Ferroelectric composites of PZT-Pt

Graduation committee:

Chairman:	Prof. dr. ir. J.A.M. Kuipers	University of Twente
Promotor:	Prof. dr. ing. D.H.A. Blank	University of Twente
Assistant promotors:	Dr. ir. H.J.M. Bouwmeester	University of Twente
	Dr. ing. A.J.H.M. Rijnders	University of Twente
Committee members:	Dr. B. Noheda	University of Groningen
	Prof. dr. R. Wolf	Philips Research Eindhoven
	Prof. dr. ir. B. Poelsema	University of Twente
	Prof. dr. J. Schmitz	University of Twente
	Dr. ir. B.A. Boukamp	University of Twente

The research described in this thesis was financially supported by the Strategic orientation Materials Science of Interfaces, MESA$^+$ Institute for Nanotechnology. It was carried out in the Inorganic Materials Science group at the Faculty of Science and Technology and MESA$^+$ Institute for Nanotechnology at the University of Twente, P.O. Box 217, 7500 AE Enschede, The Netherlands.

Ferroelectric composites of PZT-Pt
Pham Thi Ngoc Mai
ISBN 90-365-2121-1

Printed by PrintPartners Ipskamp, Enschede, The Netherlands.

FERROELECTRIC COMPOSITES OF PZT-Pt

DISSERTATION

to obtain
the doctor's degree at the University of Twente,
on the authority of the rector magnificus,
prof. dr. W.H.M. Zijm,
on account of the decision of the graduation committee,
to be publicly defended
on Friday 28th January 2005 at 15.00

by

Pham Thi Ngoc Mai

born on 29th January 1977

in Hanoi, Vietnam

The dissertation is approved by the promotor Prof. dr. ing. D.H.A. Blank and the assistant promotors Dr. ir. H.J.M. Bouwmeester and Dr. ing. A.J.H.M. Rijnders

Table of contents

1

Introduction

1.1 Dielectric materials and their properties

Dielectric materials are electrical insulators, exhibiting an electric dipole structure, in which positive and negative electrically charged entities are separated on a molecular or atomic level [1] (see Fig. 1.1).

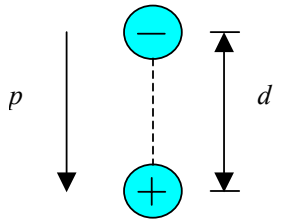

Fig. 1.1. Schematic representation of an electric dipole generated by two electrical charges of magnitude q and separated by a distance d, giving a dipole moment $p = qd$. The associated polarisation vector p is also shown.

When an external electrical field is applied, the atomic or molecular dipole moments will align to the field direction. The polarisation is defined as the dipole moment per unit volume, denoted by P. For many dielectric materials, P is proportional to the electric field strength E through the relationship:

$$P = D - \varepsilon_0 E = (\varepsilon - \varepsilon_0)E = \varepsilon_0(\varepsilon_r - 1)E \tag{1.1}$$

where $D = \varepsilon E$ is the dielectric displacement, ε the permittivity of the dielectric material, ε_0 the permittivity of the vacuum and ε_r the field-independent dielectric constant of the material, defined as:

$$\varepsilon_r = \frac{\varepsilon}{\varepsilon_0} \tag{1.2}$$

Dielectric materials are characterised by a high dielectric constant, which is always greater than unity and represents the increase in charge storing capacity by insertion of a dielectric

medium between two plates of the capacitor. The ε_r values of some dielectric materials are listed in Table 1.1.

Table 1.1. Dielectric constants of various dielectric materials [2].

Material	Dielectric constant	
	60 Hz	1 MHz
	Ceramics	
Titanate ceramics	-	15 - 10,000
Mica	-	5.4 - 8.7
Soda-lime glass	6.9	6.9
Porcelain	6.0	6.0
Fused silica	4.0	3.8
	Polymers	
Phenol-formaldelhyde	5.3	4.8
Nylon 6,6	4.0	3.6
Polystyrene	2.6	2.6

In general, the polarisation comprises four components:

$$P = P_e + P_i + P_o + P_s \tag{1.3}$$

The first component is the electronic polarisation, P_e, which arises from a displacement of the centre of the negatively charged electron cloud relative to the positive nucleus of an atom by the electric field. The second one is the ionic polarisation, P_i, which originates from the relative displacement or separation of cations and anions from each other in an ionic solid. The third contribution is the orientation polarisation, P_o, which is found only in materials with permanent dipole moments. This polarisation is generated by a rotation of the permanent moment in the direction of the applied electric field. The final source, P_s, is the space charge polarisation. This type of polarisation results from the build-up of charges at interfaces of heterogeneous systems. The different polarisation mechanisms are schematically illustrated in Fig. 1.2a, while the frequency-dependent contribution to the permittivity is schematically shown in Fig. 1.2b.

When an alternating current is applied to a dielectric material, the dipoles are no longer able to follow the oscillations of the electric field at certain frequencies. This results in an energy dissipation, called the dielectric loss:

$$\tan \delta = \frac{\varepsilon''}{\varepsilon'} \tag{1.4}$$

noting that the dielectric constant ε of a materials is a complex quantity:

$$\varepsilon = \varepsilon' + i\varepsilon'' \tag{1.5}$$

where ε' and ε'' are the real and imaginary parts, respectively.

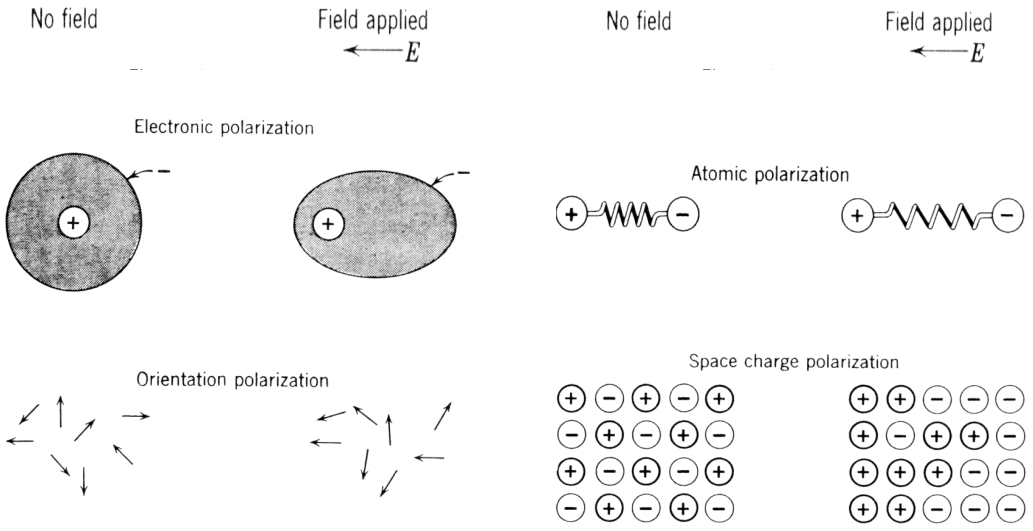

(a)

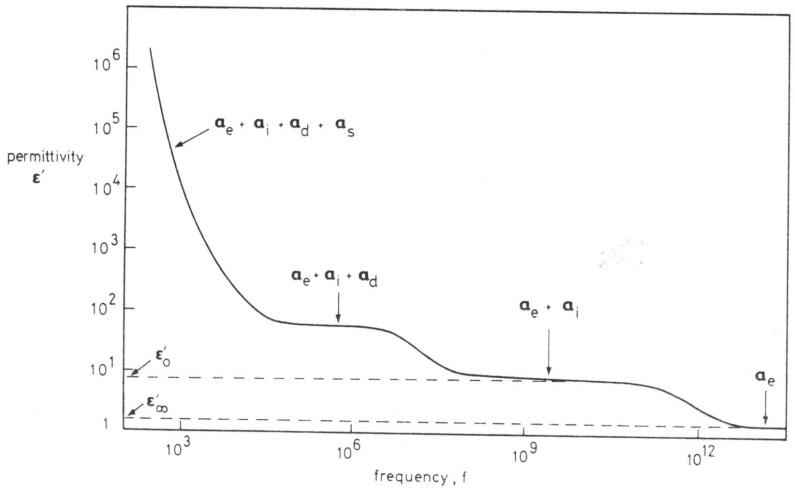

(b)

Fig. 1.2. (a) Schematic illustration of different mechanisms of polarisation [3].
(b) Variation of the permittivity with frequency of the alternating electric field. Electronic, ionic, orientation and space charge polarisation contributions to the permittivity are indicated as a_e, a_i, a_d and a_s, respectively [2].

Dielectric ceramics and polymers are used as insulators. Dielectric materials for capacitors must have a high dielectric constant, low dielectric loss, high breakdown voltage, etc. The highest dielectric constants so far have been observed in ferroelectric perovskite ceramics, among which typical examples are barium titanate ($BaTiO_3$), lead titanate ($PbTiO_3$), lead zirconate titanate ($Pb(Zr,Ti)O_3$, usually denoted as PZT).

1.2 Ferroelectric materials and their properties

Ferroelectric ceramics were discovered in the early 1940s when the phenomenon of ferroelectricity was found to be the source of the unusually high dielectric constant in ceramic barium titanate capacitors. Since that time, they became very important for many industrial applications, ranging from high-dielectric constant capacitors to later developments in piezoelectric transducers, sensors, actuators and thin film memories. These ferroelectric memories are expected to replace magnetic core memories, magnetic bubble memory systems and electrically erasable read-only memories in the near future [4-7].

1.2.1 Ferroelectricity

Ferroelectric materials are dielectric materials characterized by a reversible spontaneous polarization. The polarization behaviour in an electric field is highly non-linear and exhibits an hysteresis loop (*P*-*E* loop), as shown in Fig. 1.3a. The hysteresis loop is characterised by two important parameters, including the coercive field E_c (or coercivity) and the remanent polarisation P_r (or remanence). The coercivity is the field required to reduce the polarisation P to zero, the remamence is the polarisation at zero applied field. The value obtained by extrapolating the polarisation in the high field region to zero is called the saturation polarisation P_s.

Ferroelectricity results from the presence of permanent dipole moments that align in the direction of an external electric field. For example, in $Pb(Zr,Ti)O_3$, the dipole moment is caused by the displacement of either the Ti^{4+} or Zr^{4+} cations relative to the centre of the oxygen octahedron around the cation. The two-stable off-center positions correspond to the two different orientations of dipole moment. Adjacent dipoles tend to orient themselves in the same direction, which induces a spontaneous polarisation. Regions of uniform polarisation are called domains, separated by domain walls. In ferroelectric materials, the domain walls are extremely narrow, often not more than one or two lattice layers. The response of the domains to the applied electric field, as shown in Fig. 1.3b, determines the

shape of the hysteresis loop. In the absence of an electric field, the domains are randomly distributed, resulting in a net zero polarisation. In an electric field, the domains tend to align in the field direction by movement of the domain walls and rotation of the dipoles, and the polarisation reaches the maximum value P_s. When the electric field is removed, domains cannot return to their original states, yielding a non-zero polarisation P_r.

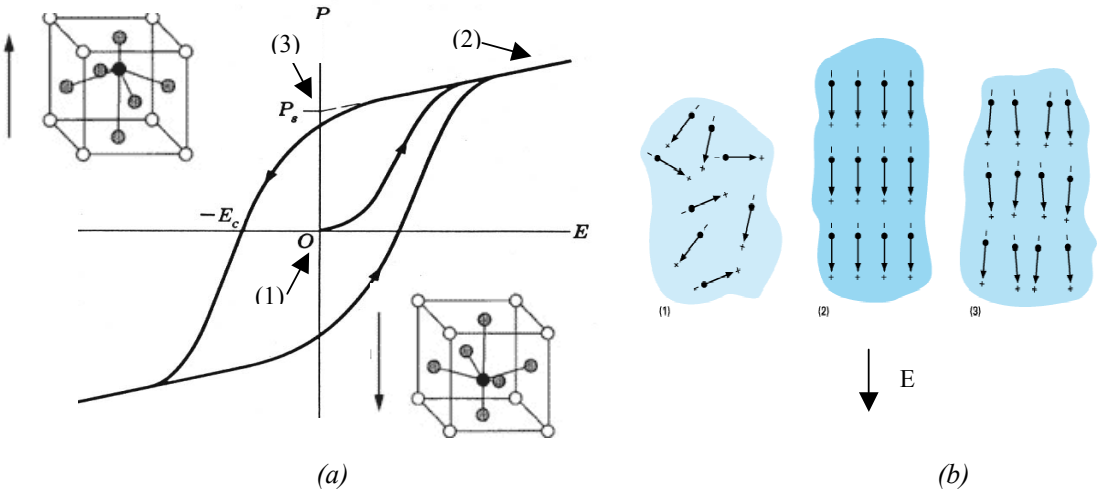

Fig. 1.3. (a) A typical ferroelectric hysteresis loop. The positive and negative saturation polarisations correspond to the two "up" and "down" states of the crystal [5].
(b) Orientation of dipoles under applied field: (1) without electric field, $P = 0$; (2) domains align in the field direction, $P = P_s$; (3) the electric field is decreased to zero, $P = P_r$.

Different from normal dielectrics, in ferroelectrics the dielectric constant is a non-linear function of applied field, and can be evaluated from the derivative of the polarisation to the applied field. Basically, there are two contributions to the dielectric constant: the intrinsic component, which involves the switching of the dipole configurations, and the extrinsic component, which involves the domain wall motion [8, 9].

A necessary condition for a crystal to exhibit ferroelectricity is that the crystal structure is non-centrosymmetric. The ferroelectric state is usually a low temperature condition, associated with the non-centrosymmetric phase. A structural phase transition from non-centrosymmetric to centro-symmetric upon heating, induces a transition from the ferroelectric-the paraelectric state. The temperature at which this transition takes place is called the Curie temperature, denoted by T_C. At T_C, the dielectric constant ε exhibits a maximum

value. Above T_C, the relationship between ε and the temperature follows the Curie-Weiss law:

$$\varepsilon \cong \frac{C}{T - T_0} \tag{1.6}$$

where C is the Curie constant and T_0 the Curie-Weiss temperature, which in most cases equal to or slightly different from T_C.

P-E loops can be used as a fingerprint to identify the material. Typical hysteresis loops obtained for various ferroelectric ceramics are presented in Fig.1.4: a) a linear tracing from a $BaTiO_3$ capacitor; b) a non-linear loop from a memory ferroelectric PZT; c) a narrow non-linear loop from a relaxor $(Pb,La)(Zr,Ti)O_3$ (PLZT) and d) a double loop typical for an antiferroelectric $Pb(Sn,Zr)O_3$ (PSZT).

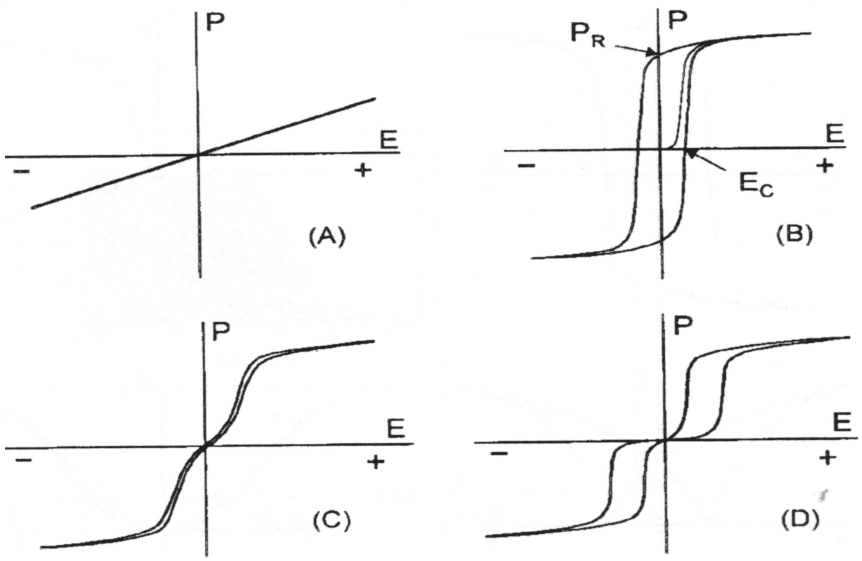

Fig. 1.4. Typical hysteresis loops from various ferroelectric ceramics: linear $BaTiO_3$ capacitor (a), ferroelectric PZT (b), relaxor 8/65/35 PLZT (c), antiferroelectric PSZT (d) [4].

Antiferroelectric materials belong to one class of deformation in the ferroelectric crystals, which has neighbouring lines of ions displaced in opposite directions. The energy difference between antiferroelectric and ferroelectric states is very small, therefore a large applied field can switch the crystal from the former to the latter.

Ferroelectric relaxors are characterized by a diffuse and dispersive phase transition where the temperature T_M at which a maximum dielectric obtained does not coincide with the structural transition temperature T_C. The remanence disappears at temperatures above a

freezing temperature T_f, which is notably less than T_M. The mean square of polarization, however, is non-zero up to 200-300 K above T_M. The unusual dielectric properties of relaxors are believed to be a consequence of the small dimension of ferroelectric regions (10-50 nm) dispersed in a paraelectric matrix. Reviews about ferroelectric relaxors can be found in Refs. [10-12].

1.2.2 Other related properties and applications of ferroelectric materials

Electro-optic properties. By varying the ferroelectric polarisation with an electric field, one produces a change in the optical properties of the ferroelectrics. The most important ones are the quadratic electro-optic effect and the biased quadratic electro-optic effect [4].

Pyroelectricity. This property relates to the ability to produce electric charges perpendicularly to the polar axis on the crystal faces as a result of a temperature change [2, 3].

Piezoelectricity. Piezoelectricity is the ability of certain crystals to produce a voltage when subjected to mechanical stress.

Ferroelasticity. A crystal that has two of more stable orientational states and can be switched from one to the other with an external mechanical stress is called ferroelastic.

Various potential applications of ferroelectric materials in commercial devices, exploiting their special properties, are presented in Fig. 1.5. These include high-dielectric constant storage capacitors, piezoelectric microactuators, infrared sensors, electro-optic light valves and thin film memories.

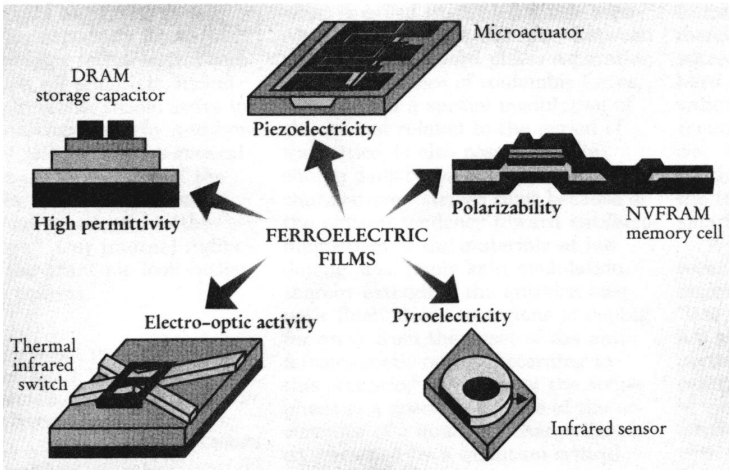

Fig. 1.5. Applications of ferroelectric materials [7].

The promising prospect of ferroelectric memories (FeRAM) in the market for memory devices is shown in Fig. 1.6, where the FeRAM offers lower power consumption and faster speed of writing (rewriting) than other kind of memories. Ferroelectric materials have been integrated into a 64 Mb DRAM devices to replace the stack/trench Si_3N_4/SiO_2 [13].

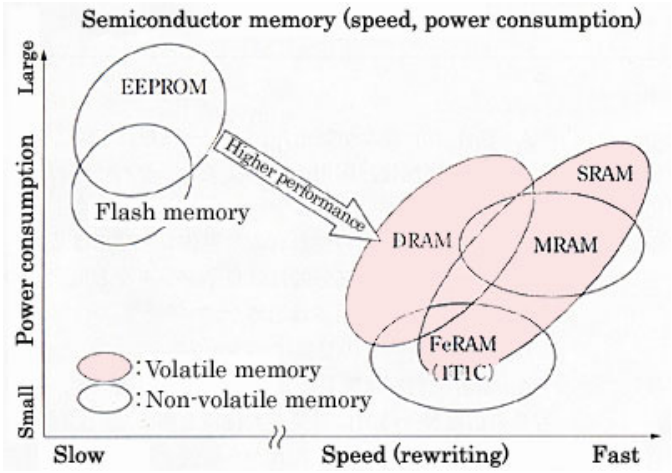

Fig. 1.6. Characteristics of memory devices [13].

Other applications relate to the high frequency response of certain ferroelectric materials. Emerging applications are in consumer portable communications, radar systems and phase array antennas, which exploit the high tunability of these materials [14].

1.3 Typical ferroelectric materials

Ferroelectric compounds are numerous, for example, potassium dihydrogenphosphate (KH_2PO_4), Rochell salt ($NaKC_4H_4O_6.4H_2O$), potassium nitrate (KNO_3), lithium niobate ($LiNbO_3$), barium titanate ($BaTiO_3$), polymer compounds based on polyvinylidene fluoride (PVF_2) and ferroelectric liquid crystals. History displays a continuous succession of new materials from various ceramic formulations, their forms (bulk, film), fabrication techniques as well as functional properties. Among them, perovskite oxides such as $Pb(Zr,Ti)O_3$, $BaTiO_3$ and $Sr(Bi,Ta)O_9$, have dominated the field.

1.3.1 Lead Zirconate Titanate (PZT)

$Pb(Zr,Ti)O_3$ (PZT) can be regarded to date as the best ferroelectric material for various applications in technology, especially for ferroelectric memories. It has the highest polarisation ($\cong$ 36 $\mu C/cm^2$) and lowest coercive field ($\geq$ 20 kV/cm) [15]. In PZT crystals, lead and

oxygen atoms appear at the corners and face centers, respectively. Octahedrally coordinated titanium or zirconium ions are located at the centre of the unit cell. Solid solutions containing less than 45 mole percent $PbTiO_3$ are rhombohedral, while those containing more than this amount are tetragonal [16]. Curie temperatures can vary from 220 °C to 490 °C, depending on the composition of PZT [15]. The phase diagram in Fig. 1.7a shows the structural changes at the Curie temperature and the morphotropic phase boundary (MPB), separating the rhombohedral and tetragonal structure at about 45 mole percent $PbTiO_3$. Very large values for the dielectric constant and the piezoelectric electromechanical coupling factor are observed near this phase boundary (see Fig. 1.7b) [17]. For large polarisation, the composition near the MPB is preferred. It is believed that the tetragonal phase with six equivalent domain states (in the <100> directions) and the rhombohedral phase with eight domain states (in the <111> directions) co-exist for these compositions, resulting in 14 possible different directions of alignment over a wide temperature range [18].

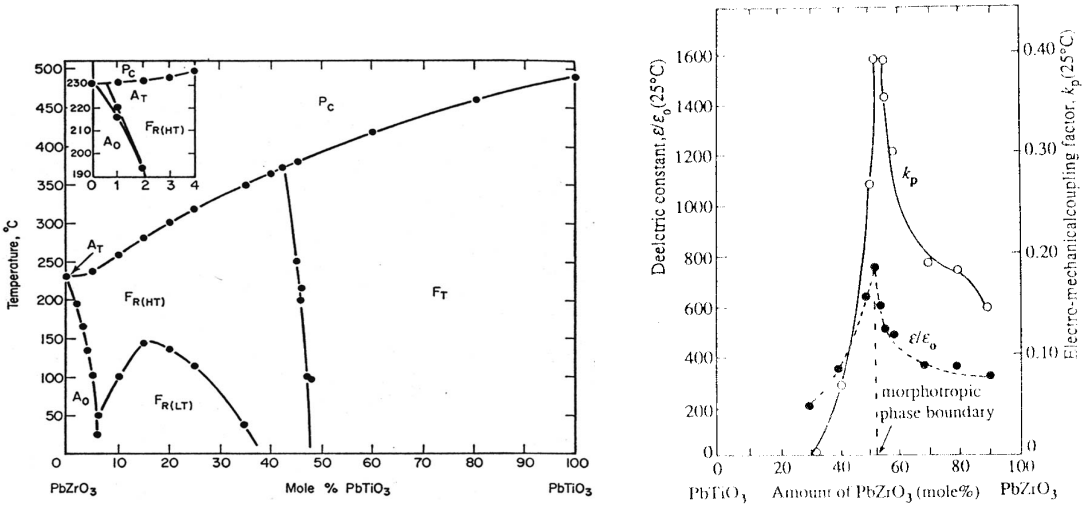

(a) *(b)*

Fig. 1.7. (a) Phase diagram of $Pb(Zr,Ti)O_3$ system [15] and (b) Composition dependence of the dielectric constant and the electromechanical coupling factor in PZT [17].

Recently, the discovery of a new monoclinic phase in PZT system in the vicinity of the MPB has been reported [19, 20]. The monoclinic structure can be considered as a "bridge" between the tetragonal and rhombohedral phases in PZT. The piezoelectric strain occurs, not along the polar axes but along the directions that induce the monoclinic distortions.

Initial studies of PZT were mainly focused on the anomalous behaviour of the dielectric constant and piezoelectric coupling of the bulk materials around MPB. Since the onset of ferroelectric memory application, extensive work on PZT thin films have been conducted in a wide composition range. The results indicate that nano-structured PZT thin films exhibit properties different from PZT bulk materials. They display higher coercive fields and somewhat lower remanent polarisations than bulk materials [6]. The hysteresis characteristics of the thin films depend on composition crystal structure, morphology, particle size and distribution, etc., and, therefore, are strongly dependent on the film fabrication.

1.3.2 PZT film fabrication

PZT thin films can be deposited either by chemical or physical vapour deposition methods. Solution chemistry approaches include sol-gel [21-24] and metal organic decomposition (MOD) [25, 26]. The sol-gel method employs alkoxide precursors in 2-methoxyethanol, whereas hydrolysis of the precursors initiates metal-oxygen-metal bond formation. During MOD, carboxylate or b-diketonate precursors are dissolved in a solvent such as xylene. The solution is relatively stable but can require higher temperature processing to remove residual organic components. The thin film is formed on a substrate by a spin or dip coating procedure, followed by firing in an oxygen-containing atmosphere. PZT requires crystallization at 550-650 °C. The phase sequence is from amorphous to the intermediate pyrochlore phase, and, subsequently, to the desired perovskite. In any case the pyrochlore phase should be prevented since it exhibits an inferior ferroelectric performance. Excess Pb is usually added to the solution because of the loss of Pb during thermal processing. Efforts are also on-going to use chemical vapour deposition (CVD) [27] or metal-organic chemical vapour deposition (MOCVD) [28, 29]. In principles, the MOCVD technique leads to faster deposition rates and to epitaxial growth of films.

Physical vapor depositions include sputtering [30-32], ion beam sputtering [33] and laser ablation [34-37] from either single or multiple targets. Sputtering has been used extensively due to its simplicity and ability to produce large uniform coatings. Pulsed laser ablation meanwhile has been used mainly at laboratory scale to rapidly explore the viability of material integration, the effect of various deposition parameters and microstructural parameters on the ferroelectric performance. The composition of films prepared by laser ablation can be ensured closely to that of the target. Another advantage of this technique is the high kinetic energy of the ablated species, resulting in highly epitaxial films. In all

techniques, oxygen (or a mixture of oxygen and argon) is frequently used as the deposition ambient to maintain the film fully oxidized. 5-10 mol % additional lead or lead oxide (PbO) is commonly added to sputtering targets to compensate for losses during processing and to ensure the desired stoichiometry in the final film. PZT films can be deposited at substrate temperatures from 250 °C to 600 °C, with an increasing need to subsequently crystallize the film by post-deposition annealing as the substrate temperature lowered. High substrate temperatures are necessary for epitaxial growth, but lower temperature deposition followed by conventional furnace annealing can produce equal or improved ferroelectric properties. The phase sequence upon annealing is similar to that observed for solution deposition, i.e., from the amorphous to the intermediate pyrochlore phase, and, subsequently, to the desired perovskite.

1.3.3 Other alternative oxides

Recently, a family of layered perovskite oxides, such as $SrBi_2Ta_2O_9$, $SrBi_2NbTaO_9$ and $SrBi_2Ti_4O_{15}$, has been explored [5, 7]. Their general chemical formulas are represented as $ABi_2B_2O_9$ and $ABi_2B_4O_{15}$, where A is a divalent metal such as Sr, Ba or Pb, B a metal of valence +5, usually Nb for the former, and of valence +4, usually Ti, for the latter. The layered structure of this kind of material is shown in Fig. 1.8.

These materials have demonstrated a high endurance during electrical cycling with excellent improved fatigue-free properties up to 10^{12} switching cycles. This very good fatigue behaviour is believed to be due to the oxygen-rich bismuth layer preventing degradation of the polarisation.

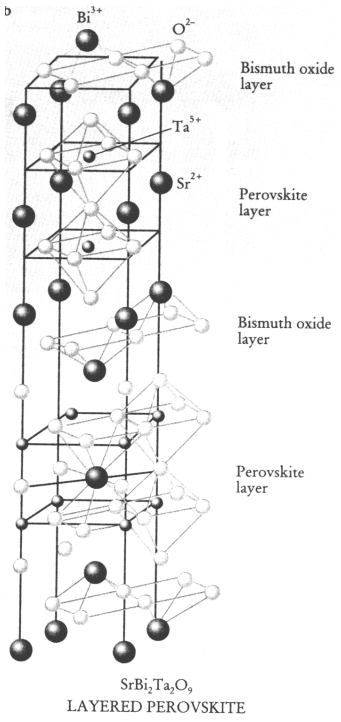

Fig. 1.8. Layered perovskite structure [7].

Other materials of interest are based on $BaTiO_3$, for example $BaTiO_3$ or $Ba(Sr,Ti)O_3$ (BST) with high dielectric constants in the range of 10^4 [4, 7]. They can be used as high-density capacitor for storage in DRAM. The materials do not contain toxic lead, which is an important environmental aspect.

$Pb(MgNb)O_3$ (PMN) is best known as a "relaxor" ferroelectric with a partially ordered perovskite structure [4, 15]. Very large dielectric constants (> 25000) and electrostriction coefficients are observed in a broad range of temperature. The dielectric constant drops rapidly with frequency (hence, it is named a "relaxor") because it takes time for the polarisation fluctuations to respond. As "relaxor" ferroelectrics, PMN-based materials have found the most successful application as high-strain electrostrictive actuators and high dielectric constant capacitors. However, PMN ceramics are somewhat difficult to prepare in pure form.

1.3.4 Seeking for new materials

To meet stringent requirements of applications, ferroelectric ceramics have been modified in various ways. To increase the electrical resistance of the material, PZT is doped with aliovalent donors, such as Nb^{5+} replacing Zr^{4+}, or La^{3+} replacing Pb^{2+}. Ceramics produced with these additives are characterised by excellent dielectric and ferroelectric properties such as a high dielectric constant, high dielectric loss, high polarisation and low coercive field. For applications exploiting pyroelectric properties, dopants such as Fe^{3+} or Sn^{4+} for replacement of Zr^{4+} or Ti^{4+}, respectively, or Ba^{2+} or Sr^{2+} for replacement of Pb^{2+}, are used to reduce the dielectric constant and dielectric loss [4].

Recently ferroelectric composites have been engineered to develop high performance in advanced technology. Ceramic-polymer composites, for example polivinylyden fluoride (PVDF)-PZT, nylon 11-PZT, combining a large piezoelectric effect of the ferroelectric ceramic with flexibility of the polymer, are widely used as acoustic devices or hydrophones [38-40]. Magnetic-ferroelectric composites like $CoFe_2O_4$-PZT, PVDF-PZT or $CoFe_2O_4$-$BaTiO_3$ [41-43] exhibit magneto-electricity by coupling electrostrictivity of the ferroelectric phase and magnetostrictivity of the magnetic phase.

Metal-ferroelectric composites offer better mechanical properties by exploiting the ductility of the metallic phase. The metallic component should not react nor dissolve in the ferroelectric phase. Hence, noble metals are most commonly utilized. Enhancement in the fracture toughness was observed for PZT-Ag, PZT-Pd-Ag and PZT-Pt composites [44-49], and was attributed to the "bridging" effect of the metallic phase behind an extending crack [42]. Resistance to fatigue after several electrical cycles can also be significantly enhanced by the ductile behaviour of the metallic phase [48].

Studies on the effect of metallic particles on the dielectric properties are quite controversial. Several authors observed the negative effect of reducing the dielectric constant, for example, from 2300 to 1700 with only 2 mol % Ag addition in PZT bulk [46], or from 400 to 100 with 5 mol % Ag addition in $PbTiO_3$ thin film [50]. Meanwhile, Maher et al. [45] reported the increase of dielectric constant from 2540 to 5100 at 10 vol.% Ag for PLZT. A similar trend has been found in other metal-ferroelectric composites. For example, an enhancement factor has been observed of 4 at 30 vol.% Pt for PZT-Pt [51] and a factor of 20 at 20 vol.% Ag for $Na_{0.5}Bi_{0.5}TiO_3$-Ag composites [52].

To deal with the behaviour of electrical properties in composites, the *effective media theories* and *percolation theory* are most common. The best-known examples of effective media theories are the Maxwell-Garnett theory and the Bruggeman theory, which has been reviewed by Meredith and Tobias [53]. These theories assume that the inhomogeneous surrounding of a particle can be replaced by an effective medium. Maxwell-Garnet theory works well in a topology referred to as *separated-grain-structure*. Here, the particles of one phase are randomly dispersed in a continuous host and are not in contact with each other. The theory is restricted to very dilute systems. If the space is filled by a random mixture of two or more constituents, then we have an *aggregate structure*, which can be described by the Bruggeman theory. This theory treats each constituent of the mixture on an equal basis. The metal-insulator transition is predicted at a critical volume fraction $V_c = 1/3$ of the metal.

Percolation theory has been reviewed by Landauer [54], while a more recent and thorough discussion is given by Sahimi [55]. The paper discusses the phenomenological equation for the conductivity of a composite system near the metal-insulator transition. In percolation theory, the two-phase composite is modelled as a lattice built up of sites and bonds. There is a probability P_{cb} for bonds or P_{cs} for sites when an infinite cluster forms, causing a conducting path and giving rise to a finite conductivity. P_{cb} and P_{cs} are called percolation thresholds. It is predicted that all transport properties (conductivity, dielectric constant, etc.) obey a power-law relation to the volume fraction V as $/V\text{-}V_c/^{-t}$, when approaching from the conductive side, and as $/V\text{-}V_c/^{-s}$, when approaching from the insulative side. Usually they are referred to as scaling laws, with parameters t and s as scaling exponents. Percolation theory further predicts a critical volume fraction $V_c = 0.16$. The difference in the predicted values of V_c between percolation theory and effective medium theory is due to the different particle size ranges considered in these models.

In the vicinity of the percolation threshold fraction (or critical volume fraction), the dielectric constant is increased significantly. The value of the critical volume fraction depends strongly on the shape, spatial distribution of the conducting phase [56] and particle sizes of the two phases [57]. Among all ellipsoids, V_c displays a maximum value for spherical particles. In the case of overlapping spheres, an even higher value of V_c is obtained, since they require a higher area of coverage in order to percolate. With respect to particle size, V_c is inversely proportional to the size ratio of conducting over insulating particles.

In addition, the ferroelectric properties of metal-ferroelectric composites are modified in the presence of a metallic phase. The dispersion of Ag into PZT increases the Curie temperature, because the ductile behaviour of the metal particles leads to the relaxation of the transformation-induced internal stress and to modification of the paraelectric-to-ferroelectric phase transformation [49]. In PZT-Pt composites, the remanent polarisation does not much differ from monolithic PZT, but the coercivity decreases remarkably [51]. The origin of this phenomenon is not clearly understood.

1.4 Aim and outline of the thesis

The aim of the research described in this thesis is focused on the preparation and characterisation of dual-phase PZT-Pt composites. The basic idea is to enhance the dielectric and ferroelectric properties of PZT by dispersion with Pt. The high dielectric constant of such composites is promising for application in super-capacitors or for DRAM devices, while the low coercivity suits low-voltage operation for applications like non-volatile memories.

This thesis consists of seven chapters. In Chapter 1, a general introduction is presented. Properties and applications of dielectric and ferroelectric materials are described.

In Chapter 2, I present an overview of the defect chemistry of PZT, followed by a discussion about the electronic and ionic conductivities measured by impedance spectroscopy. The type of charge carriers that exist in the composites as well as their concentrations are crucial to understand the insulating properties and their effect on domain switching, fatigue or imprint after many used cycles.

Chapter 3 presents a study on the preparation and characterisation of PZT-Pt bulk composites. Several models, including the effective medium theories and the percolation theory, have been employed to explain the dependence of the dielectric constant on Pt content.

In Chapter 4, I investigate the influence of deposition parameters on the growth of PZT-Pt films by Pulsed Laser Deposition (PLD). Understanding the role of each parameter aids to obtain the desired film structure through controlling the deposition conditions.

In Chapter 5, a study on the microstructure and the electrical properties of PZT-Pt films is presented. The mutual dependence between the microstructure and the electrical properties is discussed.

A severe problem for PZT-Pt thin films is the high leakage current. In Chapter 6, a conduction mechanism is proposed for PZT and PZT-Pt films to explain the influence of Pt dispersion on leakage current.

In Chapter 7, recommendations for future research are given.

At the end of this thesis a summary is provided, while in Appendix the influence of film thickness on *P*-*E* loop of PZT thin films is given.

References

1. W.D. Callister, *Materials Science and Engineering, an Introduction*, 4th edition, John Willey & Sons Inc., 1997.
2. A.E. West, *Solid State Chemistry and its Applications*, John Willey & Sons Ltd., 1985.
3. W.D. Kingery, H.K. Bowen and D.R. Uhlmann, *Introduction to ceramics*, 2nd edition, John Wiley & Sons, 1976.
4. G.H. Haertling, *Ferroelectric Ceramics: History and Technology*, J. Am. Ceram. Soc. **82** (1999) 797.
5. F. Jona, *Ferroelectric crystals*, 1th edition, New York, Dover, 1993.
6. J. Scott and C.A. Araujo, *Ferroelectric Memorie*s, Science **246** (1989) 1400.
7. O. Auciello, J.F. Scott and R. Ramesh, *The Physics of Ferroelectric Memories*, Physics Today, July 1998, 22.
8. N.B. Chaim, M. Brunstein, J. Grunberg and A. Seidman, *Electric field dependence of the dielectric constant of PZT ferroelectric ceramics*, J. Appl. Phys. **45** (1974) 2398.
9. F. Xu, S. Trolier, W. Ren and B. Xu, *Domain wall motion and its contribution to the dielectric and piezoelectric properties of lead zirconate titanate films*, J. Appl. Phys. **89** (2001) 1336.
10. L.E. Cross, *Relaxor ferroelectrics: an overview*, Ferroelectrics **151** (1994) 305.
11. A.J. Bell, *Calculations of dielectric properties from the super-paraelectric model of relaxors*, J. Phys.: Condens. Matter **5** (1993) 8773.
12. M. Tyunina, J. Levoska, A. Sternberg and S. Leppavuori, *Relaxor behaviour of pulsed laser deposited ferroelectric* $(Pb_{1-x}La_x)(Zr_{0.65}Ti_{0.35})O_3$ *films*, J. Appl. Phys. **84** (1998) 6800.
13. J.F. Scott, *Ferroelectric memories*, Springer, 2000.
14. N. Setter, *Electroceramics: looking ahead*, J. Eur. Ceram. Soc. **21** (2001) 1279.
15. R.E. Newham, *Molecular Mechanism in Smart Materials*, MRS. Bulletin, May 1997, 20.
16. C. Kittel, *Introduction to Solid State Physics*, 6th edition, New York, John Wiley, 1986.
17. B. Jaffe and R.S. Roth, *Piezoelectric Properties of Lead Zirconate-Lead Titanate Solid Solution Ceramics*, J. Appl. Phys. **25** (1954) 809.
18. L.E. Cross, *Ferroelectric materials for electromechanical transducer applications*, Material Chemistry and Physics **43** (1996) 108.
19. B. Noheda, D.E. Cox, G. Shirane, J.A. Gonzalo, S.E. Park and L.E. Cross, *Stability of the monoclinic phase in the ferroelectric perovskite* $PbZr_{1-x}Ti_xO_3$, Phys. Rev. B **63** (2001) 014103.
20. B. Noheda, D.E. Cox, G. Shirane, J.A. Gonzalo, L.E. Cross and S.E. Park, *A monoclinic ferroelectric phase in the* $PbZr_{1-x}Ti_xO_3$ *solid solution*, Appl. Phys. Lett. **74** (1999) 2059.
21. C. Livage, A. Safari and L.C. Klein, *Glycol-based sol-gel process for the fabrication of ferroelectric PZT thin films*, J. Sol-gel Sci. and Tech. **2** (1994) 605.

22. G. Yi, Z. Wu and M. Sayer, *Preparation of $Pb(Zr,Ti)O_3$ thin films by sol gel processing: electrical, optical and electro-optical properties*, J. Appl. Phys. **64** (1988) 2717.
23. N. Floquet, J. Hector and P. Gaucher, *Correlation between structure, microstructure, and ferroelectric properties of $PbZr_{0.2}Ti_{0.8}O_3$ intergrated film: Influence of the sol-gel process and the substrate*, J. Appl. Phys. **84** (1998) 3815.
24. X. Chen, A.I. Kingon, H. Al-Shreef and K.R. Bellur, *Electrical transport and dielectric breakdown in $Pb(Zr,Ti)O_3$ thin films*, Ferroelectrics **151** (1994) 133.
25. C.H. Lin, W.D. Hsu and I.N. Lin, *Ferroelectric properties of $Pb(Zr_{0.52},Ti_{0.48})O_3$ thin films prepared by metal-organic decomposition process*, Appl. Surf. Sci. **142** (1999) 418.
26. X.J. Zheng, Z.Y. Yang and Y.C. Zhou, *Residual stresses in $Pb(Zr_{0.52}Ti_{0.48})O_3$ thin films deposited by metal organic decomposition*, Scripta Materialia **49** (2003) 71.
27. W.Y. Cheng and L.S. Hong, *Chemical vapor deposition of $Pb(Zr_xTi_{1-x})O_3$ films by $Pb(C_2H_5)_4$, $Ti(I\text{-}OC_3H_7)_4$, $Zr(t\text{-}OC_4H_9)_4$ and O_2: role of lead oxide formation from $Pb(C_2H_5)_4$ and O_2 on film properties*, Thin Solid Films **415** (2002) 94.
28. D.J. Taylor, J. Geerse and P.K. Larsen, *Fatigue of organometallic chemical vapor deposited $PbZr_xTi_{1-x}O_3$ thin films with Ru/RuO_2 and Pt/Pt electrodes*, Thin Solid Films **263** (1995) 221.
29. Y.M. Kim, W. J. Lee and H.G. Kim, *Deposition of PZT films by MOCVD at low temperature and their change in properties with annealing temperature and Zr/Ti ratio*, Thin Solid Films **279** (1996) 140.
30. T. Hase and T. Shiosaki, *Preparation and switching kinetics of $Pb(Zr,Ti)O_3$ thin films deposited by reactive sputtering*, Jpn. J. Appl. Phys. **30** (1991) 2159.
31. K. Iijima, I. Ueda, K. Kugimiya, *Preparation and properties of Lead-Zirconate-Titanate thin films*, Jpn. J. Appl. Phys. **30** (1991) 2149.
32. E. Cattan, G. Velu, B. Jaber, D. Remines and B. Thiery, *Structure control of $Pb(Zr,Ti)O_3$ films using $PbTiO_3$ buffer layer produced by magnetron sputtering*, Appl. Phys. Lett. **70** (1997) 1718.
33. I. Kanno, S. Hayashi, R. Takayama, H. Sakakima and T. Hirao, *Processing and characterization of ferroelectric thin films by multi-ion beam sputtering*, Physics Research **B 112** (1996) 125.
34. P. Verardi, M. Dinescu and F. Craciun, *Pulsed laser deposition and characterisation of PZT thin films*, Appl. Surf. Sci. **154-155** (2000) 514.
35. R. Ramesh, O. Auciello, V.G. Keramidas and R. Dat, *Pulsed laser ablation-deposition and characterisation of ferroelectric metal oxide heterostructures*, Science and Technology of Electroceramic Thin films, Eds. O. Auciello and R. Waser, pg. 1-22.
36. J.S. Horwitz, K.S. Grabowski, D.B. Chrisey and R.E. Leuchtner, *Insitu deposition of epitaxial $PbZr_xTi_{(1-x)}O_3$ thin films by pulsed laser deposition*, Appl. Phys. Lett. **59** (1991) 1565.

37. D. Roy, S.B. Krupanidhi and J.P. Dougherty, *Excimer laser ablated lead zirconate titanate thin films*, J. Appl. Phys. **69** (1991) 7930.
38. R.E. Newham and J. P. Runt, *Polymer-Piezoelectric Ceramic Composites*, Polymer News **10** (1984) 132.
39. J. Runt and E.C. Galgoci, *Polymer/Piezoelectric Ceramic Composites: Polystyrene and Poly (methyl methacrylate) with PZT*, J. Applied Polymer Science **29** (1984) 611.
40. J.F. Tressler and S. Alkoy, *Functional composites for sensors, actuators and transducers*, Composites: Part A **30** (1999) 477.
41. K. Srinivas and G. Prasad, *Electromechanical coefficients of magnetoelectric PZT-Co_2FeO_4 composite*, Mod. Phys. Lett. **B 14** (2000) 663.
42. N. Cai, J. Zhai. L. Liu, Y. Lin and C. Wen Nan, *The magnetoelectric properties of lead zirconate titanate/terfenol-D/PVDF laminate composites*, Mater. Sci. Eng. **B 99** (2003) 211.
43. H. Zheng, J. Wang, S. E. Lo, Z. Ma, L. Mohaddes-Ardabili, T. Zhao, L. Salamanca-Riba, S. R. Shinde, S. B. Ogale, F. Bai, D. Viehland, Y. Jia, D. G. Schlom, M. Wuttig, A. Roytburd, R. Ramesh, *Multiferroic $BaTiO_3$-$CoFe_2O_4$ Nanostructures*, Science **303** (2004) 661.
44. H.J. Hwang, M. Yasuoka and M. Sando, *Fabrication, Sinterability, and Mechanical Properties of Lead Zirconate Tinatate/Silver Composites*, J. Am. Ceram. Soc. **82** (1999) 2417.
45. G.H. Maher, *Effect of Silver Doping on the Physical and Electrical Properties of PLZT Ceramics*, J. Am. Ceram. Soc. **66** (1983) 408.
46. D.H. Pearce and T. W. Button, *Processing and Properties of Silver/PZT Composites*, Ferroelectrics **228** (1999) 991.
47. Y. Sato, H. Kanai and Y. Yamashita, *Effect of Silver and Palladium Doping on the Dielectric Properties of $0.9Pb(Mg_{1/3}\ Nb_{2/3})O_3$-$0.1PbTiO_3$ Ceramic*, J. Am. Ceram. Soc. **79** (1996) 261.
48. H.J. Hwang, K. Tajima and M. Sando, *Fatigue-free PZT-based Nanocomposites*, Key Engineering Materials **161-163** (1999) 431.
49. H.J. Hwang, T. Nagai and T. Ohji, *Curie Temperature Anomaly in Lead Zirconate Titanate/Silver Composite*, J. Am. Ceram. Soc. **81** (1998) 709.
50. L. Tang, P. Du, G. Han, W. Weng, G. Zhao and G. Shen, *Effect of dispersed Ag on the dielectric properties of sol-gel derived $PbTiO_3$ thin films on ITO/glass substrate*, Surface and Coatings Technology **167** (2003) 177.
51. N. Duan, J.E. ten Elshof and H. Verweij, *Enhancement of Dielectric and Ferroelectric properties by Addition of Pt Particle to a Lead Zirconate Titanate Matrix*, Appl. Phys. Lett. **77** (2000) 3263.
52. Y. Lin, C.W. Nan, J. Wang, G. Liu, J. Wu and N. Cai, *Dielectric behaviour of $Na_{0.5}Bi_{0.5}TiO_3$-based composites incorporating silver particles*, J. Am. Ceram. Soc. **87** (2004) 742.

53. R.E. Meredith and C.W. Tobias, *Conduction in Heterogenous system*, pg. 15-47, in *Advances in Electrochemistry and Electrochemical Engineering*, Vol. 2, Interscience, New York, 1962.
54. R. Landauer, *Electrical Conductivity in Inhomogenous Media*, pg. 2-45, American Institute of Physics Conference proceedings, No. 40, *Electrical Transport and Optical Properties of Inhomogenous Media*, New York, 1962.
55. M. Sahimi, *Application of percolation theory*, Taylor and Francis Ltd., 1994.
56. C. Brosseau, A. Beroual and A. Boudida, *How do Shape Anisotropy and Spatial Orientation of the Constituents Affect the Permittivity of Dielectric Heterostructure?*, J. Appl. Phys. **88** (2000) 7278.
57. A. Malliaris and D.T. Turner, *Influence of Particle Size on the Electrical Resistivity of Compacted Mixtures of Polymeric and Metallic Powders*, J. Appl. Phys. **42** (1971) 614.

2

Investigation of ionic and electronic contributions to the conductivity in lead-zirconate-titanate by impedance spectroscopy

2.1 Introduction

The transport properties in solids involve the transport of charged ionic and electronic defects. In ferroelectric materials, the movement of charged defects can change the operation device characteristics. The motion and switching behaviour of domain walls can be influenced by the presence of defects [1, 2]. Charged defects may also induce enhanced degradation for fatigue, imprint and retention, or even may lead to ultimate failure. It is therefore imperative to determine the concentrations and mobilities of these species.

In the widely-used $Pb(Zr_{1-x}Ti_x)O_3$ (PZT), the mobile charged species include electrons, electron-holes and oxygen vacancies. The concentrations of these are determined by the prevailing defect equilibria, impurity content and sample history. Unless the content of volatile PbO can be carefully controlled, relatively immobile lead vacancies are introduced during preparation in PZT, which act as acceptor centers. Charge compensation occurs by creation of oxygen vacancies or by a change in the concentration of electrons and electron holes, depending on temperature and oxygen partial pressure. At room temperature, PZT is an almost pure dielectric material with a total conductivity of less than 10^{-15} $S.cm^{-1}$. Above about 150 °C, the conductivity becomes appreciable, albeit that there are doubts regarding the relative ionic and electronic contributions to the total conductivity of PZT. In quenched samples, Raymond and Smyth [3] suggested a predominantly ionic conductivity at low temperatures.

Few electrochemical impedance studies have been performed on PZT and related compositions. Las *et al.* [4] have studied the influence of the calcining and sintering temperatures on the electrical properties of PZT. The complex impedance spectra were deconvoluted and analysed in terms of electronic conduction hindered by a grain boundary effect. Peláiz Barranco *et al.* [5] investigated lanthanum-doped PZT. The complex non-linear least-

squares (CNLS) analysis, however, did not yield a clear separation between ionic and electronic conductivity. They also studied the complex PZT-$PbCuNbO_3$ system [6] but here the frequency dispersion was analysed with a simple *(RC)* circuit, which showed a rather poor match with the experimental dispersion. In this chapter, impedance spectroscopy under various conditions of oxygen partial pressure and temperature is used to investigate the conductivity in PZT. The data are subjected to CNLS analysis using equivalent circuits, which include transport paths for both ionic and electronic charge carriers.

2.2 Defect chemistry of PZT

2.2.1 Band gap characteristics

PZT has a band gap of 3.4 eV. The valence bands are mainly made up of oxygen 2*p* states, while the conduction bands are formed by the empty *d* states of either Ti^{4+} or Zr^{4+}. The main characteristic that distinguishes PZT from other perovskite titanates is the electronic structure of the Pb^{2+} ions. These retain their 6*s* electrons, the so-called inert pairs in the valence band. Using the tight-binding method, Robertson *et al.* [7, 8] calculated that the upper valence band states are actually made up of O 2*p* and Pb 6*s*.

The conductivity becomes appreciable at temperatures above 150 °C due to the existence of donor and acceptor levels inside the band gap. The location of the Pb 6*s* orbitals in the upper valence band allows Pb^{2+} sites to serve as shallow acceptor levels for holes. Evidence of Pb^{3+} centers has been reported from illumination experiments with UV band gap light [9]. The Pb^{2+}/Pb^{3+} level is assumed to lie about 0.3 eV above the valence band edge [8, 3]. The hopping of holes via Pb^{2+} sites is considered to be more favoured than free hole conduction in the valence band [8]. Lead vacancies, denoted as V''_{Pb}, and which exist in a significant amount in PZT due to the high volatility of PbO, are believed to act as acceptor levels. The V''_{Pb}/V'_{Pb} acceptor levels are assumed to be located about 0.9 eV above the valence band [3]. Acceptor levels at this depth should also be effective hole traps at high temperature. Donors are considered to be Ti^{4+}/Ti^{3+}, the level of which lie about 1 eV below the conduction band [3]. Evidence of Ti^{3+} centers has been also reported from illumination experiments [9]. Experimental data on the *n*-type conductivity are scarce due to ease of decomposition of PZT at low oxygen activities. A tentative band structure of PZT together with estimated acceptor and donor levels is given in Fig. 2.1.

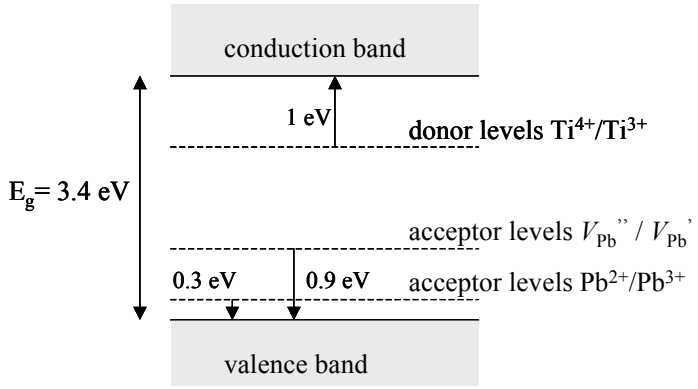

Fig. 2.1. Schematic band structure for PZT.

2.2.2 Defect chemistry

The tightly packed perovskite structure does not allow any type of interstitial ionic defect, besides protons [3]. Important defects in phase pure PZT therefore include oxygen vacancies, lead vacancies, electrons and electron holes. Oxygen vacancies are the result of equilibration with the gas phase:

$$O_O + 2h^{\bullet} \rightleftharpoons \frac{1}{2}O_2 + V_O^{\bullet\bullet} \tag{2.1}$$

with the mass-action constant:

$$K_o = \frac{p^2}{P_{O_2}^{1/2}[V_O^{\bullet\bullet}]} \tag{2.2}$$

where the well-known Kröger-Vink notation is used for the notation of defects. $V_O^{\bullet\bullet}$ denotes a doubly positively charged oxygen vacancy, $h^{\bullet}$ an electron hole ($p \equiv [h^{\bullet}]$).

Lead vacancies are formed due to the high volatility and tolerance of the PZT structure towards deficiency of PbO [10]:

$$Pb_{Pb} + O_O \rightleftarrows V_{Pb}^{''} + V_O^{\bullet\bullet} + PbO(g) \tag{2.3}$$

where Pb_{Pb} denotes lead at a regular lattice site, and (g) the gas phase. The doubly negative charge of the lead vacancies is compensated by the formation of oxygen vacancies, in accord with the charge neutrality condition:

$$2\left[V_{Pb}^{''}\right] + n = 2\left[V_O^{\bullet\bullet}\right] + p \tag{2.4}$$

where n is the electron concentration.

Other equilibria include the intrinsic ionization across the band gap, leading to the generation of electrons and holes:

$$nil \rightleftharpoons e' + h^{\bullet} \qquad K_i = np \tag{2.5}$$

as well as the ionization/trapping equilibrium of the lead vacancies:

$$V_{Pb}' \rightleftharpoons V_{Pb}'' + h^{\bullet} \qquad K_{ion} = \frac{[V_{Pb}'']p}{[V_{Pb}']} \tag{2.6}$$

By solving the above equations together with the appropriate mass conservation equations, the defect concentrations can be calculated as a function of oxygen activity. A schematic diagram of the concentrations of various defects is given in Fig. 2.2.

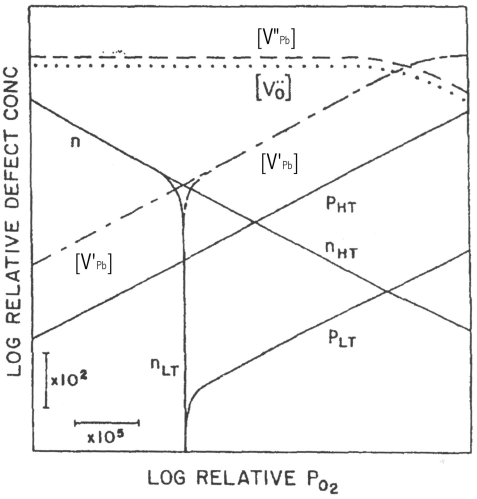

Fig. 2.2. Schematic diagram of the defect concentrations as a function of oxygen partial pressure for PZT in the presence of deep acceptor levels, V_{Pb}''/V_{Pb}', before and after quenching from high temperature (HT) to low temperature (LT). Adapted from [8].

Two main regimes are recognized in Fig. 2.2, corresponding to oxidizing and reducing conditions. The hole and electron concentrations are dominant in the oxidizing and reducing regimes, respectively. When the electron concentration is much lower than the lead vacancy concentration ($n \ll [V_{Pb}'']$), while the hole concentration is much lower than the oxygen vacancy concentration ($p \ll [V_O^{\bullet\bullet}]$), the following relation is deduced from Eq. (2.4): $[V_o^{\bullet\bullet}] = [V_{Pb}'']$, describing the regime where the major defects are oxygen vacancies and lead vacancies. A constant line in the defect diagram represents the oxygen vacancy con-

centration, if we assume that the lead vacancy concentration is not dependent on oxygen partial pressure in this regime. Meanwhile, two straight lines with a slope of 1/4 and -1/4 represent the calculated hole and electron concentrations, respectively.

The above descriptions, however, apply when the rate of reaction (2.1) is fast compared with the time scale of the experiments. When the oxidation reaction is too slow to attain equilibrium (for example, at low temperature or after quenching), the oxygen vacancy concentration is "frozen-in". Under these conditions, the defect concentrations should be calculated without taking into consideration the corresponding mass-action equation (2.2). Accordingly, in case of acceptor impurities, V''_{Pb}/V'_{Pb} in Fig. 2.2, the electron concentration is little affected by the quenching, but the hole concentration is significantly lowered by trapping at these deep acceptor centers. The order of decrease is proportional to the acceptor ionization energy. At about the point of intersection between the extrapolated lines of the free n-type charge carrier concentration, n, and the trapped hole concentration, $[V'_{Pb}]$, sharp minima occur [11, 12]. The transition point from the high-temperature (HT) to the low-temperature (LT) regimes relates to the equilibrium rate of the oxidation reaction. For the titanate perovskites, it is in the range of 400 °C to 600 °C [11], but strongly depends on the geometry and microstructure of the sample, and on the time scale of the experiments.

2.2.3 Conductivities

The electrical conductivity (σ) is the sum of the electronic (σ_{el}) and ionic (σ_i) contributions:

$$\sigma=\sigma_{el}+\sigma_i=\sigma_e+\sigma_h+\sigma_i \tag{2.7}$$

where the subscripts e and h and correspond to electrons and holes, respectively. Both are determined by the concentration n_j, charge q_j and mobility μ_j of the involved charge carriers:

$$\sigma_j = n_j q_j \mu_j \tag{2.8}$$

In perovskite materials, the ionic conductivity is mainly due to oxygen vacancies since these are the only ionic defects that have a significant mobility.

2.2.3.1 High-temperature conductivity

The results of several studies evidence the p-type conduction (hole conduction) of PZT at high temperature (T = 500-1000 °C) in a broad range of oxygen partial pressure

(pO_2 = 1-10^{-5} atm) [13-15]. Information about the *n*-type conductivity is difficult to obtain, because PZT is not chemically stable at oxygen partial pressures where it becomes an *n*-type semiconductor. It is only possible to infer *n*-type contributions from the transition from *p*- to *n*-type conduction at about 10^{-5} atm, leading to a deviation of straight line behaviour in the plot of logσ *vs*. log(pO_2) [13]. At high temperature, the contribution of ionic conductivity is small, as illustrated by the small ionic transfer numbers found. These are in the range 0.01-0.02 [13, 14].

The activation energy of p-type conductivity in the high temperature regime is reported to be in the range of 0.6 [13] to 0.71 eV [14, 15]. The activated behaviour originates from the thermally activated mobility in conjunction with the presence of deep acceptor centers. From the temperature dependence of the d.c conductivity, Smyth *et al.* calculated an activation energy for the hole mobility of 0.3 eV and for the ionisation energy 0.87 eV [14]. The hole mobility is in good agreement with the value of 0.26 eV obtained by Prisedsky and Shishkovsky [13]. The value of 1.3×10^{-3} cm^2/Vs observed at 600 °C is consistent with a small-polaron mechanism for holes via Pb^{2+} sites.

2.2.3.2 Low-temperature conductivity

Exploratory studies performed on the conductivity of PZT at low temperature are scarce. The *p*-type conductivity is regarded not to be significant at low temperatures due to the presence of deep trapping levels for holes [3, 16]. The conductivity of samples quenched after equilibration at 700 ºC in the intermediate range of pO_2 from 1-10^{-14} atm is found to be constant [3]. This has been attributed to ionic contributions to the conductivity of PZT. The corresponding activation energy is about 1.1 eV, which is in agreement with that of hopping of oxygen vacancies [11, 17]. Oxygen concentration cell measurements on related pervoskite titanates, such as $BaTiO_3$ and $SrTiO_3$ single crystals, which are expected to show similar conduction behavior, reveal very low ionic transport numbers [18, 19]. The low mobility found for oxygen vacancies, 6×10^{-9} cm^2/Vs at 250 °C [8], when compared with that of electron holes 1.3×10^{-3} cm^2/Vs [10], would not support either a significant contribution of ionic conductivity. Acceptor impurities, either deliberately added or, in the case of PZT, due to volatility of PbO, enhances the concentration of oxygen vacancies. According to Waser [11], the association equilibrium between oxygen vacancies and the acceptor centers could play a decisive role in determining the extent of ionic conductivity in these solids at room temperature:

$$A' + V_O^{\bullet\bullet} \rightleftharpoons \{A - V_O\}^{\bullet} \tag{2.9}$$

$$A'' + V_O^{\bullet\bullet} \rightleftharpoons \{A - V_O\}^{\times} \tag{2.10}$$

2.3 Experimental

Samples were prepared from commercial PZT powders (TRS Ceramics, State College, PA, USA) with Zr/Ti atomic ratio of 53:47. The composition of the starting powder was analysed by using a X-ray fluorescence (XRF, Philips PW 1840). The powder was pressed into pellets with a diameter of 10 mm, first by unaxial pressing, followed by isostatic pressing at 4000 MPa. The samples were sintered in air at 1150 °C for 2 h. During sintering the samples were embedded in $PbTiO_3$ powder in a closed Pt crucible in order to minimize Pb loss. The relative densities of sintered samples were 98-99 % of the theoretical density. The average grain size was in the range of 5-10 μm. Afterwards the samples were cut to cylinders of about 8.0 mm in diameter and thickness of 1 mm (thin sample) and 2.95 mm (thick sample). Both sides of the cylinders were polished with diamond paste. For impedance measurements, gold electrodes were deposited on both sides of samples by d.c-sputtering, followed by applying additional gold paint layers, which were cured at 700 °C.

The oxygen partial pressure during the impedance measurements was regulated between 1 Pa (≈ 10^{-5} atm) and 75 kPa (≈ 0.75 atm) using two gas-flow controllers. Nitrogen was used as a balance gas. The actual oxygen partial pressure was measured directly at the vent of conductivity cell by an oxygen sensor (Systech, model ZR 893/4). For most measurements a mixture of 80/20 N_2/O_2 was used.

Impedance data were collected in the frequency range from 0.1 Hz to 65 kHz using a frequency response analyser Solartron 1250 in combination with high impedance differential pre-amplifiers. An amplitude of 50 mV (rms) was used. After each change of temperature or oxygen pressure, the samples were allowed to equilibrate for a substantial amount of time (minimum of 3 to 4 h). The impedance data were validated using a specially developed Kramers-Kronig test program [20] and subsequently analysed with the CNLS-fit program “Equivalent circuit” [21, 22].

The samples were slowly heated in a N_2/O_2 gas stream to 603 °C. At this temperature, the pO_2 dependence of the impedance was measured. Next the impedances were measured as function of temperature down to 200 °C in the same gas mixture. Subsequently, the sample

was heated again to 603 °C at $pO_2 \approx 1$ Pa (in nitrogen gas flow) and subsequently cooled down to room temperature by placing the measurement cell outside of the furnace. Finally, the impedances were recorded as a function of temperature in an oxygen partial pressure of about 1 Pa, using a nitrogen gas flow.

2.4 Results

2.4.1 Sample purity

XRF analysis on the starting powder showed a composition of $Pb_{0.98}Zr_{0.53}Ti_{0.47}O_3$. Hafnium was found as the major impurity (0.4 wt.% HfO_2). A small amount of iron was also detected, about 2×10^{-3} wt.% Fe_2O_3. Al, Mg, Na and Si were not found, but the limit of detection was rather insensitive (respectively, 0.13, 0.25, 0.4 and 0.1 wt.%, based on the oxides). XRD analysis at room temperature on the sintered samples showed only reflections of tetragonal PZT.

2.4.2 Data analysis

The impedance spectra measured in air in general showed a large, somewhat depressed semi-circle. With varying the temperature and oxygen pressure, an extra semicircle contribution appears at low frequencies. Impedance data obtained at different temperatures is provided in Fig. 2.3. The data was first validated using a Kramers-Kronig transform test program check for systematic errors (which may originate from non-equilibrium conditions, non-linear response, slowly drifting temperature, aging or degradation of the cell). After that, the data was analyzed by using the equivalent circuits presented in Fig. 2.4. Solid lines in Fig. 2.3 represent the corresponding CNLS-fits.

For measurements carried out at high temperature and high oxygen partial pressures, the circuit of Fig. 2.4.A was mostly used. In this circuit, C_{geom} represents the dielectric response of the material, from which the dielectric constant of sample is deduced. R_{electr} and R_{ionic} represent the electronic and ionic resistances, respectively. C_{ionic} represents the blocking capacitance associated with ionic conduction. Other measurements required addition of extra (RQ) circuits to be included in the ionic path, which are tentatively assigned to grain boundary dispersion R_{gb} or to Warburg diffusion associated with charge transfer (see Fig. 2.4B-C).

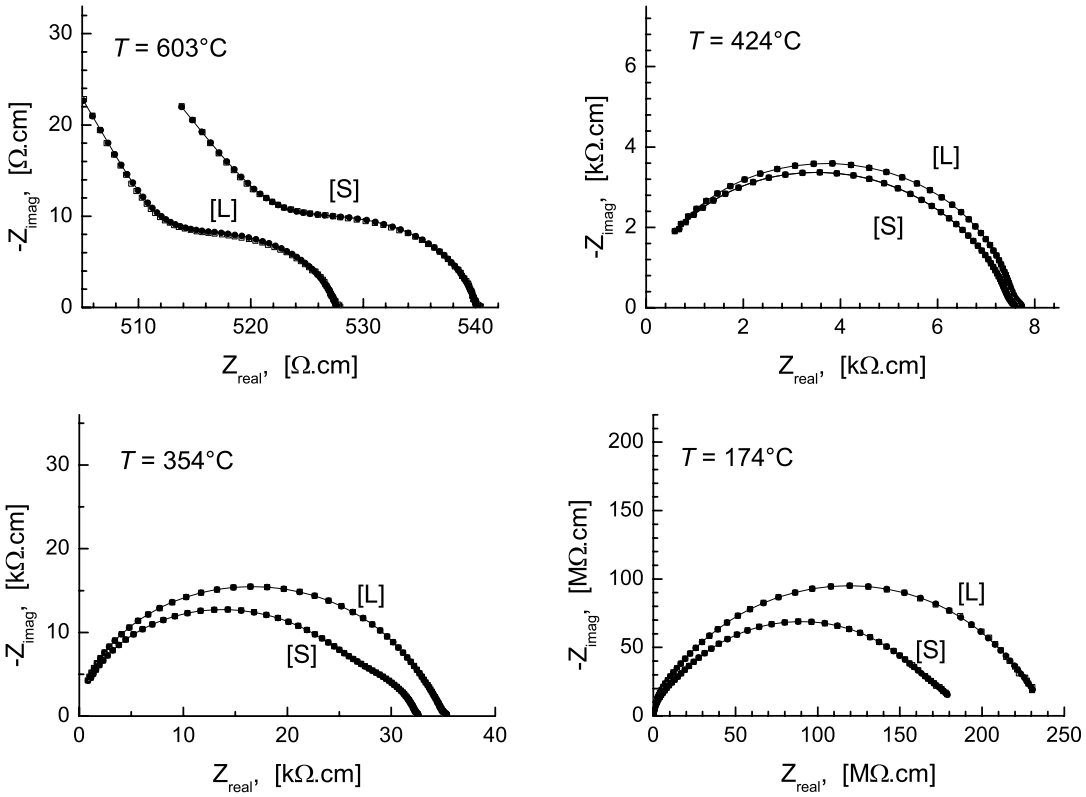

Fig. 2.3. Impedance plots measured at different temperatures and at pO_2 = 20 kPa for the thick (L) and thin (S) samples.

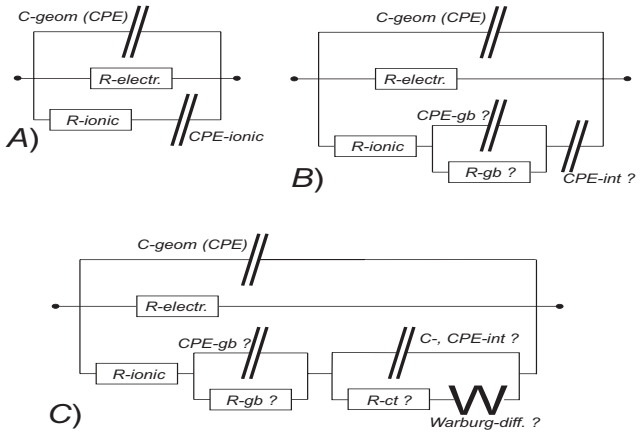

Fig. 2.4. Equivalent circuits used in the analysis of the impedance data.

2.4.2.1 Dielectric constant

The dielectric response (C_{geom}) can be represented by a constant phase element (CPE):

$$Y(\omega) = Y_0(j\omega)^n \tag{2.11}$$

At room temperature, n is found almost 1, indicating purely capacitive behaviour. At higher temperature, n decreases to about 0.7-0.8, i.e. departing from the ideal dielectric response. The apparent dielectric constant was calculated as follows:

$$\varepsilon = \frac{Y_0^{1/n} d}{A\varepsilon_0} \tag{2.12}$$

where d is the sample thickness, A the electrode surface and ε_0 the vacuum permittivity. Corresponding results are plotted versus temperature in Fig. 2.5. A clear peak is observed around the Curie temperature at 400 °C. An identical response was obtained from data of measurements in oxygen and nitrogen atmospheres. The inset of Fig. 2.5 shows that the Curie-Weiss law is obeyed over the temperature range 400-520 °C.

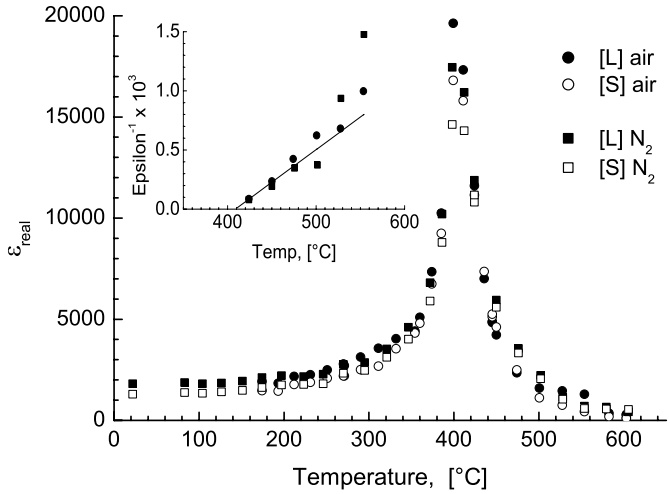

Fig. 2.5. Real part of the dielectric constant as a function of temperature in air and in nitrogen. The inset shows the Curie-Weiss law behaviour for the thick (L) sample.

2.4.2.2 Conductivity

a. Electronic and ionic conductivity

The partial electronic and ionic conductivities were calculated from R_{ionic} and R_{electr}, respectively, using:

$$\sigma = \frac{A}{d}\frac{1}{R} \tag{2.13}$$

In Fig. 2.6, the electronic and ionic conductivities, measured at 603 °C as a function of oxygen partial pressure, are presented. The ionic component is found independent of oxygen partial pressure, while the electronic conductivity shows a $(pO_2)^{0.27}$ dependence.

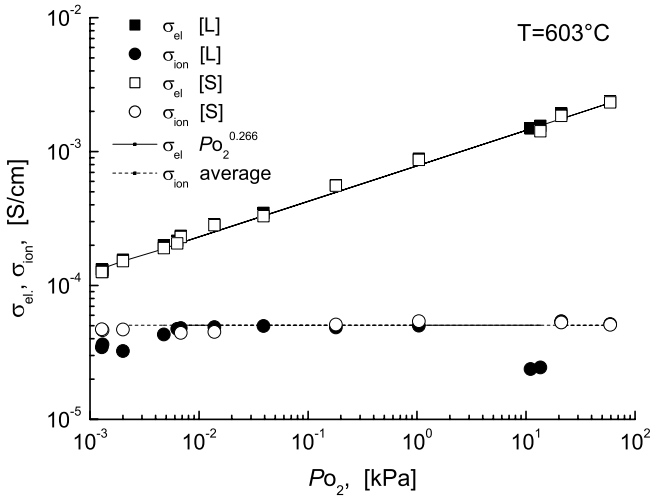

Fig. 2.6. Oxygen partial pressure dependence of the electronic and ionic conductivities measured at 603 °C. Solid lines present linear fits to the data points.

The relative ratio between the ionic and electronic conductivities is evaluated through the ionic transfer number $t_i = \sigma_i/(\sigma_i + \sigma_{el})$. At 603 °C, t_i has a small value of 0.025, which indicates that the electronic conductivity is predominant at this temperature. The obtained value is in agreement with results from Prisedsky and Shishkovsky [10] and Schwitzgebel *et al.* [11]. With decreasing temperature, the ionic transfer number gradually increases. At 150 °C, the ionic conductivity becomes more dominant. With $\sigma_i = 5\times10^{-8}$ S/cm and $\sigma_{elec} = 2\times10^{-8}$ S/cm, t_i is calculated to be 0.71. Arrhenius plots of the electronic and ionic conductivities are displayed in Figs. 2.7 and 2.8, respectively.

For both ionic and electronic conductivities, two regions with different activation energies can be discerned. This is in accordance with literature [4, 5]. The transition from the low- to high-temperature regime coincides with the Curie temperature (see Fig. 2.7), at which the paraelectric-ferroelectric transition (corresponding to the cubic-tetragonal phase transition) takes place. The obtained values for the activation energies together with corresponding values from literature are listed in Table 2.1.

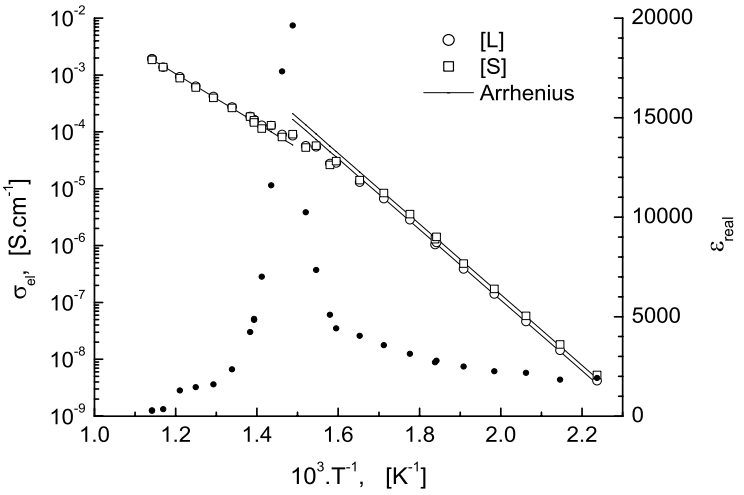

Fig. 2.7. Arrhenius plot of the electronic conductivity measured for the thick (L) and thin sample (S). The dielectric constant (solid points) is given for comparison.

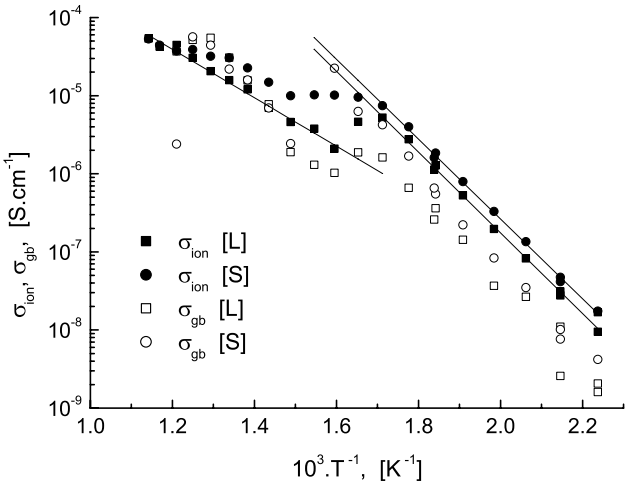

Fig. 2.8. Arrhenius plots of the ionic and grain boundary conductivities.

Table 2.1. Activation energies of electronic ($E_{a,elec}$) and ($E_{a,ionic}$) ionic conductivities of PZT as measured in air for the thick sample.

Activation energy	$E_{a,elec}$ (eV)		$E_{a,ionic}$ (eV)	
	Low T	high T	low T	high T
Our data	1.22 ($T < T_C$)	0.85 ($T > T_C$)	1.02 ($T < T_C$)	0.61 ($T > T_c$)
Branco *et al.* [5]		1.95 (T > 500 °C)	1.03 (T < 500 °C)	-
Las *et al.* [4]	1.10 ($T < T_C$)	0.70 ($T > T_C$)	-	-
Prisedsky *et al.* [13]	1.0 (300 °C)	0.60 (950 °C)	-	-
Smyth *et al.* [3, 14]	-	0.71 (T > 500 °C)	1.10 (constant with T)	

b. Grain boundary conductivity

Even though significant scatter is present in the data, a clear activated behaviour is observed in the grain boundary conductivity (see Fig. 2.8). Its Arrhenius behaviour resembles that of the ionic conductivity, clearly showing two distinct temperature regimes. The grain boundary conductivity in the low-temperature region is up to a factor of about 5 smaller than the ionic conductivity.

c. Conductivity of samples in N_2

The temperature dependence of the partial conductivities was measured in flowing nitrogen (pO_2 ~ 1 Pa) after equilibration at 603 °C and cooling to 200 °C. Arrhenius graphs for the ionic and electronic conductivities are given in Figs. 2.9 and 2.10, respectively. Again, both clearly demonstrate two activation regimes. The activation energies are identical within experimental error to those obtained for the samples measured in air. It is seen from Fig. 2.10 that the ionic conductivity above the Curie transition temperature is almost independent on the measurement ambient, as is in concordance with the pO_2 dependent measurements at 603 °C presented in Fig. 2.6. Below the transition a significant drop is observed.

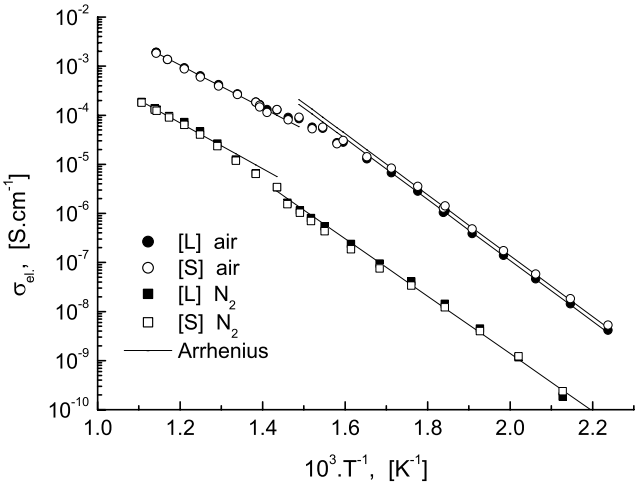

Fig. 2.9. Arhenius graph of the electronic conductivity, measured in N_2, in comparison with that measured in air. Lines represent the linear fitting.

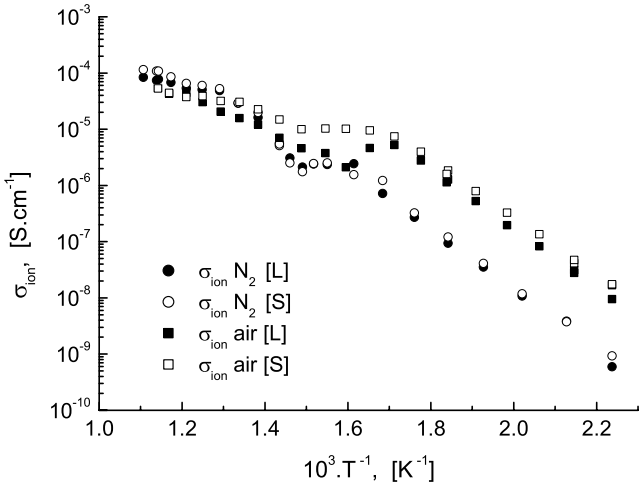

Fig. 2.10. Arrhenius graphs of the ionic conductivity, measured in N_2, in comparison with that measured in air. Conductivities above the Curie transition are identical within the experimental error.

d. Equilibration kinetics

The conductivities of the thick and thin samples measured at high temperature, above approximately 400 °C, showed no difference (see Figs. 2.6 and 2.7). At lower temperatures, the thin sample exhibits a higher conductivity, about a factor of 1.25 for the electronic conductivity and a factor of 1.6 for the ionic conductivity. Impedance measurements were conducted on the thick and thin PZT samples at 360 °C, following a pO_2 step change from 20 kPa to about 1 Pa. Figure 2.11 shows that over two weeks of time are required to complete equilibration with the gas phase at this temperature.

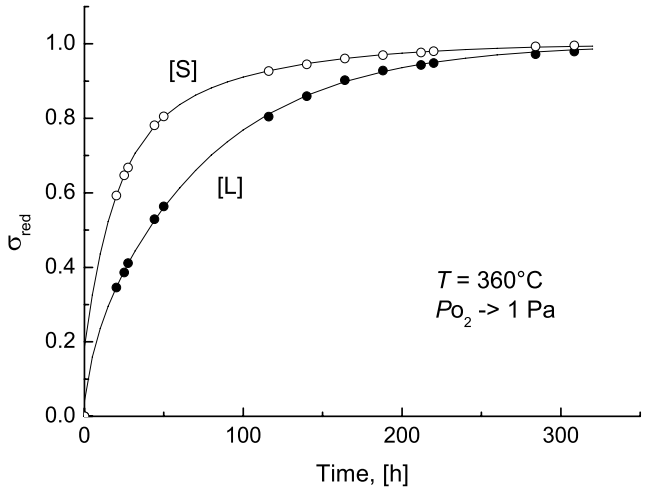

Fig. 2.11. Response of the electronic conductivity on a pO_2 jump from 20 kPa to 1 Pa. Solid lines present fits to the data points, using a diffusion-limited response model [23].

2.5 Discussion

The pO_2 dependencies of the electronic and ionic conductivities observed at 603 °C (see Fig. 2.6) are in good agreement with the defect chemistry described in Section 2.2.2. A constant ionic conductivity suggests that the concentration of oxygen vacancies is determined by the concentration of lead vacancies, due to PbO loss: $[V_o^{\bullet\bullet}] = [V_{Pb}^{''}]$. The exponent for the oxygen partial pressure is close to 1/4, which is characteristic for *p*-type conductivity. It should be noted that *n*-type contributions are beyond the experimental range of oxygen partial pressure. The present results are consistent with data of the total electrical conductivity obtained by other researchers [13-15], and also assure trustworthiness of the analysis of the impedance data using equivalent circuits.

At 603 °C, the electronic conductivity is found to be predominant, in spite of oxygen vacancies being the majority defect species. The ionic conductivity is about two orders of magnitude smaller than the electronic conductivity. This can be attributed to the large difference between the mobility of the electron holes (1.3×10^{-3} cm^2/Vs [11]) and that of the oxygen vacancies (6×10^{-9} cm^2/Vs [13]). At about 200 °C, the values of the ionic and electronic contributions to the conductivity are comparable (see Figs. 2.7 and 2.8). This disagrees with observations made by Raymond and Smyth [3], who found the ionic conductivity to be dominant at low temperature. A simple explanation is the difference in sintering conditions in both studies. The volatility of PbO, which determines the concentration of oxygen vacancy, is difficult to control during sintering at high temperature. In our study, care was taken to prevent loss of PbO during the preparation (see the experimental section). No further details are given in the paper by Raymond and Smyth [3].

Las *et al.* [4] attributed the different activation energies observed below and above the Curie transition temperature to the different mobility of *p*-type charge carriers in two phases, which differ in either electrical (paraelectric-ferroelectric) or structural (cubic-tetragonal) configuration. Another explanation, at least one contributing to the different activation energies in both phases, is the observed slow equilibration kinetics for oxygen exchange between the gas phase and the oxide at reduced temperature. Conduction in PZT is assumed to occur via a small polaron mechanism [13]. The apparent activation energy of *p*-type conduction in PZT comprises contributions arising from the ionisation/trapping equilibrium (Reaction 2.6), the oxygen exchange reaction (Reaction 2.1) and the thermally activated mobility:

$$E_a = E_{ion} - \Delta H_{ox}/2 + E_{a,m} \quad (2.14)$$

where E_{ion} denotes the ionisation energy of V_{Pb}', ΔH_{ox} the oxidation enthalpy, and $E_{a,m}$ stems from the thermally activated small polaron mobility. If the oxygen exchange reaction is no longer active at reduced temperatures, the oxygen stoichiometry of PZT is frozen, and also the (negative) enthalpy term $\Delta H_{ox}/2$ cancels in this expression. Assuming that the oxygen exchange reaction is reversible above and is blocked below the Curie temperature, we calculate a value of -0.74 eV for ΔH_{ox}. This value ought to be compared with the -0.49 eV estimated from comparison of data of conductivity at elevated temperatures with those obtained from measurements carried out at constant oxygen stoichiometry using sealed cell techniques [14]. Even though the agreement is not perfect, the present analysis shows that the slow equilibration of oxygen affects the activation energy of the electronic conductivity in the tetragonal phase.

The trapping equilibrium (Reaction 2.6) leads to a significant reduction of free holes at reduced temperatures, and increases the concentration of the singly-charged lead vacancy V_{Pb}' (trapped hole). If it is assumed that oxygen vacancies at reduced temperature form immobile defect associates with the remaining doubly-charged lead vacancies, according to reaction:

$$V_{Pb}'' + V_O^{\bullet\bullet} \rightleftharpoons \{V_{Pb} - V_O\}^{\times} \qquad K_{assoc.} = \frac{[V_O^{\bullet\bullet}][V_{Pb}'']}{[\{V_{Pb}'' - V_O^{\bullet\bullet}\}]} \quad (2.15)$$

where $K_{assoc.}$ is the corresponding equilibrium constant, this leads to a decrease in the concentration of mobile oxygen vacancies and, hence, in ionic conductivity. Accordingly, the concentration of mobile oxygen vacancy can be linked to the concentration of electron holes:

$$[V_O^{\bullet\bullet}] \sim \left(p \frac{K_{assoc.}}{K_{ion}} \right)^{1/2} \quad (2.16)$$

From this relation it follows that a decrease of the electronic conductivity by a factor of 100 leads to a decreases of the ionic conductivity by a factor of 10. This is in fair agreement with the experimental observations (see Figs. 2.9 and 2.10), suggesting that defect association would reduce the ionic conductivity in the low-temperature tetragonal phase.

2.6 Conclusions

Using complex impedance spectroscopy, the electronic and ionic conductivities of PZT were investigated in the range of oxygen partial pressure 100 kPa - 1 Pa and temperature 150-630 °C. The results are in agreement with defect chemical considerations, suggesting that lead and oxygen vacancies are the majority lattice defects. At high temperature, the *p*-type conductivity is found dominant. Below the Curie transition temperature, where the cubic-tetragonal phase transition takes place, a significant contribution of ionic conductivity is observed.

For both ionic and electronic conductivities, two regions with different activation energies can be discerned. The slow equilibration kinetics of the oxygen exchange reaction between the gas phase and the oxide for the tetragonal phase, contributes to a higher value of activation energy than observed for the high-temperature cubic phase. Defect association between lead vacancies and oxygen vacancies in the tetragonal phase reduces the concentration of mobile oxygen vacancies and thus the ionic conductivity. A model is presented in which the concentration of mobile oxygen vacancies is linked with the concentration of free electron holes.

References

1. W.L. Warren, D. Dimos, B.A. Tuttle, G.E. Pike, R.W. Schwartz, P.J. Clews and D.C. McIntyre, *Polarisation suppression in $Pb(Zr,Ti)O_3$ thin films*, J. Appl. Phys. **77** (1995) 6695.
2. H.M. Duiker, P.D. Beale and J.F. Scott, C.A. Paz de Araujo, B.M. Melnick and J.D. Cuchiaro, L.D. McMillan, *Fatigue and switching in ferroelectric memories: Theory and experiments*, J. Appl. Phys. **68** (1990) 5783.
3. M.V. Raymond and D.M. Smyth, *Nonstoichiometry, defects, and charge transport in PZT*, *In Science and Technology of Electroceramic Thin Films*, eds. O. Auciello and R. Waser, Dodrecht: Kluwer Academic Publishers, 1995, pgs. 315-325.
4. W.C. Las and P.D. Spagnol, *Electrical characterization of lead zirconate titanate prepared by organic solution route*, Ceramics International **27** (2001) 367.
5. A.P. Barranco, F.C. Pinar, O.P. Martinez, J.D.L. Santos Guerra and I.G. Carmenate, *AC behavior and conductive mechanism of 2.5 mol % La_2O_3 doped $PbZr_{0.53}Ti_{0.47}O_3$ ferroelectric ceramics*, J. Eur. Ceram. Soc. **19** (1999) 2677.
6. A.P. Barranco, F. Pinar, O.P. Martinez, J.D.L. Torres Garcia and A. Huanosta-Tera, *AC conductivity behaviour of a hot pressed [$PbTiO_3$-$PbZrO_3$-$PbCuNO_3$] ferroelectric ceramics*, Acta Mater. **49** (2001) 3289.
7. J. Robertson, W. L. Warren and B.A. Tuttle, *Band states and shallow hole traps in $Pb(Zr,Ti)O_3$ ferroelectrics*, J. Appl. Phys. **77** (1995) 3975.
8. J. Robertson, W. L. Waren, B.A. Tuttle, D. Diamos and D. M. Smyth, *Shallow Pb^{3+} hole traps in lead zirconate titanate ferroelectrics*, Appl. Phys. Lett. **63** (1993) 1519.
9. W.L. Waren, C.H. Seager and D. Dimos, *Optically induced absorption and paramagnetism in lead lanthanum zirconate titanate ceramics*, Appl. Phys. Lett. **61** (1992) 2530.
10. R.L. Holman and R.M. Fulrath, *Intrinsic nonstoichiometry in the lead zirconate-lead titanate system determined by Knudsen effusion*, J. Appl. Phys. **44** (1973) 5227.
11. R. Waser, *Bulk conductivity and defect chemistry of acceptor-doped strontium titanate in the quenched state*, J. Am. Ceram. Soc. **74** (1991) 1934.
12. J. Maier, *Complex oxides: high temperature defect chemistry vs. low temperature defect chemistry*, Phys. Chem. Chem. Phys. **5** (2003) 2164.
13. V.Prisedsky and V.I. Shishkovsky**,** *High temperature electrical conductivity and point defects in lead zirconate titanate*, Ferroelectrics **17** (1978) 465.
14. M.V. Raymond and D.M. Smyth, *Defect chemistry and transport properties of $Pb(Zr_{1/2}Ti_{1/2})O_3$*, Intergrated Ferroelectrics **4** (1994) 145.

15. G. Schwitzgebel, J. Maier, U. Wicke and H. Schmitt, *Electrochemical investigations of Lead-Zirconate-Titanate Perovskites with small and high deviations from stoichiometry*, Zeitschrift fur Physikalische chemie neue folge, Bd. **130** (1982) S.97-107.
16. D.J. Wouters, G.J. Willems and H.E. Maes, *Electrical conductivity in ferroelectric thin films*, Microelectronic Engineering **29** (1995) 249.
17. R. Lohkamper, H. Newmann and G. Arlt, *Internal bias in acceptor-doped $BaTiO_3$ ceramics: numerical evaluation of increase and decrease*, J. Appl. Phys. **68** (1990) 4220.
18. D.D. Glowerand and R.C. Heckman, *Conduction-ionic or electronic in $BaTiO_3$*, J. Chem. Phys. **41** (1964) 877.
19. J. Maier and G. Schwitzgebel, *Electrochemical investigation of conductivity and chemical diffusion in pure and doped $SrTiO_3$ and $BaTiO_3$*, J. Solid. State. Chem. **58** (1985) 1.
20. B.A. Boukamp, *A Llinear Kromig-Frammers Transformation Test for Immittance data validation*, J. Electrochem. Soc. **142** (1995) 1885.
21. B.A. Boukamp, *A package for impedance/admittance analysis*, Solid State Ionics **18-19** (1986) 136.
22. B.A. Boukamp, *A non-linear least squares fit procedure for analysis of immitance data for electrochemical systems*, Solid State Ionics **20** (1986) 31.
23. B.A. Boukamp, M.T.N. Pham, D.H.A. Blank, H.J.M. Bouwmeester, *Ionic and electronic conductivity in lead-zirconate-titanate (PZT)*, Solid State Ionics **170** (2004) 239.

3

Synthesis and characterization of bulk PZT-Pt composites

3.1 Introduction

Ferroelectric ceramics are widely used in a variety of applications, ranging from capacitors, sensors, actuators to memory devices. The physical properties can be tailored to meet the requirements for a specific application, e.g., by varying the synthesis conditions, doping with a foreign element or adding a second phase. A survey was provided in Chapter 1 of this thesis.

Dual-phase metal-ferroelectric composites may offer improved mechanical properties, exploiting the ductility of the metallic phase. For example, enhancement in the fracture toughness was observed for PZT-Ag [1-3], PZT-Pd-Ag [4] and PZT-Pt composites [5]. In addition, the electrical properties are modified by the presence of the metal phase. The ferroelectric-paraelectric transition of PZT-Ag [6], PZT-Pd-Ag [4] shifts to higher temperatures in the presence of small amounts of Ag [13]. Most remarkable is the enhancement in the dielectric constant of PZT-based composites by dispersion with Pt [14]. The increase in the dielectric constant is attributed to the formation of multiple capacitors inside the composite. At metal concentrations just below the percolation threshold, the transition associated with formation of a continuous path for electrical transport, the capacity reaches extremely large values due to creation of, so to say, “infinitely large surface area for the capacitor electrodes and a small spacing between them”. The percolation threshold depends on the shape and spatial distribution as well as the size of the conducting particles relative to that of the insulating particles [15]. Materials exhibiting a high dielectric constant offer perspectives for application in super-capacitors or dynamic RAM.

In this chapter, we focus on the synthesis of PZT-Pt composites by different chemical routes. The dielectric and ferroelectric properties of the prepared composites are measured and the results obtained are discussed in view of their microstructures.

3.2 Experimental

3.2.1 Synthesis route

The following synthesis routes were used to prepare ceramic PZT-Pt composites. All three routes started with commercial PZT powder with a Zr:Ti ratio of 53:47 (grain size 1-2 μm, 3 N, TRS Ceramic USA), but differed in the way of introducing the Pt phase, as presented below. The concentration of Pt in the composites was varied between 0 and 30 vol.% percent.

3.2.1.1 Route I: Solid- state- reaction

PZT powder was mixed with commercial Pt powder (grain size 0.8-2 μm, 3N, ACROS Organics, USA) and wet-milled in ethanol using YSZ balls (Ø = 2 mm) for 5 h. After drying, the powder was pressed at 4000 MPa into a pellet with a diameter of 10 mm and a thickness between 1-2 mm. The thus obtained pellets were sintered at 1150 °C for 2 h in a closed crucible. During sintering, the pellet was embedded in $PbZrO_3$ powder to prevent PbO evaporation.

3.2.1.2 Route II: Chemical reduction

PZT powder was dispersed in water and stabilised with 15 wt. % of Darvan C (ammonium polymethacrylic acid, R.T Vanderbilt Co., Norwalk, USA). A solution of H_2PtCl_6, obtained via dissolution of Pt metal in aqua regia, was added to the suspension. A film evaporator was used to remove water and to keep the suspension homogeneous. The dried powder was reduced in a hydrogen gas atmosphere at 400 °C for 2 h to obtain metallic Pt. The pressing and sintering procedures were similar to those described in Section 3.2.1.1.

3.2.1.3 Route III: Sol-precipitation

An aqueous solution of H_2PtCl_6 was reduced to form nano-sized Pt particles by using hydrazine, sodium boronhydrate, methanol or sodium citrate as a reducing agent. More details about the synthesis of nano-sized Pt particulates by precipitation from aqueous solutions can be found in Refs. [9-11]. Polyvinylpyrolidone (PVP) was added as a protective agent against agglomeration. Subsequently, commercial PZT powder was added to the solution, which was stirred thoroughly to ensure good mixing. The composite powder was obtained by filtering the suspension through a 0.1 μm filter. PVP was burnt out at 400 °C for 2 h. The pressing and sintering procedures were similar to those described in Section 3.2.1.1. A flow chart for this scheme is given in Fig. 3.1.

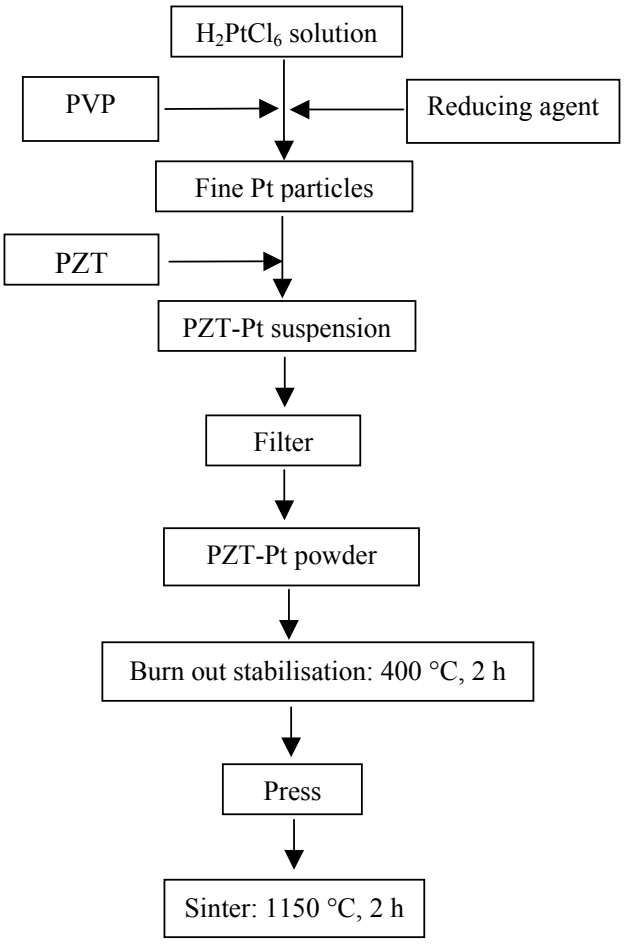

Fig. 3.1. Flow chart for the sol-precipitation method (Route III).

3.2.2 Measurement techniques

XRD analysis was performed on a Philips PANanalytical diffractometer using CuK_α radiation. The density of the disk-shaped samples was determined using the Archimedes method by immersion in water. The samples were examined by back-scattered electron imaging using scanning electron microscopy (SEM, JEOL 5800 JSM) and transmission electron microscopy (TEM, Philips CM30 Twin). Prior to the SEM investigations, the sample disks were first polished, using a 3 μm diamond emulsion, and then etched with a HF:HCl solution to reveal grain boundaries. Prior to electrical characterisation, samples were polished before sputtering of gold electrode layers on both sides. The dielectric loss and hysteresis loop measurements were carried out at room temperature at a frequency of 100 Hz, using a Radiant RT6000HVS-2 High Voltage test system at Yageo Europe B.V.

The dielectric constant and electrical conductivity of samples were measured by impedance spectroscopy, using a frequency response analyser (Solartron 1255, in combination with a Solartron Electrochemical Interface 1287). Impedance data were collected in the frequency range 1 Hz - 65 kHz, at 50 mV (rms) amplitude, from room temperature up to 500 °C. Data analysis was performed using the CNLS-fit program 'Equivalent Circuit' [19, 20].

3.3 Results and discussion

3.3.1 Phase analysis and microstructure

3.3.1.1 Solid state reaction (Route I)

Samples prepared by the solid state reaction (Route I) exhibited a bad homogeneity. The SEM investigations demonstrated the presence of large irregular agglomerates of Pt particles of about 10-50 μm, as shown in Fig. 3.2. The observations are attributed to poor mixing obtained by wet milling of the powders, which is being enhanced by the large difference in density between PZT (7.8 g/cm^3) and Pt (22.4 g/cm^3).

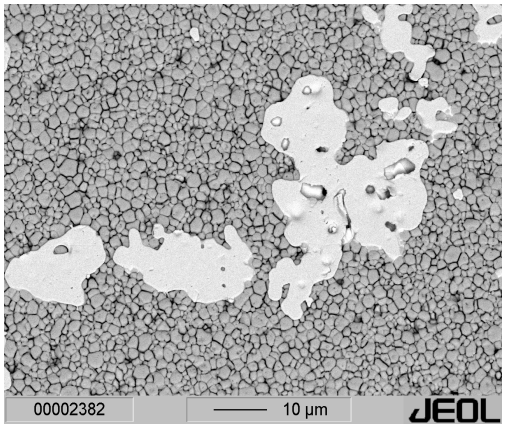

Fig. 3.2. SEM picture of PZT-Pt10 sample prepared by conventional route [7]. The bright phase indicates Pt agglomerates with irregular size of about 10-50 μm and the dark phase represents PZT matrix.

3.3.1.2 Chemical reduction (Route II)

To provide a better homogeneity and, through that, a smaller size of Pt particles inside the composite, a route was exploited based upon reduction of H_2PtCl_6 (Route II). This route

has been applied successfully for YSZ-Pt, YSZ-Pd [14] and $Ce_{0.8}Gd_{0.2}O_{1.9}$-Au [15]. The preparations yielded an additional phase, as confirmed by the XRD (see Fig. 3.3) and SEM investigations. In the SEM picture of Fig. 3.4, the bright coloured regions correspond to Pt, the grey phase to PZT, whereas the dark phase corresponds to the third unknown phase. No attempt was made to determine its composition and structure. Most likely, the acidic H_2PtCl_6 solution dissolved some of the lead from PZT, leaving a lead-deficient PZT phase.

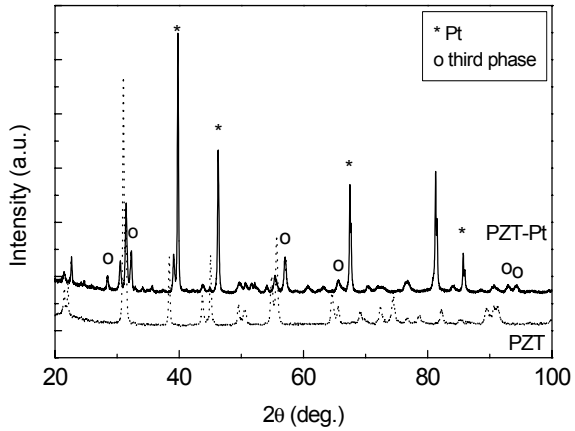

Fig. 3.3. Comparison of XRD diagrams observed for PZT-Pt prepared by chemical reduction (Route II) and pure PZT.

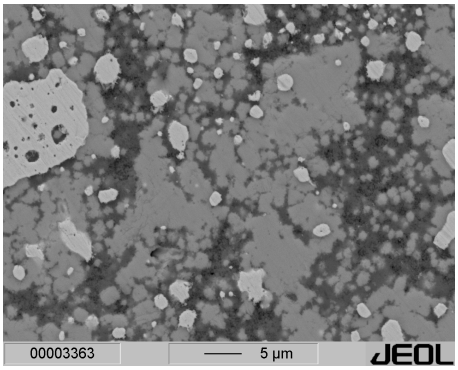

Fig. 3.4. SEM picture of PZT-Pt prepared by chemical reduction (Route II).

3.3.1.3 Sol-precipitation (Route III)

Using PVP as a stabilisation agent, the colloidal suspension of Pt nano-particles obtained after reduction forms a dark brown sol that is stable at room temperature for several months. As can be seen from Fig. 3.5a, the Pt sol consists of well-separated, nearly spherical particles with an average size around 5 nm. The TEM image was obtained by placing a drop of this sol onto a carbon grid, followed by evaporation of the solvent. The similarly prepared image of PZT-Pt powder is presented in Fig. 3.5b. Here, the Pt particles appear as grey particles covering the entire surface of a PZT grain. The clear colourless filtrate obtained upon filtering the PZT-Pt suspension suggests that all H_2PtCl_6 had been reduced to Pt and all Pt adsorbed on the PZT powder.

Figure 3.6 shows the XRD patterns of sintered monolithic PZT and the PZT-Pt composite with 10 vol.% Pt (henceforth denoted as PZT-Pt10). All reflections can be assigned to PZT and Pt, i.e., no evidence of third phase formation is found. This proves that no unwanted

side reactions occur between Pt and PZT in the composite and that the alkaline environment in the sol does not lead to decomposition of PZT. Note in Fig. 3.6 the splitting of the PZT peaks due to tetragonal distortion of the perovskite structure.

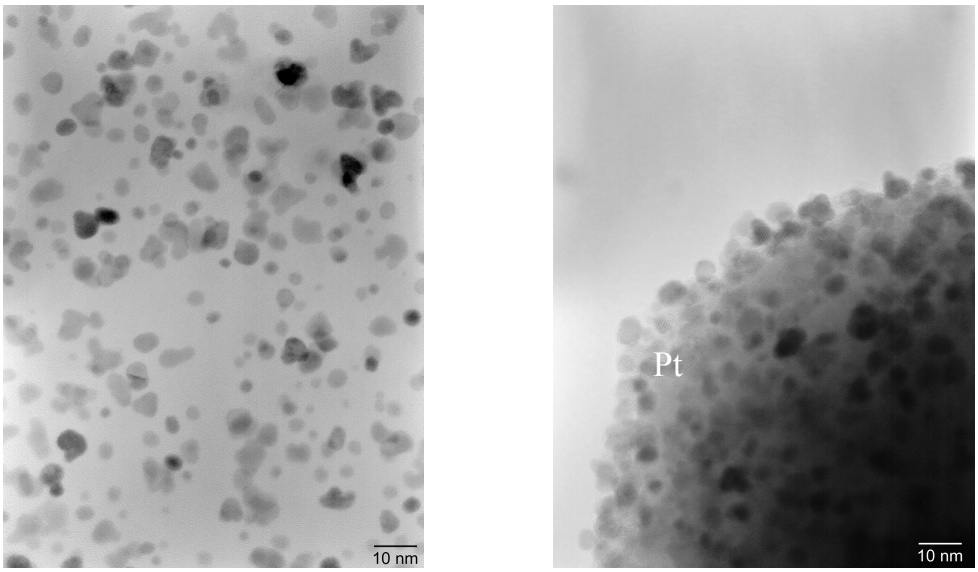

(a) *(b)*

Fig. 3.5. TEM picture of as-prepared Pt particles with PVP as protective agent (a) and as-prepared PZT-Pt mixture: Pt particles are adsorbed on PZT (b).

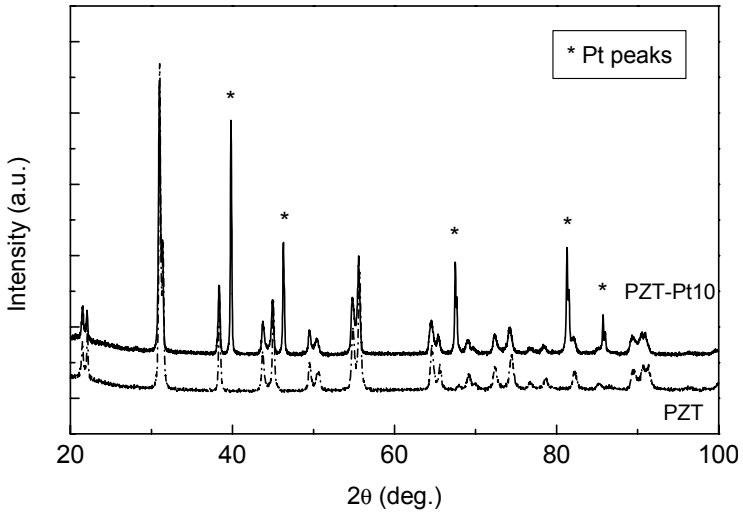

Fig. 3.6. XRD patterns of PZT and PZT-Pt10 samples prepared by sol-precipitation route (Route III).

The relative densities of the samples obtained by the sol-precipitation route are listed in Table 3.1. As can be seen, the density decreases with Pt content, but remains high and

above 95 %. The decrease in density may indicate that grain boundary motion is impeded by the presence of Pt in the composite.

Table 3.1. Relative densities of PZT-Pt composites with different Pt contents. The theoretical density of PZT is taken to be 7.6 g/cm^3.

Pt (vol.%)	0	5	10	15	20	25	28	30
Density (%)	99	97	97	96	95	95	95	95

SEM micrographs of sintered PZT and PZT-Pt10 specimens are presented in Figs. 3.7a and b, respectively. That of pure PZT shows large grains in the range of 5 -10 μm. As is apparent from Fig. 3.7b, the round-shaped Pt-particles are spread over the PZT surface with a preferred location at the grain junctions. The average size of PZT grains is estimated to be 2-3 μm, while that of Pt particles is between 100 and 500 nm.

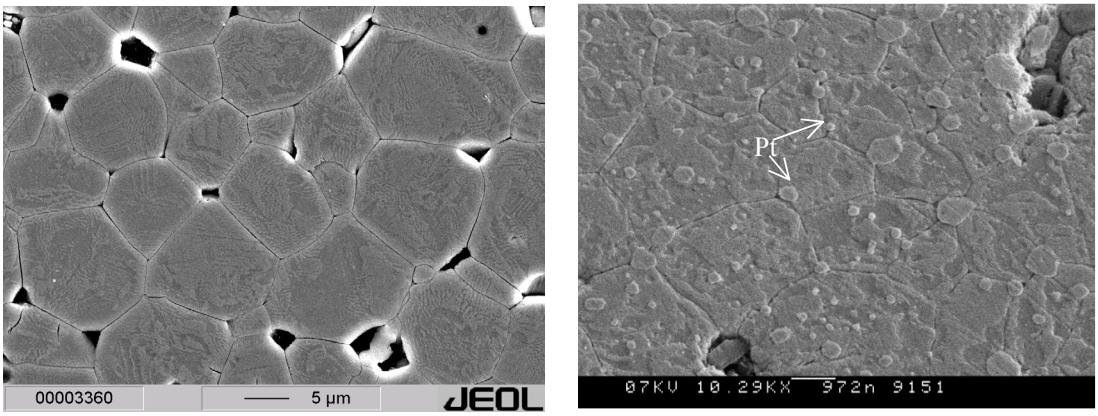

(a) *(b)*

Fig. 3.7. SEM picture of (a) pure PZT and (b) PZT-Pt10 composites, prepared by sol-precipitation route (Route III).

Even though the particle size of Pt in the sol is of the order of a few nm (see Fig. 3.5a), during sintering of the composite they grow to a few hundred nanometer (see Fig. 3.7b). This can be attributed to a very high mobility of Pt, which favours the agglomeration of Pt particles. When the Pt content increases, the shape of Pt particles changes from spherical to irregular aggregates (see Fig. 3.8). The average particle size increases from 2 μm for 15 vol.% Pt to 5 μm for 30 vol.% Pt. Meanwhile, the grain size of PZT decreases almost five times, from 5-10 μm in pure PZT (see Fig. 3.7a) down to 1-2 μm in PZT-Pt30 (see Fig 3.8b). The sample with 30 vol.% Pt already forms conductive paths as was con-

firmed by electrical measurements. The observed decrease in grain size of PZT with increasing Pt content can be explained by the two-phase system model [16]. During sintering, second-phase Pt particles tend to segregate at PZT grain boundaries. When such a boundary moves in order to enable grain growth, it must drag the second phase along with it, thereby slowing down the grain boundary motion, hence, impeding grain growth.

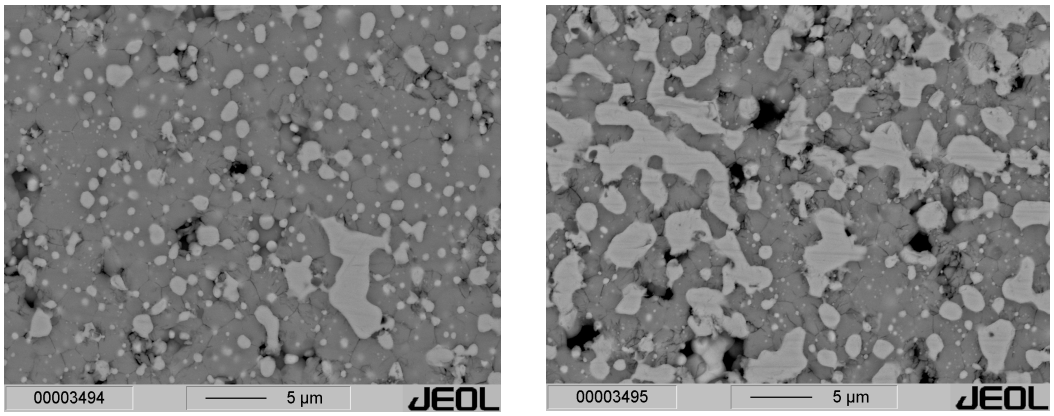

(a) *(b)*

Fig. 3.8. SEM picture of (a) PZT-Pt15 and (b) PZT-Pt30, prepared by sol-precipitation route (Route III).

Concluding this section on different routes for the preparation of PZT/Pt composites, the solid-state reaction route (Route I) leads to a poor homogeneity of samples showing large Pt aggregation. Chemical reduction (Route II) improves homogeneity and reduces the average size of Pt particles, but results in phase decomposition of PZT. Only the sol-precipitation route (Route III) provides both the proper phases and a homogeneous phase distribution. In the next section, we will present the electrical properties of samples prepared by this route.

3.3.2 Electrical properties

3.3.2.1 Dielectric constant

The apparent dielectric constant, ε, of the composites was calculated from the capacitance, *C*, using the well-known equation:

$$\varepsilon = \frac{Cd}{\varepsilon_0 S} \tag{3.1}$$

where d is the real sample thickness, S the geometrical electrode surface area, and $\varepsilon_o = 8.854\times10^{-12}$ F/m the permittivity of vacuum. Figure 3.9 shows the room temperature value of ε as a function of Pt content. The increase of ε with Pt content tends to follow a power law. A six times enhancement of ε is at composition 28 vol.% Pt over that observed for pure PZT. At 30 vol.% of Pt, the sample turned to be conductive as confirmed by measurement. The observed enhancement of ε with Pt content can be explained by the change in the effective values of d and S in Eq. (3.1) as a result of the dispersion of Pt inside PZT. The value of ε maximizes at near-percolative conditions. Dubrvov *et al.* [17] gave the following qualitative interpretation: each pair of nearby clusters of Pt inside PZT forms a capacitor, whose effective surface tends to infinity near the percolation threshold.

An effective-medium approximation (EMA) can be used to give a more quantitative interpretation. Several EMA models, among those proposed by Maxwell, Claussius-Mossoti, and Bruggeman [18], and percolation theory [19] can be used to model the observed divergence of ε with increase of Pt content in the composites. The effective-medium approximations consider a two-phase system as a random mixture of spherical grains, each grain being surrounded by a mixture of both phases that has the mean or effective value for the medium.

The first effective media for spherical inclusions were due to Maxwell. For dilute dispersions of spheres ($\phi \leq 0.1$) in a host matrix,

$$\varepsilon_m = \varepsilon_l \frac{1}{(1-3\phi)} \tag{3.2}$$

where ε_m is the effective permittivity of the composite, ε_l the permittivity of the host insulating medium, and ϕ the volume fraction of the conductive phase. The well-known Claussius-Mosseti relationship is expressed as:

$$\frac{\varepsilon_m - \varepsilon_l}{\varepsilon_m + 2\varepsilon_l} = \phi \frac{\varepsilon_h - \varepsilon_l}{\varepsilon_h + 2\varepsilon_l} \tag{3.3}$$

where ε_h is the dielectric constant of the more conductive phase. Upon assuming that the conductive phase has an infinite dielectric constant, i.e. $\varepsilon_h = \infty$, Eq. (3.3) reduces to:

$$\varepsilon_m = \varepsilon_l \frac{2\phi+1}{1-\phi} \tag{3.4}$$

When the terms ε_m, ε_h, ε_l are replaced by σ_m, σ_h and σ_l, respectively, Eq. (3.4) corresponds to the famous Maxwell-Wagner equation for conductivities of two-phase composites. In this case, the composites can be visualized as built-up of a space-filling array of coated spheres.

Bruggeman's asymmetric media equation can be presented as:

$$\frac{(\varepsilon_m-\varepsilon_l)^3}{\varepsilon_m}=(1-\phi)^3\frac{(\varepsilon_l-\varepsilon_h)^3}{\varepsilon_l} \tag{3.5}$$

and for the extreme case of a conductor-insulator composite, one can transform Eq.(3.5) to:

$$\varepsilon_m=\frac{1}{(1-\phi)^3}\varepsilon_l \tag{3.6}$$

Similarly, the general Bruggeman symmetric equation:

$$\phi\frac{\varepsilon_h-\varepsilon_m}{\varepsilon_h+2\varepsilon_m}+(1-\phi)\frac{\varepsilon_l-\varepsilon_m}{\varepsilon_l+2\varepsilon_m}=0 \tag{3.7}$$

can be simplified to:

$$\varepsilon_m=\varepsilon_l\frac{1}{(1-3\phi)} \tag{3.8}$$

hence, reducing to the simple Maxwell equation. If the dielectric constant is replaced by the conductivity, both Maxwell's and Bruggeman's symmetric equations predict an infinite conductivity, corresponding to an insulator-conductor transition at $\phi_c = 0.33$.

In practice, effective media theories work best for lower values of ϕ, where the spheres are further apart. When the system consists of conducting spheres, of just sufficient size to touch their nearest neighbours, randomly placed on the sites of a 3D lattice, it is more usually described by percolation theory. The volume fraction at which the more conductive phase is found to produce a conductive percolative path or network throughout the system equals 0.16. Below this so-called percolation threshold, the dielectric constant of the composite follows the scaling law [27]:

$$\varepsilon_m=\left(\frac{\phi_c}{\phi_c-\phi}\right)^s\varepsilon_h \tag{3.9}$$

where ϕ_c presents the critical volume fraction at which percolation occurs and s is called the critical exponent.

In Fig. 3.9, we present data of fitting the EMA and the percolation equations to the experimental data. It is seen that Bruggeman's symmetric equation and the simple Maxwell equation give a fair agreement with the experimental data. Both equations coincide due to the assumption $\varepsilon_h = \infty$. The best fit, however, is obtained for the percolation equation, Eq.(3.9), using the following fit parameters: $\phi_c = 0.29 \pm 0.01$, $s = 0.50 \pm 0.05$. According to site-bond percolation theory, $\phi_c = 0.16$ is obtained when all particles occupy a regular lattice and nearest-neighbours are well connected, shifting to higher values if grain-to-grain contact fails due to incomplete wetting. It should be noted that $\phi_c = 0.29$ is close to the percolation threshold value $\phi_c = 0.33$ predicted by the Bruggeman symmetric and/or the Maxwell equation. The fitted value for the critical exponent s is found somewhat lower, compared to $s = 0.76$ predicted by site-bond percolation theory. The available theories predict that close to the percolation threshold ϕ_c very high dielectric constants may be obtained. In practice, however, this may be difficult to achieve. Local inhomogeneities in the distribution of Pt and size effects may cause failure at compositions lower than ϕ_c due to electrical shortcut.

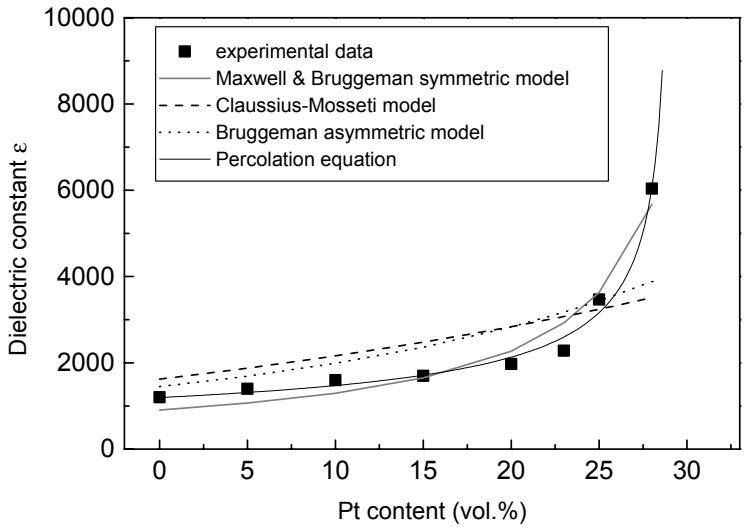

Fig. 3.9. Dielectric constant of PZT-Pt composites as a function of Pt content. The drawn lines represent the fit of the experimental data to Eqs. (3.2), (3.4), (3.6), (3.8) and (3.9).

3.3.2.2 Dielectric loss

In Fig. 3.10, the dielectric loss measured at 100 Hz is plotted as a function of Pt content. With Pt addition, the dielectric loss increases from 0.8 % for pure PZT to 2.2 % for PZT-Pt25. The dielectric loss measured for bulk ceramic PZT is in good agreement with results reported in literature [20, 21].

The loss tangent [i] ($\tan\delta$) is the quotient of the real and imaginary components of the impedance. To a first approximation, the dielectric loss can be described in terms of a simple equivalent parallel *RC* circuit, and thus can be represented as [22]:

$$\tan\delta = \frac{\sigma}{2\pi f \varepsilon \varepsilon_0} \tag{3.10}$$

where σ is the conductivity, f the frequency and ε the relative dielectric constant of the material. Equation (3.10) shows that the loss tangent is a function of conductivity σ, frequency f and permittivity ε. Accordingly, at fixed frequency, changes in the loss factor of the PZT/Pt composites with increasing Pt content are balanced by corresponding changes in σ and ε. Accurate analysis of impedance spectra of PZT/Pt composites obtained above ~150 °C made clear that the conductivity in Eq. (3.10) is a lumped parameter, comprising both ionic and electronic contributions [23].

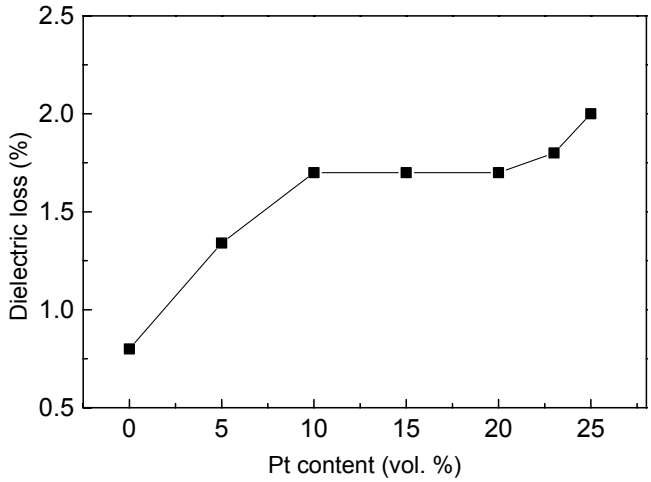

Fig. 3.10. Dielectric loss measured at 100 Hz of PZT-Pt composites as a function of Pt content.

[i] The dielectric loss is defined as $\tan\delta = \frac{\varepsilon''}{\varepsilon'}$ and is related to the power dissipation of an insulating material. (See also Chapter 1 of this thesis).

3.3.2.3 Hysteresis loops

Ferroelectric hysteresis loops measured for samples with Pt content in the range 0-23 vol.% are shown in Fig. 3.11a. Measurements on samples with higher Pt contents were not possible due to break down as saturation was neared. All samples show quite square hysteresis loops, suggesting a good grain size uniformity as well as homogeneity. The observed high symmetry of the hysteresis loops further indicates the absence of space charge layers at the electrodes. The dielectric response *dP/dE* (derivative of the hysteresis loop) of the measured hysteresis loops are shown in Fig. 3.11b.

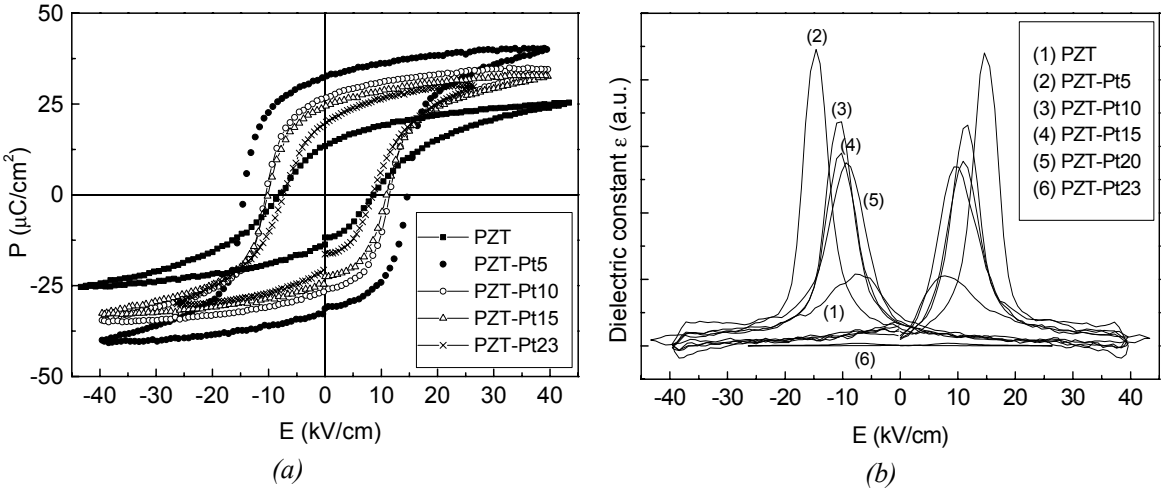

Fig. 3.11. (a) Hysteresis loops of PZT and PZT-Pt composites with different Pt contents, and (b) calculated slopes of the hysteresis loops.

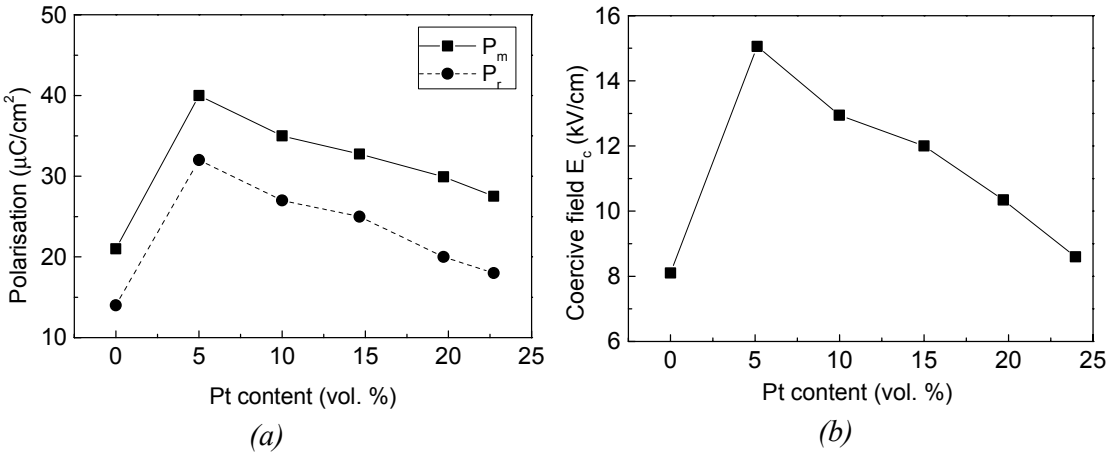

Fig. 3.12. Dependence of maximum and remanent polarisation (a) and coercive field (b) in PZT-Pt composites on the Pt content.

The variation of the remanent polarisation with Pt content is presented in Fig. 3.12a. The value increases from 15 μC/cm^2 observed for pure PZT to a maximum value of 34 μC/cm^2 for PZT-Pt5, decreasing upon further addition of Pt to 18 μC/cm^2 for PZT-Pt23. The results are in good agreement with observations made by Ning *et al.* [7]. The curve obtained departs from a linear mixing rule. This is attributed to a major contribution of space charge polarization at the PZT/Pt interfaces to the total polarization. Such a contribution is predicted to be proportional to the specific surface area A_{spec} of the inclusions. Assuming spherical Pt inclusions with a diameter d, the following relationship holds [24],

$$A_{spec} = \frac{2\pi}{d}\phi_{Pt}(1-\phi_{Pt}) \tag{3.11}$$

In the experimental range of $\phi_{Pt,}$ Eq. (3.11) thus predicts an increase of A_{spec} with $\phi_{Pt.}$ However, as can be judged from Figs. 3.7 and 3.8, the average Pt grain size is not constant but rather increases with Pt content, from a value of 500 nm for 10 vol.% Pt to 5 μm for 30 vol.% Pt. Hence, the actual contribution of space charge polarization at the interface of PZT/Pt will diminish at higher Pt contents. The coercive field increases from 8.5 kV/cm for pure PZT, to 14.5 kV/cm for PZT-Pt5 and to 9.5 kV/cm for PZT-Pt23 (Fig. 3.12b).

The dielectric response, dP/dE, which relates to the dielectric constant ε, can be used to estimate the tunability, defined by:

$$tunability = \frac{\varepsilon_{(E\neq 0)} - \varepsilon_{(E=0)}}{\varepsilon_{(E\neq 0)}} \times 100\% \tag{3.12}$$

The tunability is highest for PZT-Pt5, reaching a value of 90 %, compared to 45 % for pure PZT. The larger dielectric tunability exhibited by the composites compared to pure PZT is promising for voltage-tunable microwave devices such as resonators, filters and phase shifters [25, 26].

3.3.2.4 Impedance spectroscopy

Typical impedance data obtained for the PZT-Pt composites measured as a function of temperature are presented in Fig. 3.13. The shape of the impedance diagrams changes from an almost purely capacitive behaviour at room temperature to a slightly depressed semicircle at elevated temperature, arising due to onset of electronic conductivity. CLNS-analysis of the high temperature data resulted in a simple equivalent circuit: a parallel combination of the dielectric capacitance response $Q_{diel,}$ the electronic resistance $R_{el,}$ and the blocked ionic path presented by a series combination of the ionic resistance R_{ion} and capacitance

due to interfacial polarization Q_{int}. The circuit description code (CDC) reads [19]: (Q_{diel} R_{el} [R_{ion} Q_{int}]).

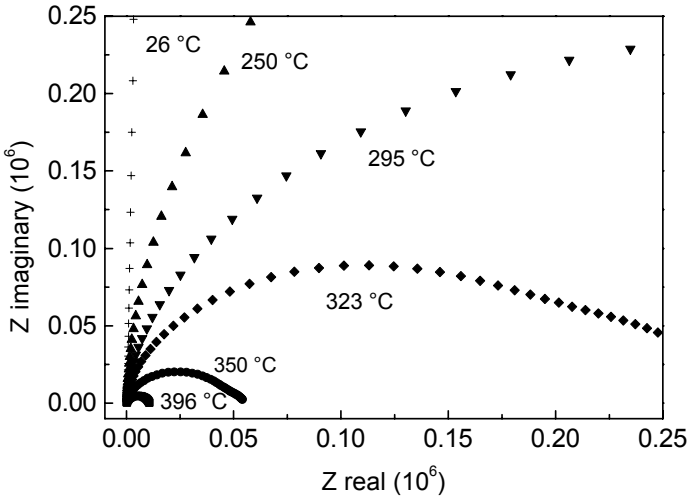

Fig. 3.13. Impedance spectra for PZT-Pt10 measured under air at different temperatures.

In the CNLS-fit analysis, the bulk capacitance showed non-ideal behaviour and had to be replaced by a constant phase element (CPE) with admittance:

$$Y(\omega) = Y_{\text{O}}(j\omega)^n \tag{3.13}$$

where j is the imaginary unit, ω the angular frequency and n the frequency power. For n = 1, this represents a pure capacitance. The value of n was found to decrease from almost 1 at room temperature to about 0.95 around the Curie temperature. To calculate the pseudo dielectric constant, a different representation of Eq. (3.13) was used:

$$Y(\omega) = (jY_n\omega)^n \tag{3.14}$$

with $Y_n = Y_o^{1/n}$. The dielectric constant was calculated according to:

$$\varepsilon = \frac{Y_n \times d}{\varepsilon_0 \times S} \tag{3.15}$$

As seen from Fig. 3.14, the dielectric constant maximizes at the Curie temperature T_{C}. For pure PZT, T_{C} is found at 400 °C, slightly increasing upon addition of Pt up to a temperature of 410 °C for PZT-Pt25. The shift in Curie temperature is tentatively explained by internal stress [27]. It is unlikely that the shift is due to incorporation of Pt into the PZT lattice because of the large difference in electro-negativity of Pt^{2+} ions (2.28) and Ti^{4+} (1.54) or Zr^{4+} (1.33) ions. The difference in the thermal expansion coefficients of PZT

(13×10^{-6}/ ^{0}C) and Pt (9×10^{-6}/ ^{0}C) may cause high tensile stress in the PZT matrix after sintering.

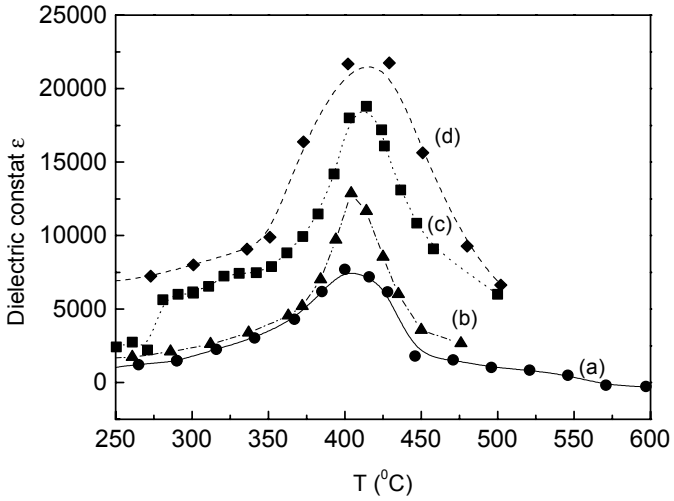

Fig. 3.14. Effect of Pt content on the Curie temperature of PZT-Pt composites: monolithic PZT (a), PZT-Pt5 (b), PZT-Pt20 (c), PZT-Pt25 (d).

Figure 3.15 shows the temperature dependence of the electronic conductivity for PZT-Pt5. Clearly two different regions with activated behaviour can be discerned. The activation energy is 0.7 eV, increasing to 1.14 eV below T_C. The transition region to low temperature-activated behaviour coincides with the width of the Curie peak in the dielectric constant. Similar observations have been made for pure PZT and the other PZT-Pt composites. For pure PZT, the results are consistent with those obtained by Las *et al.* [28], who found an activation energy of 0.71 eV for $T > T_C$ increasing to 1.1 eV for $T < T_C$.

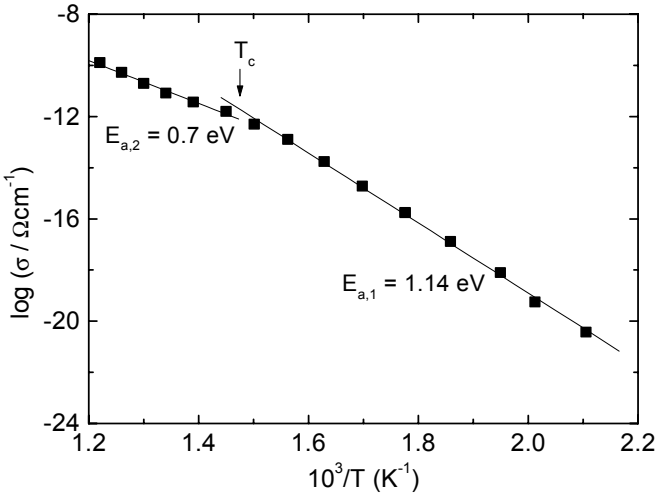

Fig. 3.15. Arrhenius plot of the electronic conductivity of PZT-Pt5 sample.

Table 3.2. Activation energies of the electronic conductivity of PZT and PZT-Pt composites.

	PZT	PZT-Pt5	PZT-Pt20	PZT-Pt25
$E_{a,1}$(eV)	1.22	1.14	1.05	1.0
$E_{a,2}$ (eV)	0.85	0.7	0.88	0.86

Activation energies for PZT and PZT/Pt composites obtained in this study are listed in Table 3.2. The decrease in activation energy observed upon addition of Pt in PZT is tentatively assigned to the role the space charge regions at the PZT/Pt interface, providing a faster pathway for conduction of electron holes.

3.4 Conclusions

Dual-phase PZT-Pt composites can be prepared successfully by the sol-precipitation route, in which PZT powder is wet mixed with a sol containing Pt nano-particles. The use of a suitable stabilization agent prevents agglomeration of the Pt particles in the sol. The wet mixing ensures a homogenous phase distribution. After sintering, no decomposition of PZT is traced. The presence of the dispersed Pt significantly reduces grain growth of PZT.

The dielectric constant of the PZT-Pt composites at room temperature increases with increasing Pt content, reaching a 6-times enhancement at 28 vol.% of Pt relative to that observed for bulk ceramic PZT. The observed enhancement of the dielectric constant with increase of the Pt content in the composites can be fitted with either the Maxwell and Bruggeman symmetric equations or the normalized percolation equation. Both the polarisation and the coercive field are found maximum at 5 vol.% of Pt. The observations are tentatively explained by the role of space charge at the PZT/Pt interface in the composites and the diluting effect of non-ferroelectric Pt phase. The dielectric constant is found maximum at the Curie temperature T_C, which is found to range for the composites between 400-410 °C. Above T_C, the activation energy for electronic conduction is significantly lowered, suggesting a change in mechanism for the transport of electron holes.

References

1. H.J. Hwang, M. Yasuoka and M. Sando, *Fabrication, Sinterability, and Mechanical Properties of Lead Zirconate Tinatate/Silver Composites*, J. Am. Ceram. Soc. **82** (1999) 2417.
2. G.H. Maher, *Effect of Silver Doping on the Physical and Electrical Properties of PLZT Ceramics*, J. Am. Ceram. Soc. **66** (1983) 408.
3. D.H. Pearce and T. W. Button, *Processing and Properties of Silver/PZT Composites*, Ferroelectrics **228** (1999) 991.
4. Y. Sato, H. Kanai and Y. Yamashita, *Effect of Silver and Palladium Doping on the Dielectric Properties of $0.9Pb(Mg_{1/3}Nb_{2/3})O_3$-$0.1PbTiO_3$ Ceramic*, J. Am. Ceram. Soc. **79** (1996) 261.
5. H.J. Hwang, K. Tajima and M. Sando, *Fatigue-free PZT-based Nanocomposites*, Key Engineering Materials **161-163** (1999) 431.
6. H.J. Hwang, T. Nagai and T. Ohji, *Curie Temperature Anomaly in Lead Zirconate Titanate/Silver Composite*, J. Am. Ceram. Soc. **81** (1998) 709.
7. N. Duan, J.E. ten Elshof and H. Verweij, *Enhancement of Dielectric and Ferroelectric Properties by Addition of Pt Particle to a Lead Zirconate Titanate Matrix*, Appl. Phys. Lett. **77** (2000) 3263.
8. A. Malliaris and D.T. Turner, *Influence of Particle Size on the Electrical Resistivity of Compacted Mixtures of Polymeric and Metallic Powders*, J. Appl. Phys. **42** (1971) 614.
9. P.R. Van Rheenen, M.J. McKelvy and W.S. Glaunsinger, *The Synthesis of Different Platinum Particle Geometries by the Chemical Reduction of Chloroplatinic Acid*, Solid State Communications **57** (1986) 865.
10. D.N. Furlong, A. Launikonis and W.H.F. Sasse, *Colloidal Platinum Sols*, J.Chem.Soc., Faraday Trans. 1 **80** (1984) 571.
11. D.G. Duff, T. Mallat, M. Schneider and A. Baiker, *Catalyst Derived from Polymer-Stabilised Colloidal Platinum: Effects of Support and Calcinations on the Catalytic Behaviour in Hydrogenation*, App. Catalysis A: General **133** (1995) 133.
12. B.A. Boukamp, *A package for impedance/admittance data analysis*, Solid State Ionics **18-19** (1986) 136.
13. B.A. Boukamp, *A Nonlinear Least Squares Fit procedure for analysis of immittance data of electrochemical systems*, Solid State Ionics **20** (1986) 31.
14. M. Hendriks, *Solid state super-capacitors based on metal/yttria-stabilised zirconia composites*, PhD Thesis, University of Twente, 2001.
15. E. Romer, *Amperometric NO_x-sensor for combustion exhaust gas control*, PhD Thesis, University of Twente, 2001.
16. R.B. Atkin, *Sintering and ferroelectric properties of Lead Zirconate Titanate Ceramics*, PhD Thesis, University of California, 1967.

17. V.E. Dubrov, Zh. Eskp. Teor. Fiz. **70** (1876) 2014.
18. D.S. McLachlan, *Analytical functions for the dc and ac conductivity of conductor-insulator composites*, J. Electroceramics **5** (2000) 93.
19. M. Sahimi, *Application of percolation theory*, Taylor and Francis Ltd., 1994.
20. P.K. Sharma, Z. Ounaies, V.V. Varadan, V.K. Varadan, *Dielectric and piezoelectric properties of microwave sintered PZT*, Smart Mater. Struct. **10** (2001) 878.
21. S. Li, W. Cao and L.E. Cross, *The extrinsic nature of nonlinear behavior observed in lead zirconate titanate ferroelectric ceramic*, J. Appl. Phys. **69** (1991) 7219.
22. W.D. Kingery, H.K. Bowen and D.R. Uhlmann, *Introduction to ceramics*, 2nd edition, John Wiley & Sons, 1976.
23. B.A. Boukamp, M.T.N. Pham, D.H.A. Blank and H.J.M. Bouwmeester, *Ionic and electronic conductivity in lead-zirconate-titanate (PZT)*, Solid State Ionics, **170** (2004) 239.
24. M. Sahimi, G.R. Gavalas and T.T. Tsotsis, *Statistical and continuum models of fluid-solid reactions in porous media*, Chem. Eng. Sci. **45** (1990) 1443.
25. L. Sengupta, *Ceramic ferroelectric composite material-BSTO-Magnesium based compound*, Warwick, Md., Appl. No. 528629, United States Patent, Patent No. 5635434, Jun. 3, 1997.
26. H.N. Al-Shareef, D. Dimos, M.V. Raymond and R.W. Schwartz, *Tunability and Calculation of the dielectric constant of capacitor structures with Interdigital Electrodes*, J. Electroceramics **1-2** (1997) 145.
27. M. Taya, S. Hayashi and A.S. Kobayashi, *Toughening of a Particulate Reinforced Ceramic-Matrix Composite by Thermal Residual Stress*, J. Am. Ceram. Soc. **73** (1990) 1382.
28. W.C. Las and P.D. Sapgnol, *Electrical Characterisation of Lead Zirconate Titanate Prepared by Organic Solution Route*, Ceramics International **27** (2001) 367.

4

Pulsed laser deposition of PZT-Pt thin film composites

4.1 Introduction

As presented in Chapter 3, dispersion of Pt in $PbZr_{0.53}Ti_{0.47}O_3$ (PZT) phase enhances the di-and ferroelectric properties of the bulk composites. The enhancement of the dielectric constant is most significant in the vicinity of percolation threshold fraction (or critical volume fraction). The percolation threshold was found dependent on the shape, spatial distribution as well as the size of the conducting particles relative to that of the insulating particles [1, 2]. In bulk samples it is difficult to control the particle size of both PZT and Pt due to massive growth of grains at high sintering temperature. Even though 5-10 nm sized-Pt particles were used as a starting material, micron-sized Pt aggregates appeared in the sintered samples after sintering at 1150 °C. An alternative way to obtain the particle size of both phases in nanometer scale is to fabricate the material in the form of thin film.

There are various ways to make composite films, including chemical methods such as sol-gel method [3-5], suspension spraying [6], liquid-phase deposition [7] and physical methods such as sputter deposition [8-10], electron beam deposition [11] and pulsed laser deposition (PLD) [12-17]. Among these techniques, PLD is well known as a method to provide a stoichiometric transfer from target to thin films. With a variety of tuneable deposition parameters, high deposition rates and high kinetic energies of the adatoms, it permits a high degree of tailoring the microstructure of the film.

The principle of PLD is illustrated through Fig. 4.1. In general, the formation of a thin film by pulsed laser deposition includes three major processes as follows:

- The ablation of target.

Under the interaction of the laser beam material is removed from the target. A plasma is formed, which contains various kinds of species such as atoms, ions, molecules and even large aggregates. In this stage, the interaction between the laser beam and the target is the most important factor, since it determines the amount of ablated materials, their existence

type and kinetic energy. The appropriate value for laser energy density hence depends on the chemical and physical properties of the target.

- The transportation of ablated material towards the substrate.

After being removed from the target, the ablated species accelerate forwards and gain huge kinetic energy (from several eV up to 10^3 eV). During the transport, they interact dynamically and chemically with each other and with gas molecules in the chamber. The kinetic energies of the ablated species thus are strongly affected by the ambient gas pressure and the distance from the target to the substrate.

- The deposition and growth of material on the substrate.

The ablated species will be adsorbed upon arriving at the substrate, resulting in formation of a thin layer of material. In this process, the substrate properties, the substrate temperature and the laser frequency play important roles on film growth.

The nucleation and growth of the film actually involves several processes, including diffusion, agglomeration, dissociation and re-evaporation of the adatoms. The growth mechanism is thermodynamically governed by the surface interaction between film and substrate, but it also can be altered kinetically by changing the supersaturation through the substrate temperature and arrival rate of the adatoms. All the mentioned processes influence the growth and hence the properties of the film.

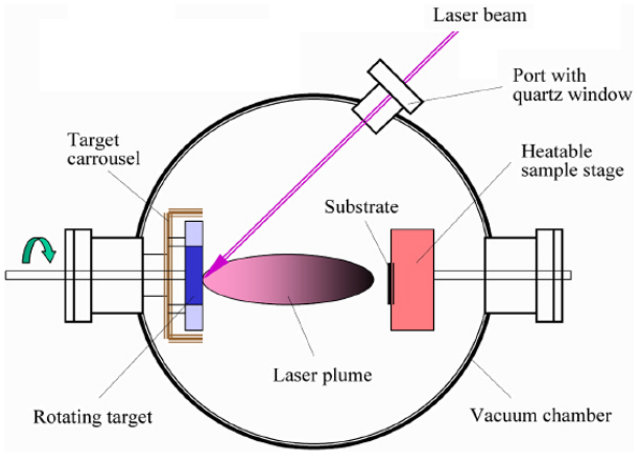

Fig. 4.1. The sketch of a PLD system.

In order to make a composite thin film by PLD one can use a composite target or alternating targets. The component compounds are ablated simultaneously in the former and in

sequence in the latter method. In order to get a homogeneous film, and especially homogeneous phase dispersion, using a composite target is simpler and also more effective. In case of metal-oxide composites, since oxides and metals ablate differently [18], care should be taken to have the desired composition in the thin film. The ablation threshold, which is defined as the lowest laser fluence to remove a substantial amount of material, is quite low for oxides, for e.g. 0.6 J/cm^2 for PZT but very high for metals, e.g. around 4 J/cm^2 for Pt [19].

In this chapter we first study the ablation process of the composite PZT-Pt target. The key-role of the laser energy density on the surface modification of the target and the resulted composition of the film will be discussed. Next we will investigate the influence of other deposition parameters such as the ambient gas pressure, the target-to-substrate distance, the substrate temperature and the laser frequency on the structural properties of films. Understanding the deposition process is important to minimize PbO loss, prevent pyrochlore (non-ferroelectric) phase during film growth and control the film microstructure.

4.2 Experimental

The laser ablation experiments were carried out with a KrF excimer (λ = 248 nm) laser beam (Compex 205, Lambda Physik) with pulse duration of 25 ns (FWHM). The $PbZr_{0.53}Ti_{0.47}O_3$ and $PbZr_{0.53}Ti_{0.47}O_3$-Pt targets were obtained after sintering the green pellets at 1150 °C for 2 h (for more details see Chapter 3). The average particle sizes of PZT and Pt in the target are 5-10 μm and 1-10 μm, respectively. One-side polished, single-crystal (001) $SrTiO_3$ substrates were used in experiments. The substrate temperature (T_s) was held constant during deposition and ranged from 400 °C to 700 °C. The target-to-substrate distance (d) was varied from 35 to 65 mm. The energy density of the laser (E) was in the range of 1.5 J/cm^2 to 6 J/cm^2. The laser frequency (f) was varied from 1 Hz to 10 Hz. Films were deposited in oxygen environment with the ambient pressure (pO_2) ranging from 0.05 mbar to 0.4 mbar. After deposition, films were cooled down to room temperature in an oxygen flow. In some cases, films were in-situ annealed in the deposition chamber or ex-situ annealed in a PbO environment to promote the crystallinity of PZT phase.

The morphology and chemical composition of the ablated areas in the targets were investigated by scanning electron microscopy (SEM) and energy dispersive X-ray (EDX), respectively. The crystal structure of films were analysed by a X-ray diffractometer (XRD) using

CuK_α wavelength. The film microstructure was examined using a SEM and an atomic force microscopy (AFM). The film thickness was quantified using a cross-section image obtained by SEM. The film composition was determined by an X-ray fluoresence (XRF) and X-ray photoelectron spectroscopy (XPS).

4.3 Results and discussion

4.3.1 Target ablation

The formation of a thin film by pulsed laser deposition is initialised by the ablation of the target under interaction with laser beam. The surface modification during laser ablation of PZT target has been discussed by Auciello *et al.* [20]. It involves the formation of cones on the surface, which reduces the deposition rate at the beginning of the ablation, accompanied with a marked decrease in plume size. Generally, the shielding effect of vaporisation-resistant impurities is responsible for cone formation. In the PZT target, it is due to the formation of Zr (and/or Ti)-rich regions, resulting from the incongruent melting and solidification of PZT. In a PZT-Pt target, one can regard Pt as "an impurity" having a higher melting point and lower laser energy absorption, resulting in less preferential ablation. A question hence arises: is the ablation of PZT-Pt stable with time?

4.3.1.1 Time dependence of the plasma

The ablation of PZT-Pt targets took place in high vacuum of 10^{-6} mbar at a laser frequency of 1 Hz. The same area of the target was irradiated during ablation. The produced plasma was pictured after every minute (i.e. 60 pulses) by a digital camera. As an example, we show the pictures obtained for PZT and PZT-Pt15 targets in Figs. 4.2 and 4.3, respectively. The laser energy density used was 2.5 J/cm^2 and the laser spot size *(A)* was 3 mm^2 in both cases. From Fig. 4.2 it can be seen that the plasma observed for PZT shrinks after 1 minute of ablation but later becomes quite steady. The time-dependence of the plasma is more noticeable for the PZT-Pt15 target (see Fig. 4.3). The produced plasma gradually shrinks with time and after 5 minutes of ablation the plasma size reduced by almost a factor of two.

The decrease of the plasma size was more evident with increasing Pt content in the targets. Beside the Pt content, the laser energy density *(E)* under which the target is exposed also influence the stability of the plasma. In Fig. 4.4 we illustrated the time-dependence of the plasmas produced from PZT-Pt18 target under different *E*. For *E* ranging from 2.5 J/cm^2 to

3.5 J/cm^2 the plasma size change significantly with time. Meanwhile, for E higher than 4 J/cm^2 it is time independent.

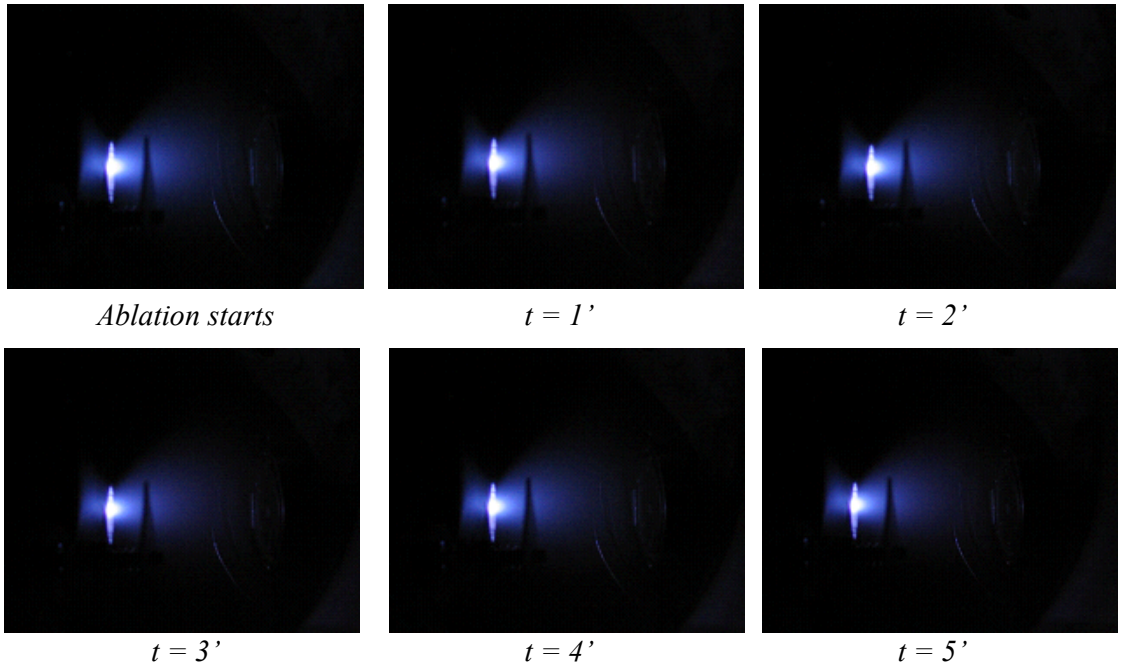

Fig 4.2. Plasmas produced from PZT target using E = 2.5 J/cm^2 (A = 3 mm^2). The ablation time (t) is indicated below each image.

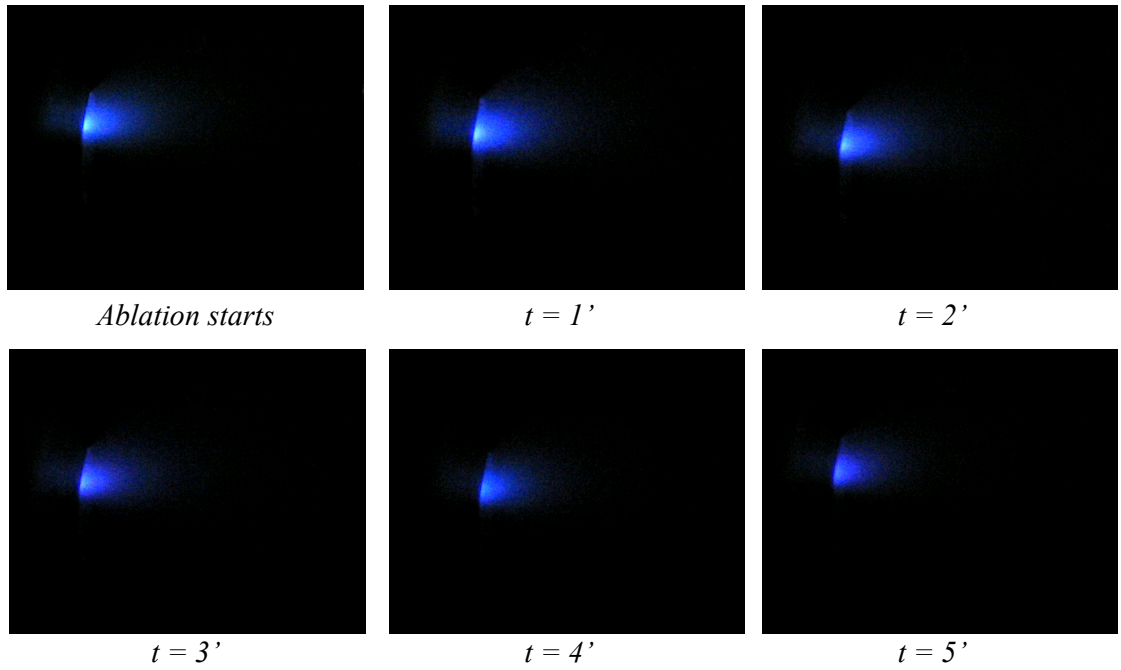

Fig. 4.3. Plasmas produced from PZT-Pt15 target using E = 2.5 J/cm^2 (A = 3 mm^2). The ablation time (t) is indicated below each image.

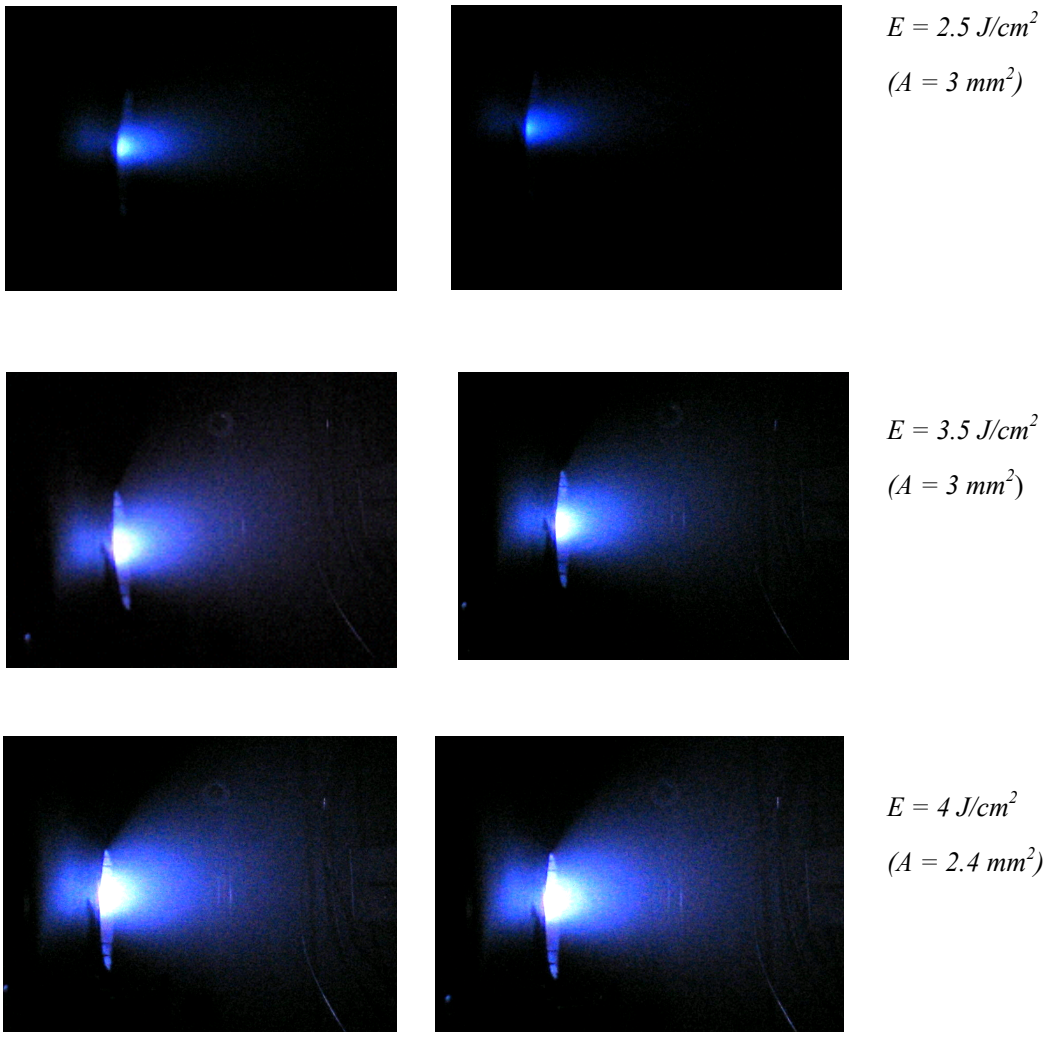

Fig. 4.4. Plasma produced from PZT-Pt18 at different energy density. The ablation time (t) is indicated below images.

According to Ref. [20], the time-dependence of PZT plasma in the initial stage is considered due to surface modification of the target, resulting from incongruent melting and solidification of PZT. However, as soon as the target surface reaches a steady state, the plasma becomes stable. The above observation indicates that under mentioned conditions the steady state of PZT plasma is obtained after approximately 1 minute (corresponding to 60 pulses). A pre-ablation of the PZT target before deposition is therefore strongly recommended.

For PZT-Pt targets, since the ablation does not cease after 1 min at E = 2.5 J/cm^2, another factor but the incongruent melting of PZT should be responsible for surface modification of the target. The most likely one is the different ablation behaviour of Pt with respect to PZT. As mentioned in Section 4.1, the energy required to ablate a metal is higher than to ablate an oxide. While the threshold ablation for PZT is only 0.6 J/cm^2, the threshold ablation for Pt is up to 4 J/cm^2. Since at E = 2.5 J/cm^2 PZT is preferentially ablated over Pt, more Pt than PZT is left in the target after every pulse. As a consequence, a preferential enrichment of Pt over PZT in the target is expected, transforming the target surface to more metallic with time.

Another evidence of surface modification in PZT-Pt targets is the change of the plasma colour with time when the deposition ambient is changed from vacuum to oxygen. In oxygen atmosphere, the plasma consists of a white shell and a blue core, which actually is due to oxidized and non-oxidized species, respectively [20]. What we observed for ablation at low energy densities is the gradual decrease of the white shell relative to the blue core with ablation time. The decrease of the white shell hence implies the presence of more non-oxidized Pt species in the plasma.

The above reasoning can be applied to explain why the PZT-Pt plasmas are time-independent at high energy densities. When E is above the threshold ablations of both PZT and Pt ($E \geq 4$ J/cm^2), the difference in preferential ablation of PZT and Pt is minimised. Because no modification of the target composition occurs, the stability of the plasma is afforded. Using energy densities above the threshold ablation of Pt keeps the plasma size unchanged for at least 30 minutes.

4.3.1.2 Energy density dependence of PZT and Pt contents in the target upon ablation

To confirm the dependence of target surface modification on laser energy density, we analysed the microstructure of the ablated targets at different laser energy densities.

SEM images of the ablated areas after 5 minutes of ablation (i.e. 300 pulses) at different E are shown in Fig. 4.5 for PZT and PZT-Pt15 targets. All images show structure of pillars that protrude from the surface. For PZT target, the pillar patterns exhibit almost no change with changing energy density (see Fig. 4.5 a-c). At higher E, there is only a slight increase in pillar length, reflecting a larger removal of material. Meanwhile, not only the length but also the shape of the pillars changed for PZT-Pt targets. The top of the pillars is quite flat at low E while becoming globular at higher E, as shown in Fig. 4.5 d-f.

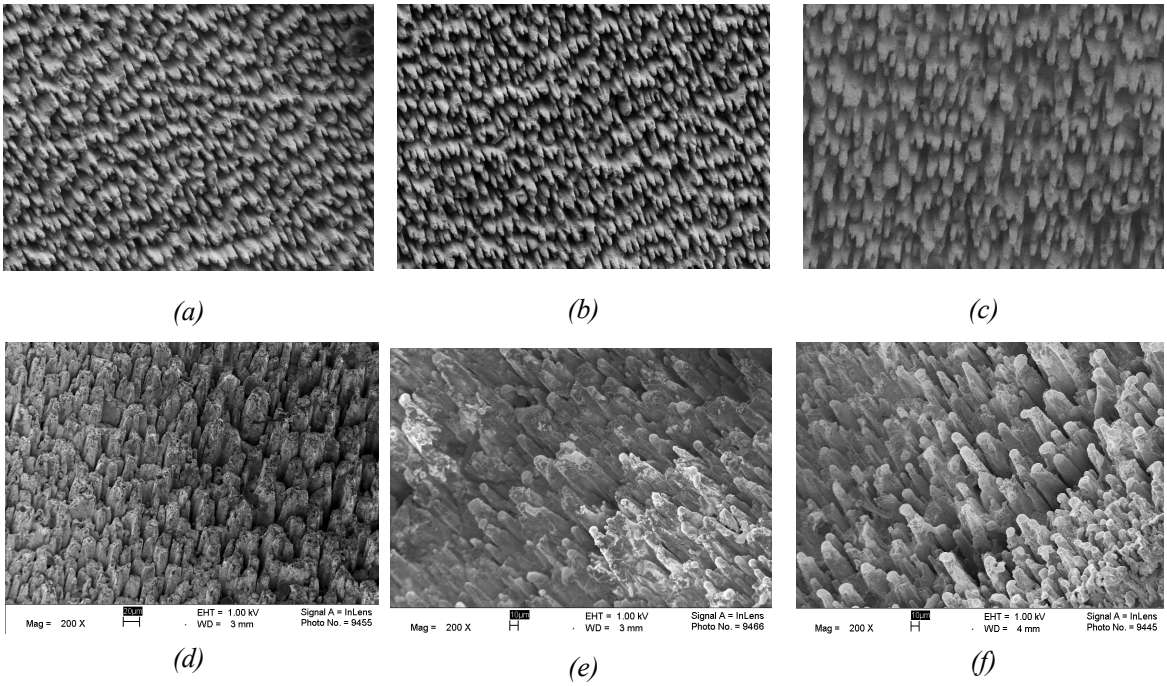

Fig. 4.5. SEM images of the ablated areas for a PZT target after 300 pulses at E = 1.5 J/cm^2 (a), E = 2.5 J/cm^2 (b) and E = 4 J/cm^2 (c); PZT-Pt15 target at E = 1.5 J/cm^2 (d), E = 2.5 J/cm^2 (e) and E = 4 J/cm^2 (f).

In order to evaluate the change in composition of the target upon changing E, we carried out the EDX analysis on those ablated areas. The results are presented in Tables 4.1 and 4.2 for PZT and PZT-Pt15, respectively. Since the surface of the ablated area is very rough, the obtained composition over the average area is not quantitatively precise. It can however give a clear trend for the changes of composition as a function of energy density.

The results clearly present a drop in Pb content after ablation in both targets, which is mainly due to the high volatility of PbO. Pb-deficiency can be seen clearly from analyzing the tip of the pillar. As seen from Table 4.1, the composition of the PZT target does not change with changing E. We can therefore assume that the composition of the PZT film does not depend on E. The energy density influences only the amount and kinetic energy of the ablated species, hence will influence the deposition rate and the film properties, e.g. the film roughness.

For the PZT-Pt15 target the dependence of either Pb, Zr or Ti contents on E was not observed, as shown in Table 4.2. However, a clear trend of decreasing Pt content with increasing E was noticed. This tendency implies that a lower energy density removes less Pt

from the target or, in another word, leaves more Pt in the target. As seen also from Table 4.2, the enrichment of Pt mostly concentrates on the tip of the pillar. The more Pt-enrichment of the target at lower energy densities is consistent with Section 4.3.1.1, which described the instability of the plasma at low E as a result of surface modification of the PZT-Pt target.

Table 4.1. Variation of composition of the PZT target with different laser energy densities.

	at.% Pb	at.% Zr	at.% Ti
Before ablation	80.6	12.9	6.5
Ablated at 1.5 J/cm^2	64.3	26.0	9.7
Ablated at 2.5 J/cm^2	65.1	25.8	9.1
Ablated at 4 J/cm^2	61.9	27.3	10.7
Tip of the pillar (E = 4 J/cm^2)	34.1	50.0	15.9

Table 4.2. Variation of composition of the PZT-Pt15 target with different laser energy densities.

	at.% Pb	at.% Zr	at.% Ti	at.% Pt
Before ablation	4.8	16.0	53.4	25.8
Ablated at 2.5 J/cm^2	4.5	16.2	43.5	35.7
Ablated at 3 J/cm^2	4.8	15.1	44.9	35.2
Ablated at 4 J/cm^2	5.7	17.4	44.2	32.7
Ablated at 5 J/cm^2	5.9	16.8	44.4	32.9
Ablated at 6 J/cm^2	5.7	17.3	45.7	31.3
Tip of the pillar (4 J/cm^2)	3.2	13.3	25.5	57.9

4.3.1.3 Energy density dependence of the Pt content and the morphology of produced PZT-Pt films

From the above analyses we conclude that the laser energy density has a strong impact on the ablation of the target, as illustrated in the surface modification of the target and hence the un-stability of the plasma. As a result, the properties of produced films are expected to be strongly dependent on the energy density.

Firstly, because the laser energy density determines the ablated amount of PZT relative to Pt, it should also influence the composition of the film. XRF analysis was carried out on films deposited from a PZT-Pt10 target at different energy densities. The results are shown in Table 4.3.

Table 4.3. XRF analysis of films deposited from PZT-Pt10 target at different energy densities (T_s = 600 °C, pO_2 = 0.1 mbar, f = 5 Hz).

E (J/cm^2)	1.5	2.5	3.5	4
vol.% Pt	3.6	4.1	4.5	5

As can be seen from Table 4.3, the Pt content increases with increasing E. This observation is in agreement with EDX results obtained on the ablated areas of the PZT-Pt target. A strong dependence of film morphology on E was revealed from the AFM images, presented in Fig. 4.6 for films deposited at E = 1.5, 2.5 and 4 J/cm^2. The film thickness is in the range of 150 to 220 nm. With increasing E the film roughness significantly increases. The film deposited at E = 1.5 J/cm^2 shows the footprint of the terrace structure of $SrTiO_3$ substrate, indicating a very smooth surface (see Fig. 4.6a). For the film deposited at E = 2.5 J/cm^2, grains with an average size of around 70-100 nm are visible in the image (Fig. 4.6b). Columnar growth of the film was revealed from a cross-section SEM image (not presented here). At E = 4 J/cm^2, instead of mono-sized grain morphology, smaller grains appear between large grains. The average grain size also decreases (Fig. 4.6c).

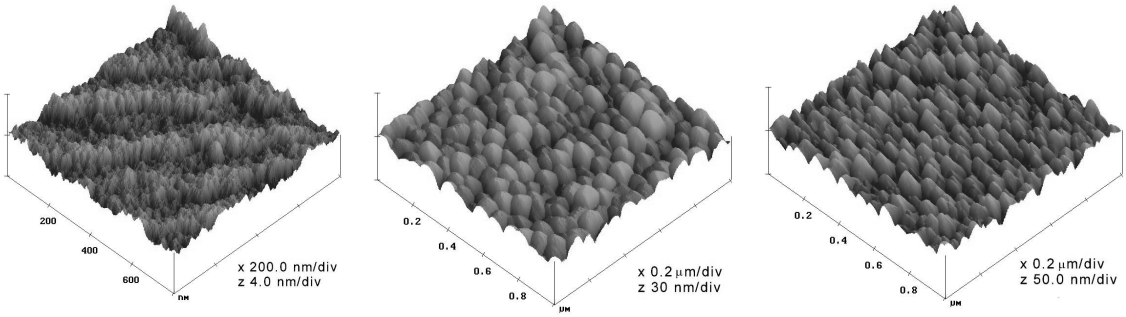

(a) *(b)* *(c)*

rms = 0.6 nm *rms = 2.0 nm* *rms = 5.5 nm*

Fig 4.6. AFM pictures of films deposited at different energy densities using PZT-Pt10 target E = 1.5 J/cm^2 (a), E = 2.5 J/cm^2 (b), E = 4 J/cm^2 (c) (pO_2 = 0.1 mbar, f = 5 Hz). The root mean square (*rms*) of roughness is also indicated.

The roughness of the PZT-Pt film is attributed to the heterogeneous growth of PZT in the presence of Pt. The non-wetting behavior of Pt towards PZT, the difference in the diffusion coefficient and mobility between Pt and PZT enhances the phase segregation and surface

roughening. The surface roughness of the film thus increases with Pt content, which in turn increases with E. The decrease in grain size of PZT-Pt films with increasing E is opposite to that observed for PZT films. It can be explained only by the increase in number of Pt particles located at the grain boundaries of the PZT particles, which prohibits the grain growth of PZT.

The instability of the plasma, as mentioned in Section 4.3.1.1, raises a question about the stability of the deposition rate as a function of E. In Fig. 4.7, the deposition rate is plotted versus the deposition time for E = 1.5 and 4 J/cm^2 using a PZT-Pt10 target. The deposition rate is constant at E = 4 J/cm^2, in consistency with the stable plasma observed. Meanwhile, it drops with time at lower energy density of 1.5 J/cm^2, in agreement with the decrease of plasma size with time.

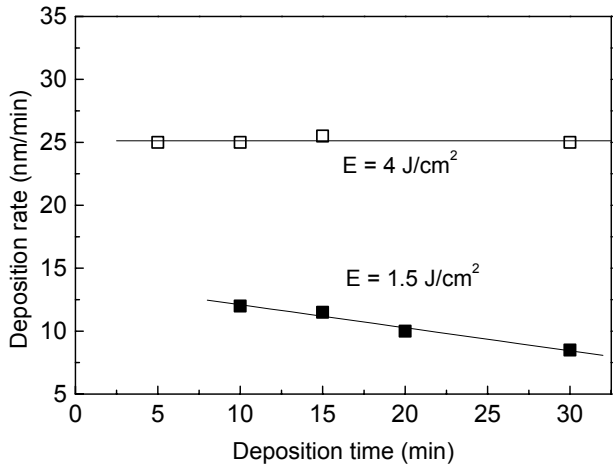

Fig. 4.7. Time-dependence of deposition rate at 1.5 J/cm^2 and 4 J/cm^2 using a PZT-Pt10 target (pO$_2$ = 0.1 mbar, f = 5 Hz, d = 45 mm). The lines are for eyes guiding.

Furthermore, due to the change of the target composition as a function of time, one can expect a gradient of the Pt content for films fabricated at low energy density. Two films deposited from a PZT-Pt15 target at E = 1.5 J/cm^2 and E = 4 J/cm^2 were analysed by XPS sputter profiling to get the depth profile of the Pt concentration. The obtained results are shown in Fig. 4.8. As seen from this figure, the film deposited at 1.5 J/cm^2 demonstrates a gradual decrease of the Pt content from the film surface to the film-substrate interface. This observation can be interpreted as an increase in Pt content with increasing deposition time. It is understandable from the Pt enrichment of the target under a low laser energy density, as discussed above. In contrast, the film deposited at 4 J/cm^2 shows a rather steady

Pt content along the film thickness. The Pt content indeed decreases slightly from 8 at.% to 7.5 at.% near the expected interface. However, at the interface the Pt content does not drop to zero but shows a tail with a noticeable amount of Pt at a distance of 20 nm away from the interface into the substrate. The tail is probably due to the rough surface after sputtering profiling (rms ~ 2.5 nm as taken from AFM picture) or due to diffusion of Pt in to the substrate [21]. However, the latter assumption is unlikely since at 600 °C a metal is not expected to diffuse into an oxide single-crystal substrate with such a deep penetration.

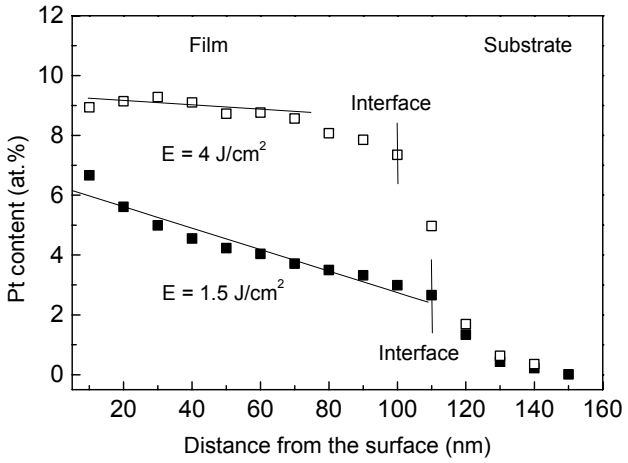

Fig. 4.8. Depth profile of Pt concentration in films deposited from a PZT/Pt10 target at 1.5 and 4 J/cm^2 (pO_2 = 0.1 mbar, f = 5 Hz, d = 45 mm). The lines are just for eye-guiding.

In conclusion, extremely smooth films are obtained at a low laser energy density. The film however has a gradient of Pt content along the film thickness and a lower Pt content compared to the target. Furthermore, the deposition rate decreases with ablation time. A higher Pt content film is obtained only by a long pre-ablation and at the expense of very low deposition rate. Rougher films are grown at high laser energy density. However, a closer stoichiometric transfer from the target to the film and a stable film deposition is realised. The effect of the energy density on the electrical properties will be investigated later in Chapter 5.

4.3.2 Material transport towards the substrate

4.3.2.1 Influence of the gas pressure

When an ambient gas is present in the deposition chamber, it scatters, attenuates, and thermalises the plasma species, changing the deposition rate, the spatial distribution and

the kinetic energy distribution of the species. A reactive gas such as oxygen or nitrogen results in the formation of chemical compounds like oxides or nitrides, correspondingly. For deposition of PZT an oxygen environment is required to ensure the oxygen stoichiometry and also to minimize the loss of PbO. In Refs. [22, 23], the authors observed a strong increase of at least 4 times in the Pb content of films deposited in an oxygen environment as compared to films deposited in vacuum. The effect was attributed to a reduction of the re-sputtering arising from scattering of ablated species by ambient gas molecules.

In our experiments, a perovskite PZT phase was not obtained in oxygen pressures lower than 0.05 mbar. Failure to form a perovskite phase is usually due to severe Pb-deficiency. The following equilibrium of PbO with oxygen may play an important role in determining the Pb content in the film:

$$PbO_{solid} \rightleftharpoons PbO_{vapor} \rightleftharpoons Pb_{vapor} + \tfrac{1}{2}\, O_2(g) \qquad (4.1)$$

A deficiency of O_2 shifts the equilibrium to the right, where PbO in the film is decomposed to O_2 and Pb in vapor.

In order to investigate the influence of oxygen pressure on thin film deposition, a PZT-Pt25 target was used for ablation at $E = 4$ J/cm^2, $f = 1$ Hz and at different oxygen pressures $pO_2 = 0.05$, 0.2 and 0.4 mbar. The produced plasmas were pictured by a digital camera and are shown in Fig. 4.9. As can be seen from these pictures, the shape of the plasma strongly depends on the oxygen pressure. At low pressure of 0.05 mbar, the plasma is round and relatively large. At $pO_2 = 0.2$ mbar, it becomes narrower and smaller with sharp boundaries. At higher pressure of 0.4 mbar, the plasma changed in shape while remaining the same size. The sharpening of the plasma boundary is an indication of a shock front, resulting in a spatial confinement of the plasma [24].

The deposition rate was found to increase with increasing oxygen pressure, from 15 nm/min at 0.05 mbar to 17 nm/min at 0.2 mbar and 23 nm/min at 0.4 mbar. It is expected that the amount of removed material is mainly determined by the laser energy density and is little affected by the oxygen pressure. The above difference in deposition rate is simply due to the spatial redistribution of species inside the plasma [20]. In high vacuum, due to the lack of interaction between ablated species and gas molecules, the ablated species are free to expand over the whole space. It results in large but diluted plasma. In the presence of gas molecules, the species are confined to the center of the plasma. As a con-

sequence, the plasma is smaller and more concentrated. As the substrate is placed in the plasma center, the deposition rate of material on the substrate will be higher at high than at low pressures. Furthermore, the role of the sticking coefficient, which determines the number of re-evaporated atoms from the film surface, also should be considered. As mentioned in Ref. [22], the sticking coefficient increases with increasing oxygen pressure, possibly because the incorporation of oxygen into ablated species enhances the sticking probability.

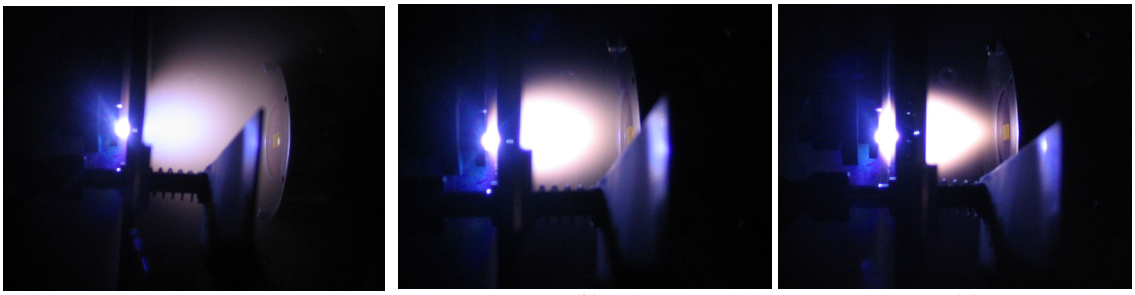

(a) *(b)* *(c)*

Fig 4.9. Plasmas produced from a PZT-Pt25 target at pO_2 = 0.05 mbar (a), pO_2 = 0.2 mbar (b), pO_2 = 0.4 mbar (c).

Beside the spatial redistribution, the change in kinetic energy of ablated species is another effect resulting from changing oxygen pressure. It leads to a change in film morphology as can be seen from cross-section SEM images presented in Fig. 4.10.

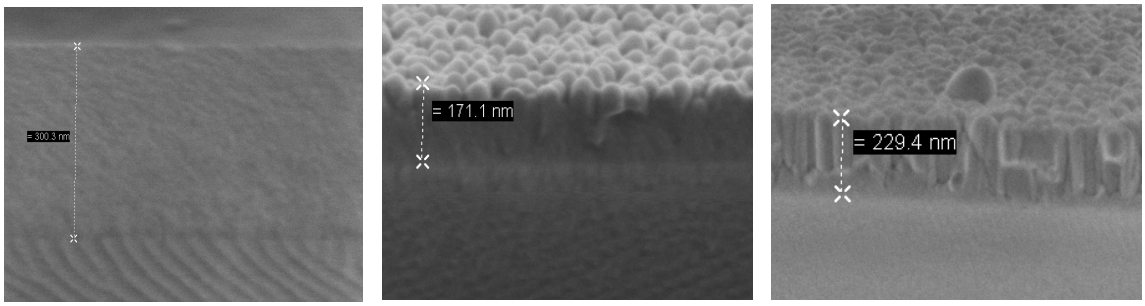

(a) *(b)* *(c)*

Fig. 4.10. Cross-section SEM images of PZT-Pt25 films on STO substrates, deposited at different oxygen partial pressures 0.05 mbar (a), 0.1 mbar (b), 0.4 mbar (c) (E = 4 J/cm^2, f = 3 Hz, d = 45 nm).

The film deposited at pO_2 = 0.05 mbar is very smooth even at a thickness of around 300 nm. With further increasing pressure, films become rougher with larger lateral particle sizes and a more well-defined columnar structure. These different behaviors in film growth are considered due to the different diffusitivity of the adatoms, which ultimately relate to

their mobility and kinetic energy. For example, the more oxidized species at high oxygen pressures have lower mobility than the less oxidized ones at low oxygen pressures, hence forming a rougher film surface. It is well known about the two pressure regimes in PLD, described by the drag model for lower pressures and by the shock wave model for higher pressures. At the transition pressure for shock wave formation, a sharp decrease in the kinetic energy of species is induced [24]. If we assume that a lower kinetic energy of the adatoms leads to a rougher film surface, the above abrupt increase in film roughness at 0.1 mbar probably coincides with the transformation to the shock wave regime.

4.3.2.2 Influence of the target-to-substrate distance

During transport from target to substrate, the ablated species loose their kinetic energies due to interaction with each other and/or with ambient gas molecules. The kinetic energy of the ablated species is therefore a function of the traveling distance. A set of films were deposited from a PZT-Pt25 target on $SrTiO_3$ substrates using E = 4 J/cm^2, pO_2 = 0.1 mbar, f = 10 Hz and at the following target-to-substrate distances:

- d = 35 mm: the substrate was located inside the plasma and 10 mm away from the visible plasma.

- d = 45 mm: the substrate was located just at the end of the visible plasma.

- d = 55 mm: the substrate was located outside the plasma and 10 mm away from the end of the plasma.

- d = 65 mm: the substrate was located outside the plasma and 20 mm away from the end of the plasma.

In Fig 4.11, the cross-section SEM images of films deposited at d = 45 mm and d = 65 mm are presented as representative samples. No difference in morphology and roughness was observed for the films even-though it is known that the kinetic energy can influence the film roughness through the diffusion of adatoms along the surface. However, it should be emphasized that there are at least two factors governing the growth of a heterogeneous film: the surface diffusion of adatoms (for all kinds of film growth) and the surface interaction between two phases (only for a hetero-growth). Due to the latter effect, the formation of grain boundaries and surface roughening is much enhanced in the presence of a second phase. In our case the hetero-growth seems to play a dominant role over the surface diffusion. Since changing the target-substrate distance alters only the kinetic energy of the ar-

riving species but not the Pt fraction, it should not cause a large difference in film morphology.

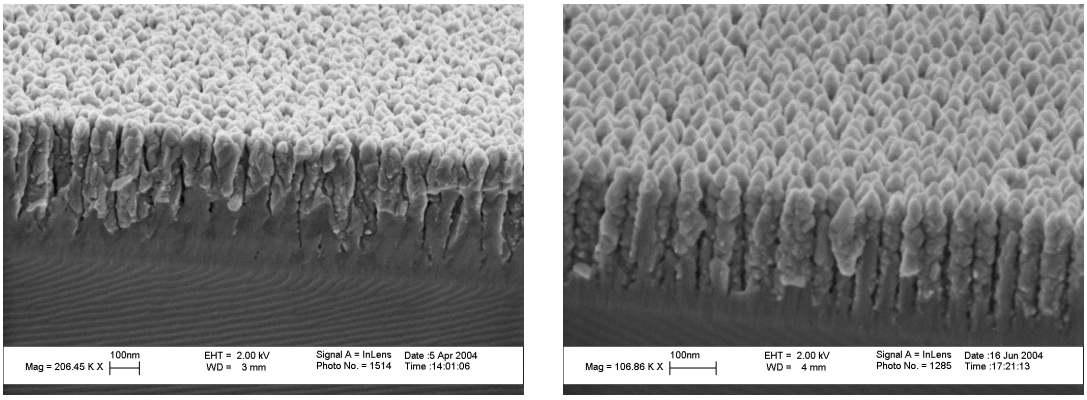

(a) *(b)*

Fig. 4.11. Cross-section SEM images of films deposited from a PZT-Pt25 target at the target-substrate distances of 45 mm (a) and 65 mm (b) (E = 4 J/cm^2, f = 10 Hz, pO_2 = 0.1 mbar).

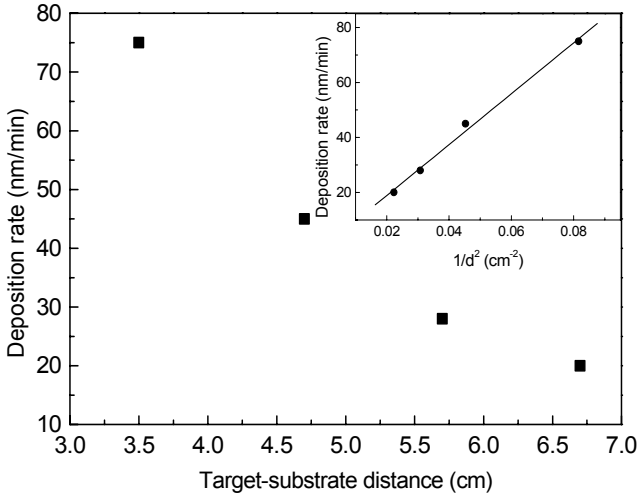

Fig. 4.12. The deposition rate versus target-substrate distance for ablation of a PZT-Pt25 target (E = 4 Jcm^2, f = 10Hz, pO_2 = 0.1 mbar). The inset presents the deposition rate versus inverse square distance, where the solid line is a linear fitting.

We observed a major effect of increasing target-substrate distance on decreasing the deposition rate. The deposition rate decreases from 75 nm/min at d = 35 mm to 20 nm/min at d = 65 mm. The dependence of deposition rate on target-substrate distance is illustrated in Fig. 4.12. This is found in accordance with the inverse distance squared relation for vacuum [20]:

$$R(d) = \frac{R_{d=0}}{d^2} \tag{4.2}$$

where $R_{d=0}$ and $R(d)$ correspond to the deposition rate at the target surface (zero distance) and at distance d, respectively. The plot of the deposition rate versus $1/d^2$ shows a linear dependence as presented as an inset of Fig. 4.12. The inverse distance squared relation for vacuum holds also for oxygen background implying that the gas pressure affects the angular distribution of the ablation plume, and does not merely alter the laser energy density.

4.3.3 Deposition and growth of material on the substrate

4.3.3.1 Influence of the substrate temperature (deposition temperature)

In this section we focus on the influence of the substrate temperature on film growth, since by using an appropriate temperature a fully developed perovskite PZT can be produced directly on $SrTiO_3$ substrates. Films were grown at temperatures from 400 °C to 700 °C. As-deposited PZT-Pt films are light brown in comparison with yellowish transparent pure PZT. Deposition at higher substrate temperature leads to darker colored films, which is tentatively explained by the increase of the Pt particle size. XRD patterns of PZT-Pt films deposited at different substrate temperatures using a PZT-Pt10 target are presented in Fig. 4.13.

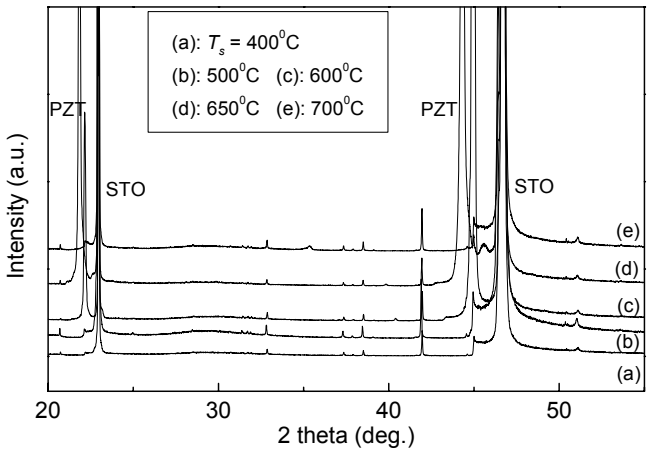

Fig 4.13. XRD patterns of films deposited from a PZT-Pt10 target at different substrate temperatures (E = 2.5 J/cm^2, f = 5 Hz, pO_2 = 0.1mbar).

The degree of crystallization of PZT phase evidently depends on the substrate temperature. Below 600 °C, no evidence is found for the formation of the perovskite PZT phase. This suggests that PZT exists either in the amorphous or in the nanocrystalline (pyro-

chlore) states. Only films deposited at $T_s \geq 600$ °C show the appearance of the perovskite phase, which grows preferentially along the (100) direction. Films deposited at 700 °C show only very weak PZT reflections. This may be explained by the strong re-evaporation of PbO at high temperature, leading to decomposition of the PZT phase.

Besides peaks from the $SrTiO_3$ substrate, only peaks originating from PZT are observed. The absence of Pt peaks in the diagrams is due to the small crystallite size of a few nm (see Section 4.3.4 and Chapter 5) as well as by the overlap between Pt and $SrTiO_3$ peaks.

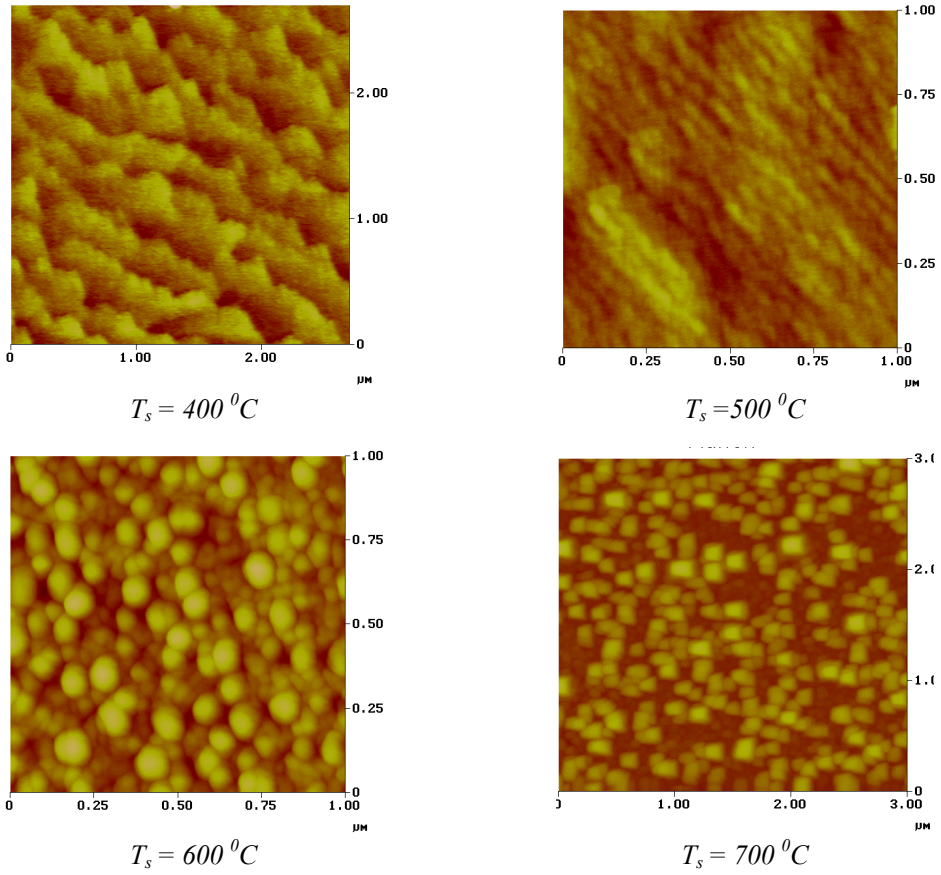

Fig. 4.14. AFM pictures of films deposited from a PZT-Pt10 target at different temperatures (E = 2.5 J/cm^2, f = 5 Hz, pO_2 = 0.1 mbar). The substrate temperature is indicated below each image.

More details about the effect of the substrate temperature on the film microstructure are provided in the AFM pictures given in Fig. 4.14. The change in film morphology appears to coincide with the structural phase transition of PZT. At T_s = 400 °C the film was extremely smooth with no grain structure (amorphous state). It changed to an oriented fine-

grained structure (nano-crystalline pyrochlore) at T_s = 500 °C and later to a globular grain structure (perovskite) with grain sizes of 60-80 nm at T_s = 600 °C. At the higher T_s of 700 °C, instead of a smooth surface with mono-sized grains, the films exhibit islands dispersed in a smooth matrix.

4.3.3.2 Influence of the laser frequency

Differently from other vacuum techniques, in PLD a high instantaneous vapor flux resulting from each pulse is followed by periods of no vapor flux between pulses. One can easily change the time interval between laser pulses by changing the laser frequency. The film nucleation density is proportional to F/D, where F is the vapor flux per pulse and D is the diffusivity. However, the film nucleation and growth also depend on how the period of pulses is relative to the time constant for the diffusion, agglomeration and dissociation. If those parameters are comparable the laser frequency may have a large influence on film growth, otherwise the effect can be neglected.

To study the influence of the laser frequency we varied the frequency from 1 Hz to 10 Hz. The SEM cross-section images of two representative films deposited from PZT-Pt25 target at f = 1 Hz and 10 Hz are shown in Fig. 4.15.

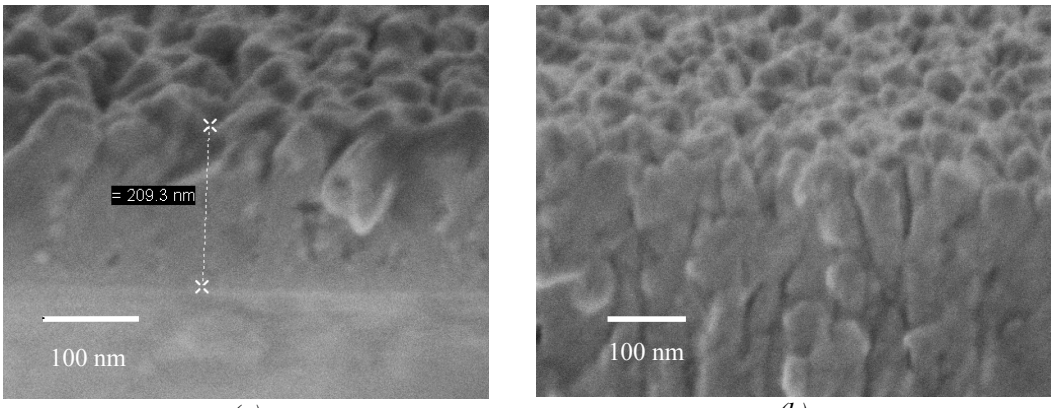

(a) *(b)*

Fig 4.15. PZT-Pt25 films deposited at f = 1 Hz (a) and f = 10 Hz (b) (E = 4 J/cm^2, pO_2 = 0.1 mbar, d = 45 mm).

The films have a columnar structure with the same surface roughness, which indicates the insignificant effect of the laser frequency on film morphology. Possibly, the time between pulses is either much longer or shorter than the agglomeration and/or the dissociation rates and thus has no influence on film growth. It also might be that the interfacial energies of Pt and PZT are the most governing parameters in film nucleation and growth, as we discussed

in Section 4.3.2.2 about the influence of the target-substrate distance. The frequency can be exploited mainly in controlling the deposition rate. For PZT-Pt25 target, the deposition rate can be increased from 6 nm/min at f = 1 Hz to 45 nm/min at f = 10 Hz. Further more, using a high frequency has an advantage of decreasing the deposition time and minimizing PbO loss, especially at high deposition temperatures.

4.3.4 Post-annealing

The crystallinity of film can be developed by either increasing the substrate temperature or by post-annealing of as-deposited films. For example, PZT/Pt films deposited at T_s = 400 °C are completely amorphous. They can be transformed to the perovskite phase upon annealing at higher temperatures. This amorphous-perovskite phase transformation usually takes place at around 600 °C. For films grown on $SrTiO_3$ substrates, as-deposited at high T_s and post-annealed films posses the same crystallographic structure, with a preferred orientation in the (001) direction.

Films can be either in-situ annealed in the deposition chamber right after the deposition or ex-situ annealed. Ex-situ annealing was carried out in a closed crucible with PbO controlled atmosphere to prevent PbO evaporation at high temperatures. As a result, ex-situ annealed films have the advantage over in-situ annealed films of less Pb-deficiency. This observation recommends that if a PbO atmosphere can be created inside the deposition chamber during in-situ annealing, good quality of films will be produced.

Films annealed at 600 °C for 30 minutes mainly consist of the perovskite phase. A small amount of pyrochlore, however, still remains and deteriorates the electrical properties of the films. For an annealing temperature of 650 °C, the pyrochlore phase fully transforms to perovskite. Unfortunately, films with Pt contents higher than 15 vol.% became conductive after annealing. It indicates the formation of Pt conducting channels in the film around 650 °C. Since the percolation threshold is predicted to be around 50 vol.% for thin films [25], the conducting channel is either formed along the thickness or at the surface through diffusion of Pt. A cross-section SEM image of a film, as-deposited at 400 °C using a PZT-Pt15 target and further annealed at 650 °C, is presented in Fig. 4.16. In this image the PZT phase appears as a dark matrix. The Pt phase appears as bright round particles, which are dispersed all over the film thickness. From the cross-section image, it is difficult to draw a conclusion whether Pt conducting channels form at the surface or along the film

thickness. Based on the columnar structure of the film we suggest that the later case is more likely.

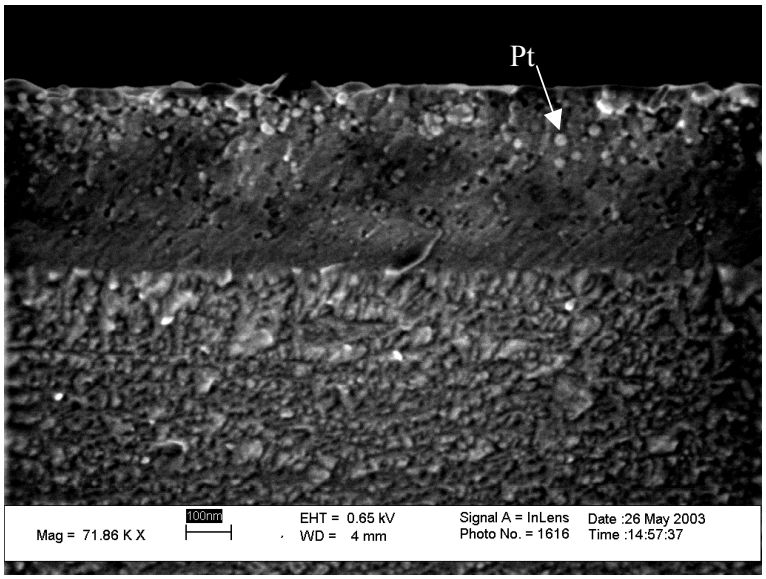

Fig. 4.16. Cross-section SEM image of film deposited from a PZT-Pt15 target (E = 4 J/cm^2, f = 5 Hz, t = 15 min, pO$_2$ = 0.1mbar, T_s = 400 °C) followed by annealing at 650 °C for 30 minutes.

4.4 Conclusions

PLD involves many complex processes where various parameters can influence the film deposition. We found that the most critical parameter for depositing a composite film from a composite PZT-Pt target is the laser energy density. By using a low energy density of 1.5 J/cm^2, a very smooth film can be obtained. However it also leads to a much lower Pt content in the film as compared to the Pt content in the target. This difference resulted from the quite different ablation behaviour of PZT from Pt. The plasma is unstable during deposition, which follows from the fact that the target composition is modified during the laser ablation process. By using energy densities above the ablation threshold of Pt (4 J/cm^2), one can prevent the above phenomenon and ensure a stable deposition rate with time and a homogeneous profile of Pt content along the film thickness.

Perovskite PZT phase is obtained only at high oxygen pressures (pO$_2$ ≥ 0.05 mbar) since at lower pressure PbO is substantially lost in the form of Pb metal and oxygen. Increasing the

oxygen pressure further results in the confinement of the plasma and hence in an increase of the deposition rate. The film roughness increases with increasing oxygen pressure.

An important parameter for the crystallographic properties of the film is the substrate temperature. Perovskite PZT phase can be directly obtained on $SrTiO_3$ substrates at a narrow range of deposition temperature between 600 and 650 °C. Lower temperatures produce an amorphous phase or a disordered pyrochlore phase while higher temperatures lead to a Pb-deficient pyrochlore phase. Eventhough post-annealing can provide the same effect as an increased substrate temperature, it is not recommended for PZT-Pt films with Pt content higher than 15 vol.%. The reason is that during annealing Pt particles with high mobility seem to aggregate at grain boundaries of the columnar PZT phase and thus short-circuit the film.

The influence of the laser frequency and the target-to-substrate distance on the growth of PZT-Pt film is not of significance for the hetero-growth of PZT in the presence of Pt. The film roughness is mainly determined by the Pt content in the film. The laser frequency and the target-to-substrate distance can be exploited in tuning the film deposition rate.

From the above analyses, one can choose the most suitable parameters to obtain the desired properties of PZT/Pt films. The parameters listed in Table 4.4 have been selected by us to fabricate the films for further electrical characterisations, which will be presented in Chapter 5.

Table 4.4. The PLD conditions for fabrication of PZT-Pt composite films.

Parameter	Setting	
Laser energy density	4 J/cm^2	(for close Pt content between film and target)
	1.5 J/cm^2	(for extremely smooth film)
Oxygen pressure	0.1 mbar	
Substrate temperature	600 °C	
Laser frequency	10 Hz	
Target-to-substrate distance	45 mm	

References

1. C. Brosseau, A. Beroual and A. Boudida, *How do Shape Anisotropy and Spatial Orientation of the Constituents Affect the Permittivity of Dielectric Heterostructure?*, J. Appl. Phys. **88** (2000) 7278.
2. A. Malliaris and D.T. Turner, *Influence of Particle Size on the Electrical Resistivity of Compacted Mixtures of Polymeric and Metallic Powders*, J. Appl. Phys. **42** (1971) 614.
3. X.H. Wang, J. Shi, S. Dai and Y. Yang, *A sol-gel method to prepare pure and gold colloid doped ZnO films*, Thin Solid Films **429** (2003) 102.
4. T.K. Kundu and D. Chakravorty, *Nanocomposites of lead-zicronate-titanate glass ceramic and metallic silver*, Appl. Phys. Lett. **67** (1995) 2732.
5. L. Tang, P. Du, G. Han, W. Weng and G. Zhao, *Preparation of silver dispersed $PbTiO_3$ film by sol-gel method*, Materials Science and Engineering B **99** (2003) 370.
6. Y. Matsuoka, E. Ban and T. Yoshimura, *Superconducting YBCO/Ag composite films prepared by spraying a suspension*, Thin Solid Films **385** (2002) 1.
7. H.Y. Ko, M. Mizuhata, A. Kajinami and S. Deki, *Fabrication and characterization of Pt nanoparticles dispersed in Nb_2O_5 composite films by liquid phase deposition*, J. Mater. Chem **12** (2002) 1495.
8. M. Ando, R. Chabicovsky and M. Haruta, *Optical hydrogen sensitivity of noble metal-tungsten oxide composite films prepared by sputtering deposition*, Sensors and Actuators B **76** (2001) 13.
9. J.G. Serrano and U. Pal, *Synthesis and characterization of Au nanoparticles in Al_2O_3 matrix*, International Journal of Hydrogen Energy **28** (2003) 637.
10. J. Hsu, S. Chen and C. Chang, *Anomalous positive magnetoresistance in Fe_3O_4-Ag composite films*, Journal of Magnetism and Magnetic Mateirals **242-245** (2002) 479.
11. B. Bian, Y. Hirotsu and A. Makino, *Microstructure and magnetic property of Fe-Al_2O_3 granular films*, Nanostructured Materials **8** (1997) 1057.
12. C.N. Afonso, R. Serna, J.M. Ballesteros, A.K. Petford-Long and R.C. Doole, *Synthesis by pulsed laser deposition of metallic nanoclusters embedded in an amorphous host*, Applied Surface Science **127-129** (1998) 339.
13. J. Gonzalo, R. Serna and C.N. Afonso, *Quantative optical determination of shape of Cu nanocrystals in a composite film*, J. Appl. Phys. **89** (2001) 5734.
14. T. Takeshi, K.M. Beck and N. Koshizakai, *Preparation of Pt/TiO_2 nanocomposite films by 2-beam pulsed laser deposition*, Applied Surface Science **197-198** (2002) 619.

15. D. Kumar, J. Narayan, T.K. Nath, A.K. Sharma, A. Kvit and C. Jin, *Tunable magnetic properties of metal ceramic composite thin films*, Solid State Communications **119** (2001) 63.

16. H. Wang, Y. Zhu and P.P. Ong, *Surface modification of CdS nanocrsytallites doped in SiO_2 matrix*, J. Appl. Phys. **90** (2001) 964.

17. Z. Liu, X.K. Meng, X.L. Guo, X. Liu, J.M. Liu and J.M. Hong, *The structure of Pt-Al_2O_3 composite films prepared by pulsed laser deposition technique*, Thin Solid Films **286** (1996) 49.

18. Lianne Doeswijk, *Pulsed Laser Deposition of Oxides on Silicon: Exploring Their Passivating Qualities*, PhD thesis, University of Twente, The Netherlands, 2002.

19. D.B. Chrisey and G.K. Hubler, *Pulsed Laser Deposition of Thin Films*, John Wiley & Sons Inc., New York, 1994.

20. O. Auciello, R. Dat and R. Ramesh, *Pulsed Laser Ablation synthesis and characterisation of ferroelectric thin films and heterostructures* in Ferroelectric thin films: synthesis and basic properties, Eds. C.P. Araujo, J.F. Scott and G.W. Taylor, Gordon and Breach Publishers, 1996.

21. D. Leinen, R. Sireira, E. Rodriguez-Castellon, M.L. Calzada, *XPS depth profile analysis of sol-gel calcium-modified lead titanate thin films*, Thin Solid Films **354** (1999) 66.

22. C.S. Ma, S.K. Hau, K.H. Wong, P.W. Chan and C.L. Choy, *The role of ambient gas scattering effect and lead oxide formation in pulsed laser deposition of lead-zirconate-titanate thin films*, Appl. Phys. Lett. **69** (1996) 2030.

23. M. Tyunina, J. Levoska and S. Leppavouri, *Experimental studies and modeling of Pb-Zr-Ti-O film growth in pulsed laser deposition*, J. Appl. Phys. **83** (1998) 5489.

24. D.B. Geohegan, *Fast intensified-CCD photography of $YBa_2Cu_3O_{7-x}$ laser ablation in vacuum and ambient oxygen*, Appl. Phys. Lett. **60** (1992) 2732.

25. M. Sahimi, *Application of percolation theory*, Taylor and Francis Ltd., 1994.

5

Microstructure and electrical properties of PZT-Pt thin films

5.1 Introduction

In Chapter 3 we presented a study on the properties of the bulk PZT-Pt composites. The enhancement of the dielectric constant in the material is explained by either the effective medium theory or the percolation theory. The modification of the ferroelectric properties in the presence of Pt phase is attributed to two factors: the space charge polarisation at the PZT/Pt interfaces and the diluting effect of Pt. As mentioned, the electrical properties of a metal-insulator system depend on the volume fraction [1, 2], the distribution [3] and the particle size [4] of a metal phase. Thin film fabrication of PZT-Pt composites by Pulsed Laser Deposition (PLD) and the influence of deposition conditions on film growth were discussed in Chapter 4. In this chapter we will study the microstructure and the dielectric and ferroelectric properties of PLD-produced PZT-Pt thin films. Attention will be paid to the influence of the Pt phase. The relationship between the microstructure and the electrical properties of the film will be discussed also. These properties will be compared with those obtained for bulk material.

5.2 Experimental

Composite PZT-Pt targets, containing Pt particles of a few μm in size, were prepared by a sol-precipitation route (see Chapter 3). The Pt content was varied from 3 to 25 vol.%. A KrF excimer laser (λ = 248 nm, f = 10 Hz) was used to grow PZT-Pt films in an oxygen environment (pO_2 = 0.1 mbar) on (001) $SrTiO_3$ substrates. In order to have atomically flat surfaces, the substrates were chemically and thermally treated prior to deposition. In this way a TiO_2-terminated surface layer was produced [5]. During deposition, the substrate temperature was kept at 600 °C to promote the crystallization of the PZT phase. The energy density *(E)* of the laser spot was either 4 J/cm^2 or 1.5 J/cm^2.

The produced thin films were characterized by XRD, AFM and TEM. Their composition was determined by X-ray fluorescence (XRF). Samples for the electrical characterization

were prepared on single crystal 1 wt.% Nb-doped $SrTiO_3$ substrates. The electronically conducting substrate acted as bottom electrode. The top electrode was provided by sputter deposition of gold in a surface area of 100×100 μm using a shadow mask. The film thickness was determined from a cross section SEM image. The low-field dielectric constant and dielectric loss were measured at room temperature by means of a multi-frequency LCR meter 4141pA with a driving voltage of 50 mV in a frequency range of 100 Hz - 1 MHz. The high temperature *C-V* measurements were performed at temperature range of 40 °C to 250 °C, at 10 kHz and with a 50 mV amplitude ac signal using a 4275A Multi-frequency LCR meter (Hewlett-Packard). The high temperature dielectric constants were calculated from low-field capacitances. The *I-V* characteristics were recorded at room temperature using a 4140B pA meter/d.c voltage source. Prior to the *I-V* measurements the samples were pre-poled. The polarity of the applied voltage was considered with respect of the top electrode, while the bottom electrode was grounded. The *P-E* loop measurements were carried out using a Sawyer-Tower circuit over a frequency range of 100 Hz - 1 kHz.

5.3 Results and discussion

5.3.1 Influence of the Pt content

PZT-Pt films were deposited at $E = 4$ J/cm^2 for 15 min. The corresponding thickness of deposited films, as determined from cross section SEM, was in the range of 500 to 800 nm, depending on the Pt content.

5.3.1.1 Microstructural properties

In Fig. 5.1 the XRD diagrams of PZT-Pt films with various Pt contents are presented [i]. All films show perovskite reflections of PZT with a (001) preferred orientation. The presence of amorphous or pyrochlore phases could not be detected from the diffraction patterns.

In the XRD diagrams, the Pt reflections could not be identified, either because these overlap with the $SrTiO_3$ peaks or because of the nanometer size of the Pt particles. The presence of a Pt phase has been proven quantitatively by the XRF analysis (see Chapter 4) and

[i] Films with different Pt contents are denoted similar to the corresponding target, i.e., the film deposited from a PZT-Pt5 target is denoted as PZT-Pt5 film.

also by TEM imaging, as shown in Fig. 5.2a. The TEM picture clearly shows that Pt particles, visible as dark spots in a brighter PZT matrix phase, are dispersed homogeneously. Pt particle sizes are in the range of 3-10 nm. The PZT phase shows a columnar structure with an average width of 60-80 nm. The cross-section TEM image in Fig. 5.2b shows a good matching of lattice fringes between the film and the $SrTiO_3$ substrate, especially at the film-substrate interface.

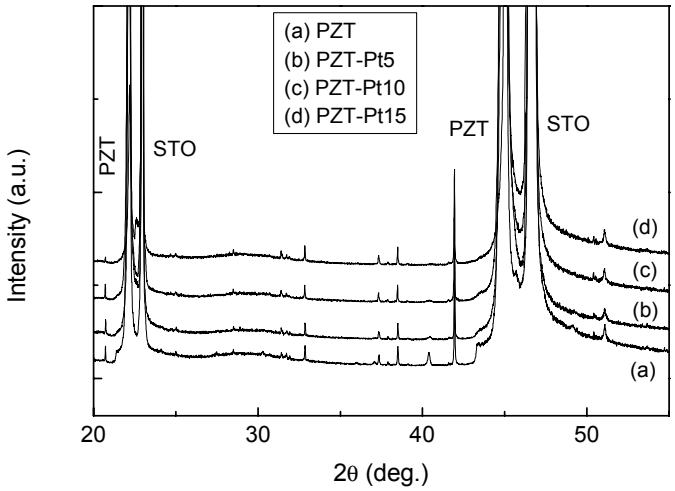

Fig 5.1. XRD patterns of PZT-Pt films with different Pt contents. The result of PZT film is also shown for comparison.

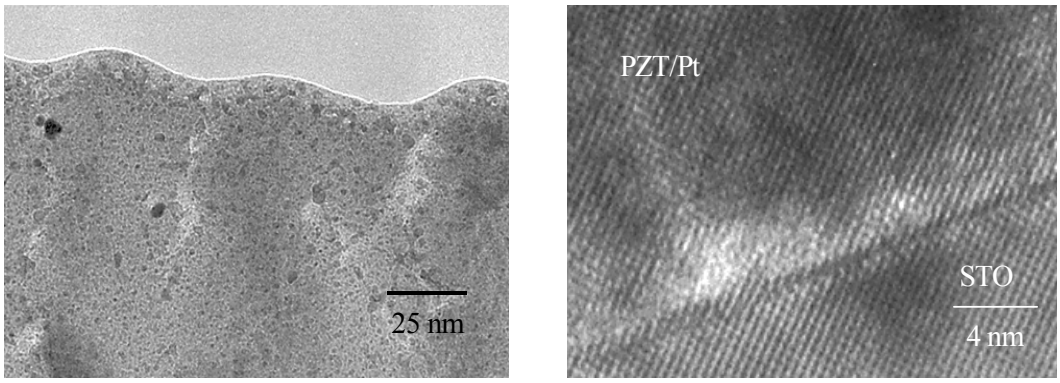

Fig. 5.2. Cross-section TEM image of a PZT-Pt10 film as general view (a) and at the film/electrode interface (b).

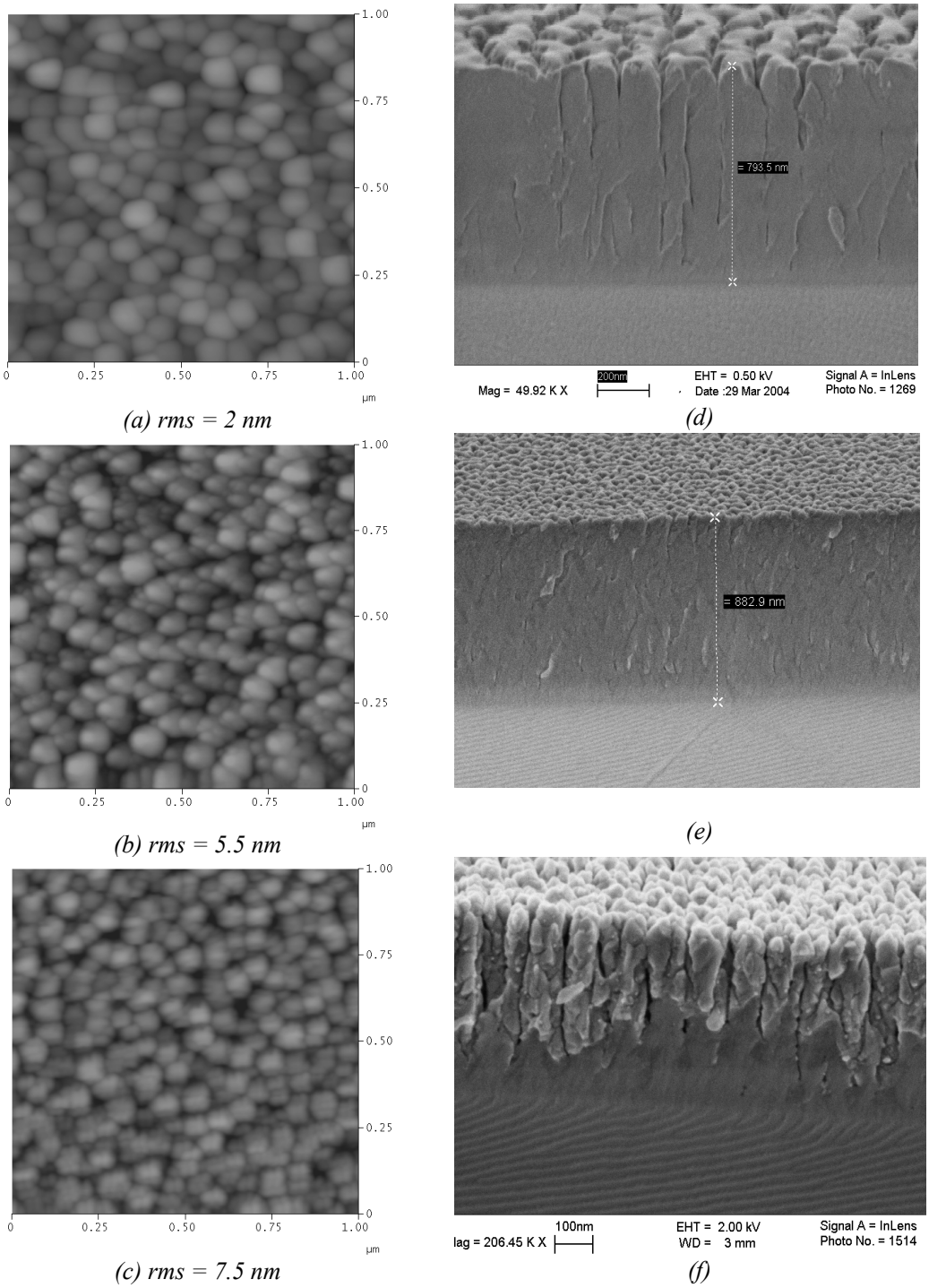

Fig. 5.3. AFM images of PZT-Pt5 (a), PZT-Pt10 (b) and PZT-Pt15 films (c) (the roughness (rms) is indicated); SEM pictures of corresponding films (d-e).

The surface properties of PZT-Pt films are revealed in the AFM pictures given in Fig. 5.3a-c. It can be seen that the roughness of the film increases with increasing Pt content. The average lateral size of PZT is around 70 nm, which is in agreement with the TEM

observations. In high Pt content films (Fig. 5.3b-c), small particles of 30-40 nm appear in between large grains. It is assumed that Pt inclusions at the PZT grain junctions inhibit the growth of the PZT grains, as was also observed for bulk materials. Corresponding cross-section SEM images of those samples are provided in Fig. 5.3d-e. All films show a columnar structure. With increasing Pt content, the columns become more irregular with open grain boundaries and small particles surrounding them.

5.3.1.2 Electrical properties

a. Dielectric constant and dielectric loss

The dielectric constant ε and dielectric loss *tan* δ are presented as a function of frequency *f* in Fig. 5.4 for PZT and PZT-Pt films with Pt contents below 10 vol. %. As can be seen from Fig. 5.4a, those films exhibit an almost linear dependence of ε on frequency. In the wide range from 500 Hz to 1 MHz, *tan* δ has low and almost unvaried values around 0.04, except the slight increase around 1 MHz (Fig. 5.4b). At low frequency of 100 Hz, it increases sharply above 0.1. Of notation is the increase of ε with increasing Pt content while *tan* δ remains low.

The frequency dependence of both ε and *tan* δ changes abruptly at Pt content of 15 vol.% (see Fig. 5.5a). The dielectric constant exhibits a sharp increase at $f \sim 1$ kHz, accompanied by a peak of *tan* δ around that frequency. The maximum value of *tan* δ increases significantly to 0.4. The same behaviour was observed for PZT-Pt25 film, but with the loss peak shifting to 300 Hz and a maximum loss of 0.79 (Fig. 5.5b).

The dependence of dielectric constant on Pt content, measured at 100 Hz and 1 kHz, is presented in Fig. 5.6, together with results obtained on bulk PZT-Pt. For PZT-Pt films, increasing the Pt content up to 10 vol.% results in an increase of ε. The enhancement factor is maximum at 10 vol.% Pt and equals 8 with respect to pure PZT, which is much higher than that obtained in the bulk. With further increase of Pt content the dielectric constant starts to decrease. The difference between ε values measured at 100 Hz and 10 kHz is more significant at these Pt contents.

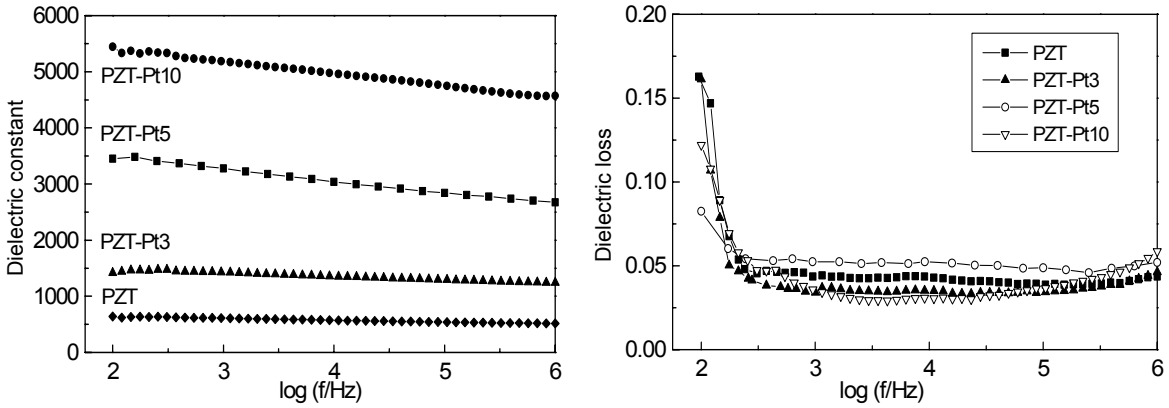

Fig. 5.4. Frequency dependence of the dielectric constant (a) and the dielectric loss (b) of PZT-Pt films with Pt contents varying from 0 to 10 vol.%.

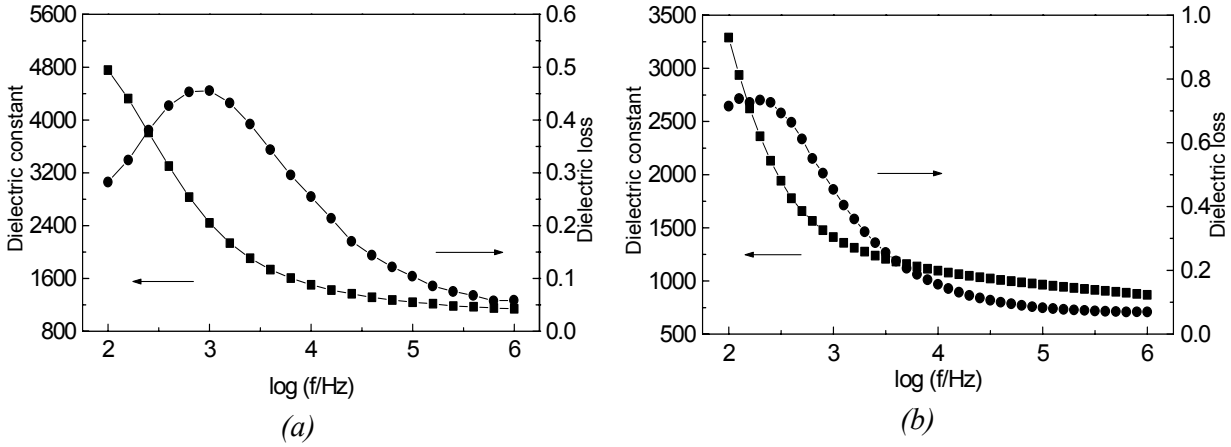

Fig. 5.5. Dielectric constant and dielectric loss as a function of frequency for PZT-Pt15 (a) and PZT-Pt25 (b).

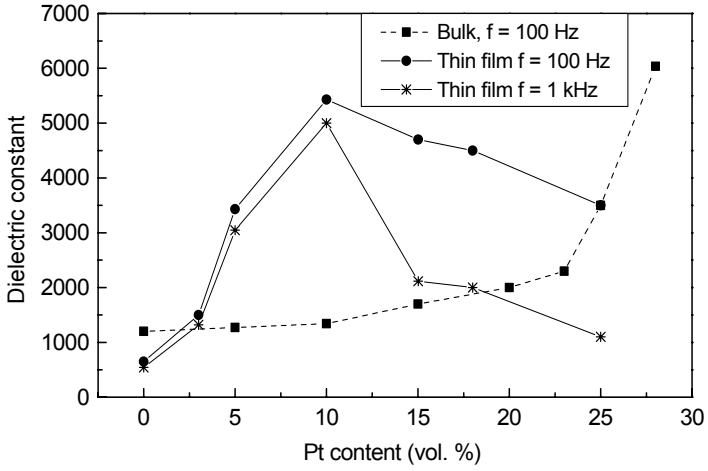

Fig. 5.6. Dependence of dielectric constant on Pt content for bulk material, measured at 100 Hz and for PZT-Pt films, measured at 100 Hz and 1 kHz.

The temperature dependence of the dielectric constant was also analyzed. The ε values calculated from capacitances measured at 10 kHz are plotted as a function of temperature for PZT and PZT-Pt films in Fig. 5.7. The maximum temperature obtained is only 250 °C [i], which is still below the Curie temperature given in literature for PZT (360-390 °C). As observed from the ε-*T* plots, ε increases up to 250 °C for PZT film while it seems to saturate around 200 °C for PZT-Pt10 film. It is noted that the ε-*T* plot of the latter film exhibits a quite broad maximum. That maximum shifts to 175 °C for PZT-Pt15 and to 150 °C for PZT-Pt18 with the further increase of ε around 200 °C. The latter observation possibly relates to the thermally activated behavior of charge carrier concentrations, which induce a capacitance increasing with increasing temperature.

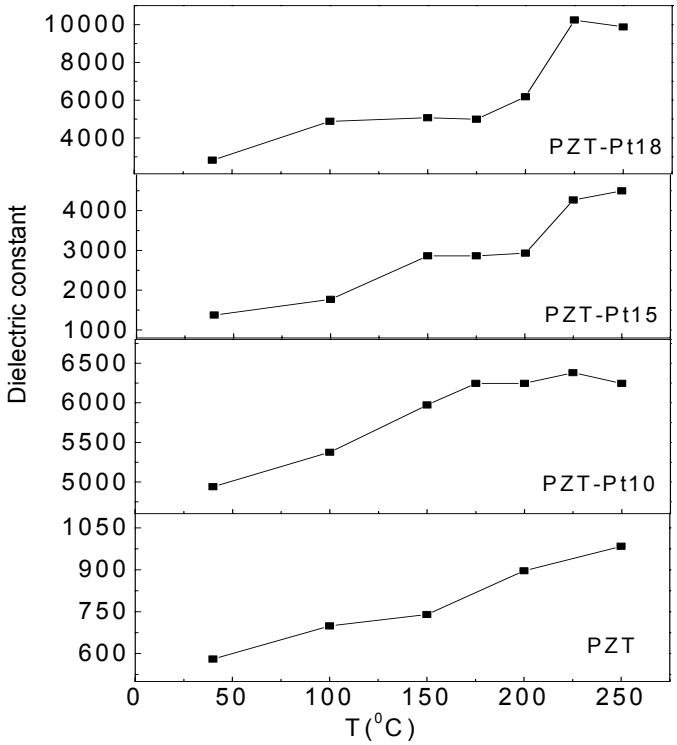

Fig. 5.7. Dielectric constant as a function of temperature for PZT-Pt films.

b. I-V characteristics

The *I-V* curves obtained for PZT and PZT-Pt films, irrespective of the composition, exhibit an asymmetry due to the asymmetric geometry of Au/PZT-Pt/Nb-STO capacitors, as can

[i] the temperature is limited by the set-up.

be seen in Fig. 5.8. The leakage current increases several orders with increasing Pt contents, from 5×10^{-7} for pure PZT to 3×10^{-3} A/cm^2 for PZT-Pt25 at 100 kV/cm. Most pronounced is the shift to lower fields of the threshold field, where Schottky emission is initialized. More details on *I-V* analysis will be presented in Chapter 6.

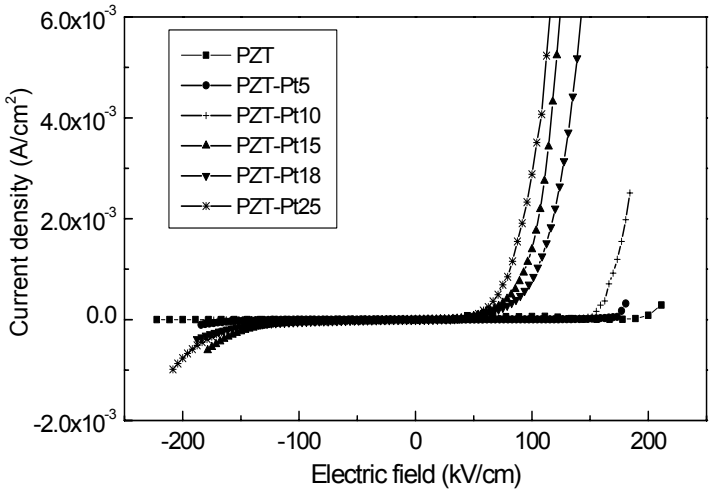

Fig. 5.8. *I-V* curves of PZT-Pt films measured at room temperature.

c. Polarisation behaviour

All samples demonstrated asymmetric *P-E* loops, which is also due to the asymmetric geometry of Nb-STO/PZT-Pt/Au capacitors. For films with Pt contents above 5 vol.% the loops shifted vertically once the voltage was applied, similarly to what was observed in compositionally graded ferroelectric devices prepared with BST, PZT and PLZT [6-8]. The physical mechanism for the onset shifting has been proposed to be due to either the build-up of potential across the graded films [6] or due to the asymmetrical leakage current [9-10]. For comparison between samples, the loops were corrected for the shift.

In Fig. 5.9 we present *P-E* loops, measured at frequencies from 100 Hz to 1 kHz, for PZT and PZT-Pt films. From these measurements, two important features were observed:

- In the above-mentioned range of frequency, while PZT and PZT-Pt3 films show almost no frequency dependence, films with higher Pt contents exhibit a significant decrease of the remanent polarisation and coercive field with increasing frequency.

- With addition of Pt, the loops shrink both in vertical and horizontal directions, showing a decrease in both polarization and coercive field. From 0 to 5 vol.% Pt, the polarizations

have values around 21-24 μC/cm^2. At 10 vol.%, it drops drastically to 14.5 μC/cm^2 at f = 100 Hz and to 7.5 μC/cm^2 at f = 1 kHz. The polarization almost vanishes at 25 vol.% Pt with the value of only 1.7 μC/cm^2 at f = 1 kHz. The remanent polarisations and coercive fields derived from *P-E* loops are listed in Table 5.1.

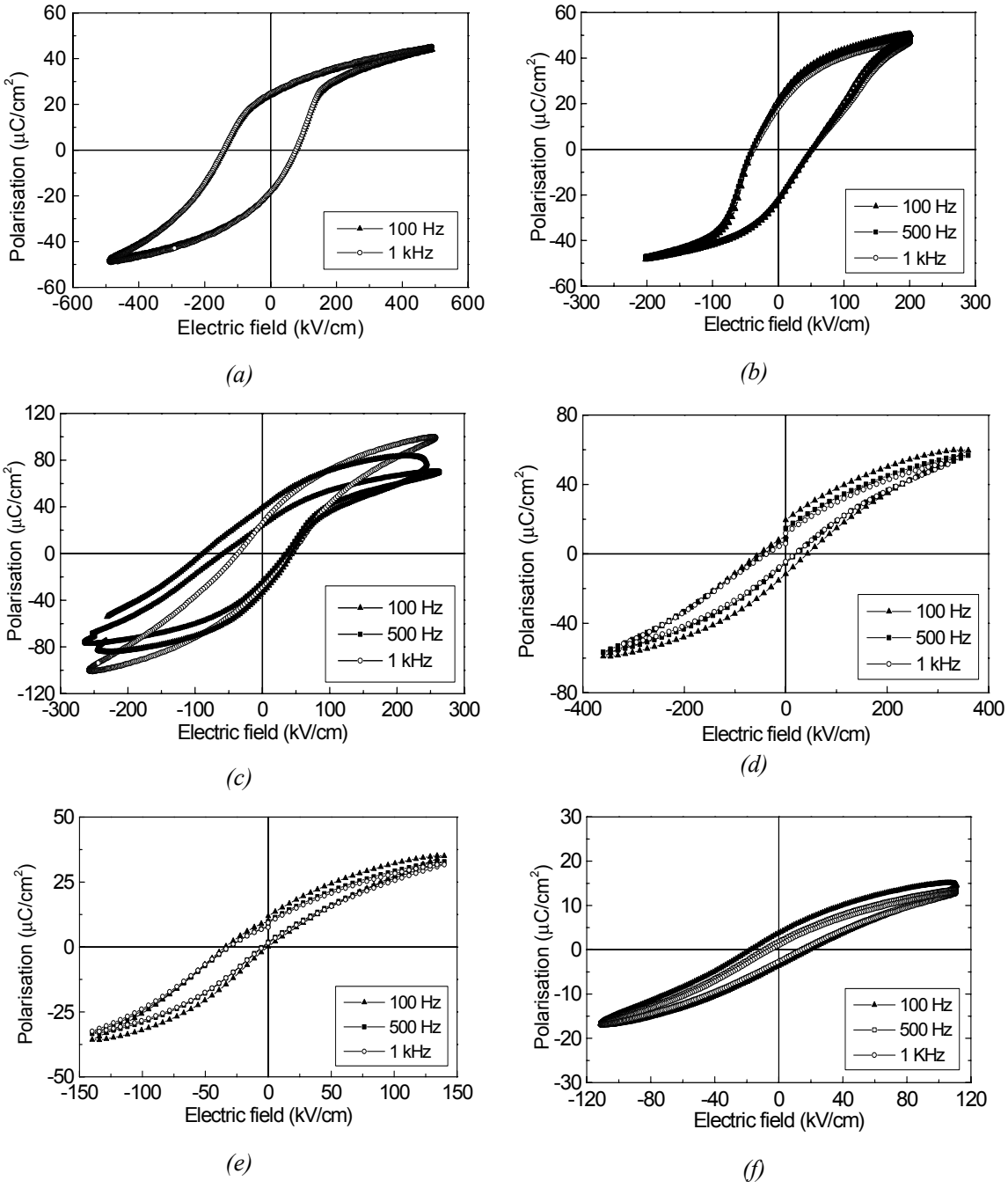

Fig. 5.9. *P-E* loops of PZT-Pt samples, measured at 100 Hz, 500 Hz and 1 kHz for: PZT (a), PZT-Pt3 (b), PZT-Pt5 (c), PZT-Pt10 (d), PZT-Pt15 (e) and PZT-Pt25 (f).

Table 5.1. Remanent polarisations and coercive fields measured at 100 Hz and 1 kHz for PZT-Pt thin films with different Pt contents.

Sample	f = 100 Hz		f = 1 kHz	
	P_r (μC/cm^2)	E_c (kV/cm)	P_r (μC/cm^2)	E_c (kV/cm)
PZT	21.0	109.0	21.0	109.0
PZT-Pt3	21.5	45.0	21.0	45.0
PZT-Pt5	24.5	49.0	21.0	41.0
PZT-Pt10	14.5	43.5	7.5	27.5
PZT-Pt15	6.0	17.0	3.8	12.0
PZT-Pt25	3.4	18.0	1.7	10.0

5.3.1.3 Discussion

Based on the electrical properties of the studied PZT-Pt films, we can roughly divide the films into two groups:

- Films with low Pt contents are characterized by a relative smooth surface and a well-defined columnar structure. They exhibit a weak dependence of the dielectric constant, the dielectric loss and the *P-E* loops on frequency (Fig. 5.4). The dielectric constant increases with Pt content while the dielectric loss remains low and invariant. Typical ferroelectric loops were observed in the *P-E* measurements, however with a slight decrease of the polarization and the coercive field with increasing Pt content (Fig. 5.9).
- Films with high Pt contents posses rough surfaces and irregular columnar structures. They demonstrate a sharp increase in the dielectric constant with decreasing frequency, accompanied by a loss peak around 1 kHz (Fig. 5.5). The dielectric constant decreases with Pt content while the dielectric loss rises to extremely high value. In addition, the ferroelectric loops significantly shrink with increasing frequency and increasing Pt content (Fig. 5.9). The loops are very narrow with low remanence, which resemble those typical for relaxor ferroelectrics (see Chapter 1). Other important features include the shifting of the onset voltage under applied field, the smearing of the temperature at which the dielectric constant reaches a maximum.

a. Frequency dependence of dielectric constant and dielectric loss

The frequency dependence of the dielectric constant of the first group (Pt content below 10 vol.%) can be fitted to the well-known universal law: $\varepsilon \sim f^{n-1}$ [11], as can be seen from the logarithmic plot in Fig. 5.10. The value of n is very close to unity, in the range of 0.973-0.982. The observed behavior indicates that there is no relaxation process occurring in the studied frequency range. The high loss at low frequency is due to the dc conduction [11], and in this case, the leakage current of the film. The slight increase of tan δ at around 1 MHz can be attributed to another resistance in series with the system, originated from either the film/electrode interface or the PZT/Pt interface resistance (note that the increase in loss in PZT-Pt samples are more significant than in pure PZT). It also can correspond to a relaxation of ion vibration, more specifically, the shift of Ti^{4+} ions inside the octahedron, which usually takes place at high frequency of 100 MHz [12].

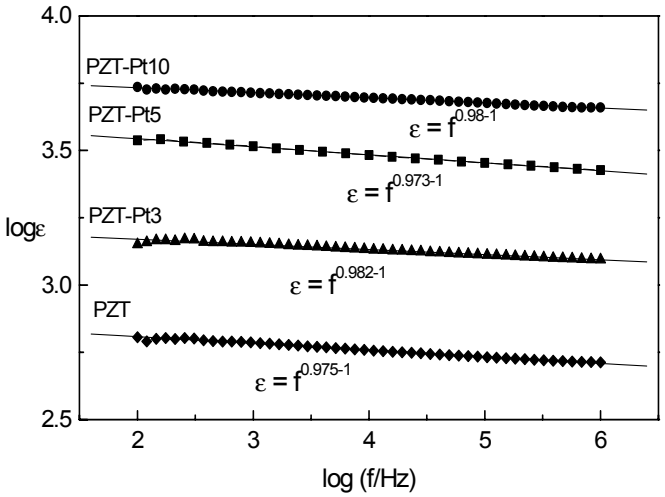

Fig. 5.10. The logarithmic representation of the dielectric constant versus frequency. Solid lines represent linear fittings.

A loss peak around 1 kHz observed for the second group (Pt content above 10 vol.%) implies a relaxation of polarisation process. Low frequency relaxations in ferroelectrics include dipole switching or domain wall relaxation and space charge relaxation [13]. The former however is significant only at temperatures near T_C, which is around 360-390 °C for PZT. Hence it is more likely that the loss peaks observed in our case correlate to the space charge relaxation, which is associated with the formation of charges at the film/electrode interface and at the PZT/Pt interfaces inside the film. The former is due to

accumulation/depletion of charge carriers at the interface between the film and the electrode and hence, is related to the leakage current. The latter is well-known as the Maxwell-Wagner effect in inhomogeneous medium, arising from the difference in conductivities of various phases in contact [14]. This effect is also responsible for the drastically increase of the dielectric constant at low frequencies. In our case, the appearance of a loss peak in high-Pt content films is possibly due to high conductivity and a large amount of PZT/Pt interfaces in those films.

b. Leakage current

The leakage current in PZT-Pt films is considered due to charge carrier injection from the electrode to the film over the Schottky barrier at the film/electrode interface. The current density is exponentially inversely proportional to the barrier height, which is determined by the difference between the work function of the metal electrode and the electron affinity of the ferroelectrics. When different bottom and top electrodes are employed, the *I-V* curve will be asymmetric to the voltage polarity, as observed in Fig. 5.8.

The shift of the threshold voltage for Schottky emission towards smaller values with Pt addition can be intuitively understood if one takes into account the fact that the effective electrical field in the case of a composite thin film will be larger than simply the ratio of the applied voltage over the thickness. Due to the dispersion of many conducting particles, in which there is no electrical field, the electrical field is redistributed across the composite thin film. The increase of leakage current of several orders with Pt addition however could not be explained alone by the shortening of the ferroelectric phase. It is attributed to the change of the Schottky barrier height at the film/electrode interface in the presence of nano-Pt particles. A more thorough analysis of *I-V* characteristics will be presented in Chapter 6.

c. Frequency dependence of the P-E loops

The switching time for domains in PZT films is usually in the range of a few hundred nanoseconds, which means that a frequency below 1 MHz provides enough time for fully switching of the polarization. According to Scott [15], the reason why the coercive field varies with frequency is that domain switching in a ferroelectric involves domain wall motion, which has an increasing resistance or viscosity with increasing frequency. It results in the following empirical relationship for coercive field: $E_c \sim f^{1/m}$, where $m = 6 \div 7$ [16].

From this relationship one can expect a negligible effect of frequency in the range of 100 Hz to 1 kHz, as we observed for pure PZT and PZT-Pt3 (Fig. 5.9a-b).

The significant decrease of the remanent polarisation with increasing frequency, observed for other PZT-Pt samples (Fig. 5.9c-f) reveals the contribution of a non-switching, but strongly frequency dependent component to the total polarisation. The space charge polarisation is well-known as one of the non-switching sources. Since its contribution is more significant at low frequency, the *P-E* loop inflates with decreasing frequency. The opening of the *P-E* loop at high electric fields also resulted from that non-switching source. At high enough fields, where the switching polarisation tends to saturate, the leakage current continues to rise, increasing the space charge polarisation at the film/electrode interface and hence the total polarisation.

d. Thin film versus bulk material

- The enhancement of the dielectric constant

Addition of Pt in a PZT matrix results in the increase of the dielectric constant in both bulk and thin film material. There are, however, several distinguished features between bulk and thin film:

- The enhancement factor of the dielectric constant in thin films is higher than in bulk material (see Fig. 5.6).
- In bulk material, the dielectric constant increases with the Pt content as a power law, following the percolation theory with a critical volume fraction [i] of 0.29 (see Chapter 3). For thin films, the power law is not obeyed. At Pt contents higher than 10 vol.% the dielectric constant however decreases with increasing Pt content.

The above difference between PZT-Pt bulk and thin film is possibly due to the difference in Pt particle sizes: micron-size (> 0.5 μm) in bulk and nano-size (< 20 nm) in thin films.

Considering a conducting-insulating mixture, at a certain volume fraction of the conducting phase, a higher enhancement factor of the dielectric constant is expected if the critical volume fraction shifts to a lower value. Maliaris *et al*. [4] have shown that the critical volume fraction drops when the conducting particles are about 16 times smaller than the insulating ones. However, even though the ratio of PZT over Pt particle sizes in thin films is

[i] A volume fraction corresponds to the percolation threshold, i.e. when a percolation conducting path is formed in the system. The predicted value by the effective medium theory is 0.33.

around 10-20 while that for the bulk is around 1-2, the percolation threshold in thin films was not lower than in the bulk. Even at 40 vol.% Pt content an insulating behavior was observed, i.e. the percolation path is not yet formed in the film.

On the other hand, the increase in dielectric constant can also be attributed to the formation of a space charge layer at the PZT/Pt interfaces. Since the interface area is inversely proportional to the particle size, the influence of this double layer will be much more pronounced in thin film than in bulk. This explains the sharper increase of the dielectric constant with increasing Pt content observed for thin films (Fig. 5.6). The consistence of the experimental data with theory is satisfied only if the decrease of the effective thickness of the PZT phase in the presence of the Pt phase is taken into account, while the surface interaction between two phases is neglected.

It is not yet clear why in thin films the dielectric constant decreases with further increasing Pt content above 10 vol.%. Since no other phase than perovskite PZT phase was detected in XRD diagrams, this decrease is not due to the formation of the pyrochlore phase or any other phases. It possibly relates to the decrease of the PZT grain size or to the formation of an interface layer between PZT and Pt phases, which has a low dielectric constant. At high Pt contents, the effect of these low dielectric constant layers could be dominant over the effect of the space charge layer, hence resulting in the decrease of the total dielectric constant.

- The change of *P-E* loops

The *P-E* loops of both PZT-Pt bulk and thin film shrink with Pt addition. The effect is however much stronger in thin films than in bulk. A PZT-Pt23 bulk sample remains ferroelectric with a reasonably high polarization of 18 $\mu C/cm^2$ at 100 Hz (see Chapter 3). Meanwhile for PZT-Pt thin films the polarizations drops quickly at 10 vol.% Pt and almost vanished at 25 vol.% Pt (see Table 5.1).

The simple mixing rule, based on the diluting effect of non-ferroelectric Pt phase, explains the decrease of polarization with increasing Pt content in the bulk, but fails in thin films. Hence, the size-effect should be taken in consideration. On the one hand, we can regard that the dispersion of the Pt phase shortens the PZT phase down to the limited size, under which PZT appears as a paraelectric phase. Even though the theoretical value of that critical thickness, calculated by a mean-field Ginzburg-Landau approach is around 20 nm at room temperature [17], to our observation a 60 nm thick PZT film already lost the switch-

ing property (see Appendix). On the other hand, the nano-sized Pt particles dispersed throughout the PZT matrix can be considered as impurities centers, which break up in some degrees the periodicity of the long-range order in PZT phase. This breaking of periodicity split the micro-sized domains of PZT into smaller sub-micro sized domains or even nano-polar domains, depending on the concentration and dispersion of the Pt phase. Since the stability of the domain is inversely proportional to its size, the nano-polar domains are not stable and are driven to paraelectric upon a thermal agitation. As a result, the total polarization and also the coercive field are expected to drop quickly with further Pt addition. That phenomenon does not occur in bulk because the size of both Pt and PZT particles is in the micrometer scale and so is the distance between them. The domain structure hence is not expected to change in this case.

e. Relaxor-like behaviour?

The slim but still non-linear *P-E* loops obtained for PZT-Pt films with Pt contents above 10 vol.% (Fig. 5.9e-f) look identical to the characteristic *P-E* loop of relaxor ferroelectric material (see Chapter 1). Important features of relaxor ferroelectrics are (a) frequency dependent and diffuse phase transition (b) slow degeneration of the hysteresis as the temperature increases through the dielectric maximum, referred to the square-to-slim loop transitions. Even though the exact nature of their peculiar physical properties is not yet clear, the origin mainly stems from the nano-scale chemical/structural inhomogeneity that breaks the translational invariance of the polarization. Impurities, defects, incomplete or inhomogeneous cation ordering, macroscopic fluctuations in chemical composition, core/shell structure, etc. can lead to the smearing of the ferroelectric phase transition. The substitution of La into a PZT host can be taken as a typical example. La^{3+} substitution hinders ferroelectric ordering by disrupting the coupling between BO_6 octahedra. When the La content increases, the structure changes from a long-range-ordered ferroelectric state to an ensemble of polar regions (~ 10 nm). It is known that the energy barrier separating alternative domain states scales with the domain volume. Near a domain dimension of 10 nm that energy barrier is small comparable to k_BT at room temperature, making the polar region unstable [18]. The studies made by Viehland [19] shows evidences from TEM observation of the transformation from normal micron-sized domains to polar nanodomains around 25 at.% of La in PLZT [19].

The variation of the polarization and the coercive field of PZT-Pt films with respect to Pt content bears a resemblance to the relaxor-ferroelectric transition of PLZT. The Pt entities

can be considered to act as La^{3+} in breaking the long-range order of polarization, which makes the remanent polarization decrease with increasing Pt content and disappear at certain contents. Even though the Curie temperature could not yet be determined due to the limit of measurement set-up, PZT-Pt films seems to have a broader ferroelectric-paraelectric phase transition, shifting to lower temperatures as compared to pure PZT (see Fig. 5.7). Other evidences such as the frequency dependence of the phase transition, the formation of nano-polar domains, etc. are necessary to conclude if the Pt phase really induces the relaxor-ferroelectric transition.

5.3.2 Multi-layer $(PZT/PZT\text{-}Pt)_n$ film: influence of the Pt dispersion

PZT-Pt layers are separated by PZT layers in a multi-layer $(PZT/PZT\text{-}Pt)_n$ film in order to reduce (a) the leakage current and (b) the surface roughness of the composite film.

5.3.2.1 Experimental and results

The multi-layer film consists of 25 alternating layers of PZT and PZT-Pt25, the thickness of each layer is around 10 nm. The film was prepared by alternating deposition using multi-targets (E = 4 J/cm^2, pO_2 = 0.1 mbar, f = 10 Hz). The film morphology can be seen from a cross-section SEM image presented in Fig. 5.11. The surface smoothness of the multi-layer film is not much enhanced in comparison with single-layer PZT-Pt25 films.

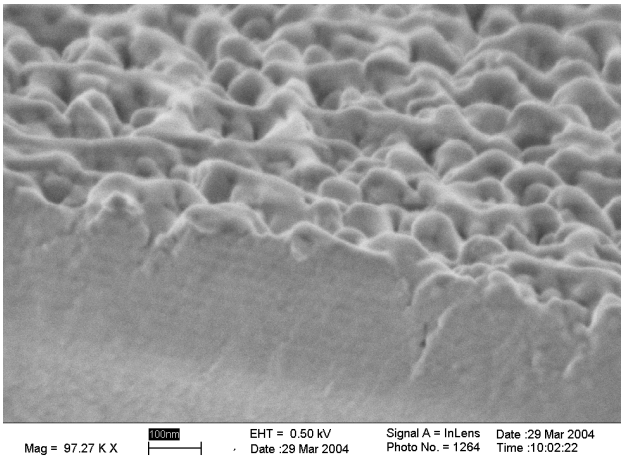

Fig. 5.11. Cross-section SEM of a $(PZT/PZT\text{-}Pt25)_n$ multi-layer film.

With respect to conductivity, the multi-layer film has a lower leakage current than the single-layer PZT-Pt25 film. The current density is 5×10^{-4} A/cm^2 at 100 kV/cm, which is comparable to the value obtained for a single-layer PZT-Pt10 film. The frequency dependence

of ε and *tan* δ for the multi-layer film is presented in Fig. 5.12. The dielectric constant measured at 100 Hz is 1260, which is in between those values of PZT (600) and PZT-Pt25 (3500) films. The following relationship was observed for the dielectric constant versus frequency: $\varepsilon \sim f^{n-1}$ with n = 0.982. The magnitude of *tan* δ is considerably high (around 10 %) but a loss peak was not observed in the given frequency range. A well-defined *P-E* loop was recorded, as can be seen in Fig. 5.13. The remanent polarization is 37.5 μC/cm^2, which is even higher than the value of 15 μC/cm^2 obtained for a PZT film having the same film thickness (see Appendix). The coercive field is 176 kV/cm, comparable to that of PZT film. The loop however tilts and does not saturate at high fields up to 800 kV/m. The rounder tip of the loop indicates a reasonable amount of leakage current at high fields.

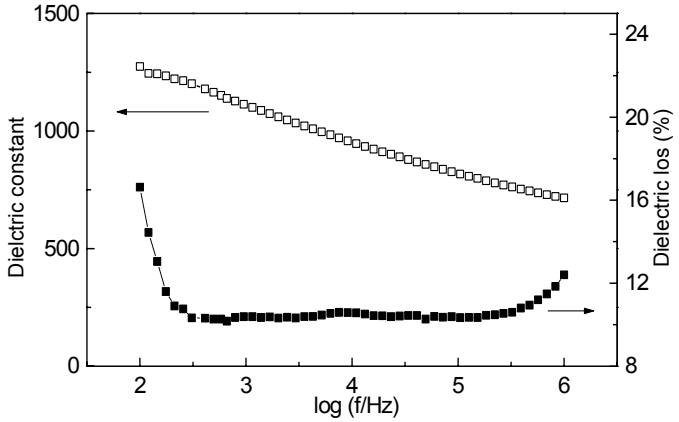

Fig. 5.12. Frequency dependence of dielectric properties of a $(PZT/PZT\text{-}Pt25)_n$ film.

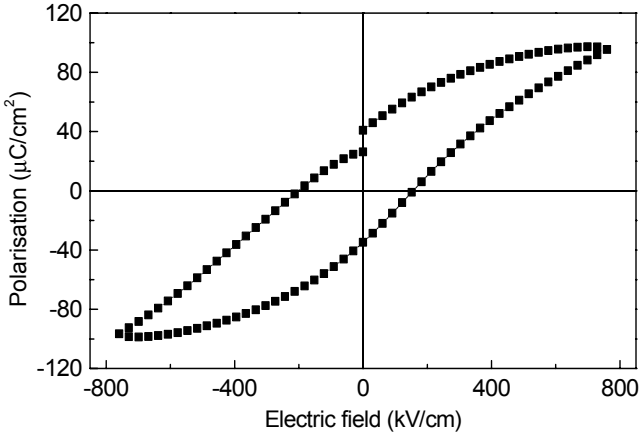

Fig. 5.13. *P-E* loop of a multi-layer $(PZT/PZT\text{-}Pt25)_n$ film measured at 1 kHz.

5.3.2.2 Discussion

The multi-layer $(PZT/PZT\text{-}Pt25)_n$ film has an average Pt content equal to that of the single-layer PZT-Pt10 film. It explains the same order of leakage current obtained for the two films. The dielectric constant of the single-layer PZT-Pt10 film (5400 at 100 Hz) is, however, much higher than that of the multi-layer (1260 at 100 Hz). This observation indicates that not only the content but also the spatial distribution of Pt phase determines the effective dielectric constant of PZT-Pt system. Actually, a multi-layer film can be considered as series of capacitors and the total dielectric constant ε can be calculated as following:

$$\frac{d}{\varepsilon} = \frac{d_{PZT}}{\varepsilon_{PZT}} + \frac{d_{PZT-Pt}}{\varepsilon_{PZT-Pt}} \tag{5.1}$$

where d is the total film thickness, ε_{PZT} and $\varepsilon_{PZT\text{-}Pt}$ the dielectric constants of PZT and PZT-Pt25, respectively. The value of ε depends on the thickness of each layer but should be in between ε_{PZT} and $\varepsilon_{PZT\text{-}Pt}$. Using d = 250 nm, ε_{PZT} = 600, $\varepsilon_{PZT\text{-}Pt}$ = 3500, d_{PZT} = 130 nm, $d_{PZT\text{-}Pt}$ = 120 nm, Eq. (5.1) provides a corresponding value of 1000 for ε. The difference between the calculated value (1000) and the experimental value (1260) is possibly due to errors in determining the thickness and dielectric constant of each phase. The high dielectric loss of the multi-layer film resulted either from high loss of the PZT-Pt25 component or from a large concentration of charged impurity centers, especially at the interfaces between layers.

Similarly, with respect to the ferroelectric behaviour, one should not treat a $(PZT/PZT\text{-}Pt25)_n$ multi-layer simply as a system containing 10 vol.% Pt. The phase distribution of the multi-layer and single-layer films is schematically drawn in Fig. 5.14, where the Pt particles are represented as spheres. In a single-layer PZT-Pt10, Pt particles are homogeneously distributed all over PZT matrix. The average separation distance between Pt particles is around 5-10 nm, as can be roughly estimated from TEM picture in Fig. 5.2a. Those nano-Pt particles may act as impurity centers and induce the formation of PZT nano-sized domains. Since those nano-domains are easily driven from ferroelectric to paraelectric state, the single-layer film exhibits low values of polarization (7.5 $\mu C/cm^2$) as well as of coercive field (27.5 kV/cm).

Meanwhile, in a multi-layer there are regions of PZT matrix free of Pt dispersion, in which ferroelectricity is still retained. One may question the existence of ferroelectricy in such a thin layer of 10 nm only, since the 60 nm thick PZT film already shows paraelectric

behaviour (Appendix). However, it should be emphasized that those 10 nm PZT layers are, firstly, sandwiched between other PZT-based layers, and secondly, are multiplied at least 10 times. The long-range interaction, which is the origin of ferroelectricity, is therefore kept over the whole thickness of the multi-layer film. Our case is similar to PZO/PTO system, which exhibits ferroelectricity even when the periodicity of each layer is only few unit cell (~ 1-2 nm) [20].

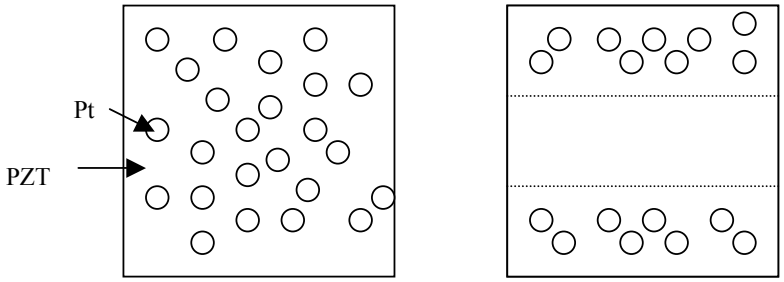

Fig. 5.14. Schematic representation of Pt distribution in a single-layer PZT-Pt (a) and in a multi-layer $(PZT\text{-}Pt/PZT)_n$ (b).

The tilting of the *P-E* loop is known to originate from the effect of a space charge layer at the film-electrode interface [21]. The charged defects near the interface between layers may pin domain walls and create a localized space charge field opposing the applied field, causing a non-saturation behavior [22].

In conclusion, the dielectric constant and dielectric loss of the multi-layer $(PZT/PZT\text{-}Pt25)_n$ film have values in between those of single-component films, and very much different from those obtained for single-layer film having the same Pt content. This observation reveals the important role of the spatial distribution of the Pt phase. Similarly, while PZT-Pt10 shows evidence of the degradation in ferroelectricity, the multi-layer film still exhibits good ferroelectric properties. The latter is explained by the preservation of the long-range interaction in the PZT phase over the whole system.

5.3.3 Influence of the film roughness (films deposited at low and high energy densities)

For a good electrical performance, a smooth film surface is always desired since it provides a homogeneous electric field distribution, a sharp and less defected interface between the film and the electrode. In Chapter 4, we already showed that the film roughness could be tailored through adjusting the laser energy density. The surface roughness of a film de-

posited at low energy density is much lower compared to a film deposited at high energy density.

5.3.3.1 Results

In Fig. 5.15a we present the TEM image of a film deposited at 1.5 J/cm^2 using a PZT-Pt15 target. From XRF analysis, the Pt content of this film is comparable with a film deposited from a PZT-Pt10 target at higher energy density of 4 J/cm^2. The TEM image of the latter film is presented in Fig. 5.15b. As can be seen from the pictures, the film deposited at 1.5 J/cm^2 is much smoother than the film deposited at 4 J/cm^2. A columnar structure is revealed, but the grain boundaries between columns are not clearly visible.

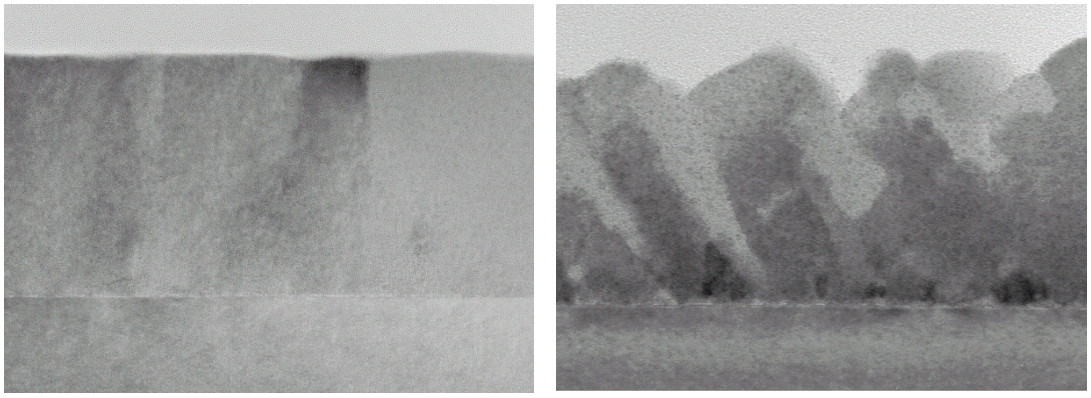

(a) *(b)*

Fig. 5.15. Cross-section TEM image of films deposited at 1.5 J/cm^2 (a) and at 4 J/cm^2 (b).

Both films show little frequency dependence of the dielectric constant and dielectric loss in the frequency range of 100 Hz to 1 MHz (see Fig. 5.16a). Values obtained for *tan* δ are low and in the same range as 0.03 for the smooth and 0.04 for the rough film. The dielectric constant of the smooth film (2830 at 100 Hz), however, is lower compared to the rough one (4400 at 100 Hz). The smooth film also exhibits a lower leakage current (see Fig. 5.16b).

The ferroelectric properties of the two films demonstrate quite different features, as can be seen in Fig. 5.17. The coercive fields measured at 1 kHz are 82 kV/cm and 27.5 kV/cm, while the remanent polarizations are 30 μC/cm^2 and 7.5 μC/cm^2, for the smooth and the rough films, respectively. Again we observed a frequency dependence of the *P-E* loops, illustrated in the decrease of the polarization and coercive field with increasing frequency.

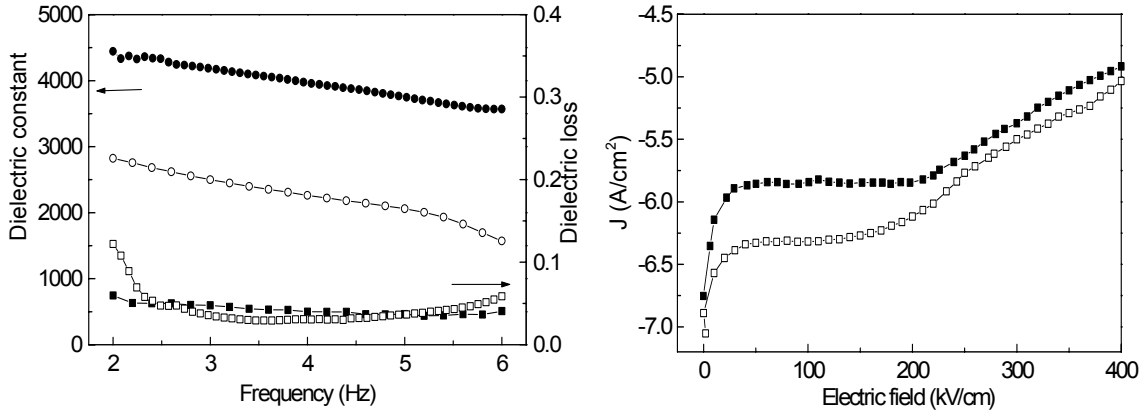

Fig. 5.16. (a) Frequency dependence of the dielectric constant and dielectric loss and (b) *I-V* characteristics of the smooth (open points) and the rough films (solid points).

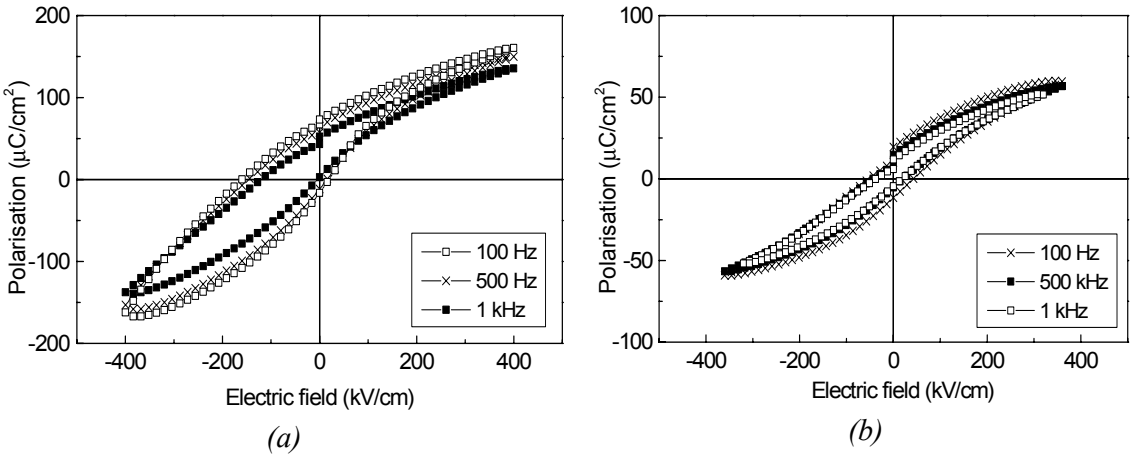

Fig. 5.17. *P-E* loops of the smooth (a) and the rough films (b) measured at different frequencies.

5.3.3.2 Discussion

Under an external electric field, a smoother film surface provides a more homogeneous field distribution, and hence a lower leakage current than a rougher surface. A lower leakage can also be attributed to a lower surface state density at the film/electrode interface, which is obtained by a smooth film surface. However, the difference in leakage current of the smooth and the rough films is not large, indicating the more important role of Pt fraction in the film.

The relationship between the dielectric constant, the polarization and the film roughness is not straightforward. The distribution and/or the size of Pt particles, which actually governs

the film roughness, possibly play a more important role. From the TEM images the location of Pt particles can hardly be observed for the smooth film, most likely because the sizes of the Pt particles lie below the measurement resolution. We therefore assume that there exists a critical size for Pt particles, above which phase segregation occurs, leading to the film roughening.

The formation of an interface layer with low dielectric constant between a PZT film and Pt electrodes is well-known in literature [23, 24]. This low dielectric layer results in the decrease of the total dielectric constant. With decreasing film thickness that so-called "dead-layer" effect becomes more significant. If we assume that the same phenomenon occurs at the PZT/Pt interfaces in a PZT-Pt film, the modification of the dielectric constant by Pt dispersion is influenced by at least 3 factors: the reduction of the PZT effective thickness, the formation of a space charge polarization and a low-dielectric constant layer at PZT/Pt interfaces. Among them, the first two increase the total dielectric constant while the last one lowers it. The lower dielectric constant observed for the smooth film is possibly due to the dominance of the last factor when the Pt particles are very small.

The different polarization behaviour of the smooth versus the rough films may correlate to the stability of the ferroelectric state. According to Ref. [25], the total free-energy for the transformation from the ferroelectric to the paraelectric state mainly consists of three components: (a) the chemical energy, which relates to the defect concentration, in this cases the Pt content; (b) the elastic energy, which relates to lattice misfit and (c) the electrostatic energy, which relates to the dipole-dipole interaction, the depolarization field and the applied field. Among them, the elastic strain component is the one with a negative value, hence lowering the total free energy and favoring the existence of the ferroelectric state. The contribution of the elastic strain energy in the smooth film is expected to be larger than in the rough film, since in the latter the strain caused by lattice misfit is all relaxed through formation of grain boundaries, dislocations, ect.

5.4 Conclusions

PZT-Pt films grown on (001) $SrTiO_3$ substrates are preferentially oriented in the (001) orientation. Films consist of PZT columns with lateral size of around 60-80 nm and spherical Pt particles with size of 3-10 nm. Films are smooth with the surface roughness increasing with Pt content.

The electrical properties of PZT-Pt films significantly differ from pure PZT films. Below 10 vol.% Pt, the dielectric constant increases with increasing Pt content, while the dielectric loss remains low. The maximum enhancement of the dielectric constant is a factor of 8 at 10 vol.% Pt, compared to pure PZT. With further increasing Pt content above 10 vol.%, the dielectric constant decreases. High-Pt content films exhibit high loss with a loss peak around 1 kHz. The loss is attributed to the space charge relaxation, which arises from the interface charges at the film/electrode and the PZT/Pt interfaces.

The *P-E* loops shrinks upon Pt addition. The remanence almost disappears for PZT-Pt25 film. PZT-Pt films also are distinguished from pure PZT by the strong frequency dependence of the polarization. This frequency dependence arises from a non-switching but frequency dependent component, which can be the space charge polarization. The asymmetry of the build-up charges at top and bottom electrodes is considered to cause the *P-E* loops shifting along the polarisation axis.

PZT-Pt composite films exhibit higher leakage current than pure PZT film. The increase of leakage current is due to the re-distribution of the electric field in the presence of conducting Pt particles and the change of the barrier height at the film/electrode interface.

The influence of Pt addition on the dielectric properties observed in PZT-Pt thin films differs from PZT-Pt bulk. The difference is attributed to the nano-size effect of Pt particles in thin films. The dependence of the dielectric constant on the Pt content follows percolation theory in bulk material, but not in thin films. The latter observation is possibly because in thin films the contribution to the dielectric constant of space charge polarization at PZT/Pt interfaces is dominant over the decrease of the PZT effective thickness. Since the space charge polarization is inversely propotional to the particle size, one can expect the produced effect is much larger for nano-sized particles in thin films than for micron-sized particles in bulk.

If the decrease of the polarization with increasing Pt content, as observed in bulk material, can be explained by a diluting effect of a non-ferroelectric phase, in thin films it fails in explaining the vanishing of the remanent polarization at Pt contents far below the percolation threshold. The role of Pt particles as impurities to break down the periodicity of the polarization hence must be taken into account. Small Pt entities dispersed all over the PZT matrix and about 5-10 nm separated from each other, possibly split the micro-sized PZT domains into nano-sized domains. Since the stability of the domain is inversely proportional to its size, the paraelectric-ferroelectric transition of those nano-domains may take

place just by thermal vibration around room temperature. The narrowing and finally disappearance of the hysteresis in the *P*-*E* loops, together with the broader phase transition, observed from ε vs. *T* plots, resemble the characteristics of relaxor ferroelectrics. Other evidence is necessary in order to confirm whether Pt addition induces the relaxor behaviour in PZT.

The electrical properties of PZT-Pt films depend not only on the Pt content but also on the spatial distribution of the Pt phase. When small Pt particles, separated few nanometers from each other, are 3D homogeneously distributed in a PZT host, the ferroelectricity is degraded. Meanwhile, good ferroelectric performance is still observed in a multi-layer $(PZT/PZT\text{-}Pt)_n$ film, where Pt particles are separated by 10 nm thick layers of PZT. The preservation of the ferroelectricity is either due to the expansion of micro-sized domains of PZT in lateral direction or due to the existence of the long-range order along the film thickness. The dielectric constant and dielectric loss obtained for a multi-layer $(PZT/PZT\text{-}Pt)_n$ film are in between the values of single component films, and very much different from those of a single PZT-Pt film having the same Pt content.

The dielectric and ferroelectric properties of PZT-Pt films are dependent on the film roughness. A smoother film exhibits a lower leakage current due to a more homogeneous distribution of electric field and a less-defected film/electrode interface. The effect of film roughness on the dielectric constant and polarisation is not clearly understood in terms of roughness. It is assumed to originate from the size-effect of Pt particles, which in turn influences the film morphology.

References

1. R. Landauer, *Electrical Conductivity in Inhomogenous Media*, pg. 2-45, American Institute of Physics Conference proceedings, No. 40, Electrical Transport and Optical Properties of Inhomogenous Media, New York, 1962.
2. M. Sahimi, *Application of percolation theory*, Taylor and Francis Ltd., 1994.
3. C. Brosseau, A. Beroual and A. Boudida, *How do Shape Anisotropy and Spatial Orientation of the Constituents Affect the Permittivity of Dielectric Heterostructure*, J. Appl. Phys. **88** (2000) 7278.
4. A. Malliaris and D.T. Turner, *Influence of Particle Size on the Electrical Resistivity of Compacted Mixtures of Polymeric and Metallic Powders*, J. Appl. Phys. **42** (1971) 614.
5. G. Koster, G.J.H.M. Rijnders, D.H.A. Blank and H. Rogalla, *Imposed layer-by-layer growth by pulsed laser interval deposition*, Appl. Phys. Lett. **74** (1999) 3729.
6. J.V. Mantese, N. W. Schubring, A.L. Micheli, A.B. Catalan, M.S. Mohammed, R. Naik and G.W. Auner, *Slater model applied to polarisation graded ferroelectrics*, Appl. Phys. Lett. **71** (1997) 2047.
7. M. Bazier, M. McElfresh and S. Mansour, *Unconventional hysteresis behavior in compositionally graded Pb(Zr,Ti)O_3 thin films*, Appl. Phys. Lett. **72** (1998) 1121.
8. I. Boerasu, L. Pintilie and M. Kosec, *Ferroelectric properties of $Pb_{1-3y/2}$ La_y $(Zr_{0.4}Ti_{0.6})O_3$ structures with La concentration gradients*, Appl. Phys. Lett. **77** (2000) 2231.
9. R. Bouregba, G. Poullain, B. Vilquin and G. Le Rhun, *Asymmetrical leakage currents as a possible origin of the polarisation offsets observed in compositionally graded ferroelectric films*, J. Appl.Phys. **93** (2003) 5583.
10. L. Zheng, C. Lin, W. P. Xu and M. Okuyama, *Vertical drift of P-E loop in asymmetric ferroelectric capacitors*, J. Appl. Phys. **79** (1996) 8634.
11. A.K. Jonscher, *Dielectric relaxation in solids*, Chelsea Dielectric Press, London 1983.
12. J. Ravez, *Ferroelectricity in solid state chemistry*, C.R. Acad. Sci. Paris, Serie Iic, Chimie, Chemistry **3** (2000) 267.
13. C. Elissalde and J. Ravez, *Ferroelectric ceramics: defects and dielectric relaxations*, J. Mater. Chem. **11** (2001) 1957.
14. A.R. Von Hippel, *Dielectric and Waves*, John Wiley & Sons, New York, 1962.
15. J.F. Scott, *Ferroelectric memories*, Springer, Cambridge 2000.
16. O. Auciello, J. F. Scott and R. Ramesh, *The physics of ferroelectric memories*, Physics today July 1998, 22.

17. T. Tybell, C.H. Ahn and J.-M.Triscone, *Ferroelectricity in thin perovskite films*, Appl. Phys. Lett. **75** (1999) 856.

18. L.E. Cross, *Relaxor ferroelectrics*, Ferroelectrics **76** (1987) 241.

19. X. Dai, Z. Xu and D. Viehland, *Normal to relaxor ferroelectric transformation in lanthanum-modified tetragonal-structured lead zirconate titanate ceramics*, J. Appl. Phys. **79** (1996) 1021.

20. I. Kanno, S. Hayashi, R. Takayama and T. Hirao, *Superlattices of $PbZrO_3$ and $PbTiO_3$ prepared by multi-ion beam sputtering*, Appl. Phys. Lett. **68** (1996) 328.

21. A.K. Tagantsev, M. Landivar, E. Colla, K.G. Brooks and N. Setter, *Depletion, depolarising effects and switching in ferroelectric thin films* in Science and technology of electroceramic thin films, ed. by Auciello and R. Waser, 1995, Kluwer Academic Publisher, pg. 301.

22. S. Bhaskar, S.B. Majumder, P.S. Dobal, S.B. Krupanidhi and R.S. Katiyar, *Dielectric and ferroelectric response of sol-gel derived $Pb_{0.85}La_{0.15}TiO_3$ ferroelectric thin films on different bottom electrodes*, Thin Solid Films **406** (2002) 30.

23. P.K. Larsen, G.J.M. Dormans, D.J. Taylor and P.J. van Veldhoven, *Ferroelectric properties and fatigue of $PbZr_{0.51}Ti_{0.49}O_3$ thin films of varying thickness: Blocking layer model*, J. Appl. Phys. **76** (1994) 2405.

24. C.H. Lin, P.A. Friddle, C.H. Ma, A. Daga and H. Chen, *Effects of thickness on the electrical properties of metalorganic chemical vapor deposited $Pb(Zr,Ti)O_3$ (25-100 nm) thin films on $LaNiO_3$ buffered Si*, J. Appl. Phys. **90** (2001) 1509.

25. S. Semenovskaya and A.G. Khachaturyan*, Ferrolectric transition in a random field: possible relation to relaxor ferroelectrics*, Ferroelectrics **206** (1998) 157.

6

Conduction mechanism in PZT and PZT-Pt films

6.1 Introduction

Understanding the nature of the leakage current in ferroelectric films is important for device operation. As presented in Chapter 5 for PZT-Pt films, high leakage current results in an increase of dielectric loss at low frequency and changes in the *P-E* loop while the asymmetric current is responsible for drifting of *P-E* loop along the polarisation axis. Different models describing the leakage current have been proposed to explain the conduction characteristics of PZT films [1-7]. These models can be divided into two general groups: interface-controlled and bulk-controlled mechanisms. Carrier injection through a blocking contact such as thermionic- Schottky emission and Fowler-Nordheim tunnelling belongs to the first group. The second group includes ohmic conduction, Pool-Frenkel emission and space-charge limited conduction (SCLC). In many cases the favoured transport mechanism is electron injection into the conduction band of the dielectric material at the cathode by thermionic and/or tunnel emission, possibly combined with transport by carrier drift and diffusion in the bulk of the film.

A number of publications on the *I-V* analysis of ferroelectric films have appeared. Most authors, however, did concentrate mainly on the high-field conduction regime using different conduction laws such as SCLC [1], Schottky [2-3], Pool-Frenkel [4], Fowler-Nordheim [5] or mixed conduction [6-7]. Actually, a typical *I-V* characteristic as shown in Chapter 5 consists of several regimes and the cross-over between the regimes is an important feature. An adequate model for conduction should describe all the regimes as well as the cross-over between them.

In this chapter the leakage currents of PZT and PZT-Pt films will be discussed. A model will be proposed to explain the *I-V* characteristics obtained for the films. Subsequently the influence of electrodes, field polarity and film thickness on the conduction will be verified. Finally, the effect of Pt addition on the leakage current of PZT-Pt films will be clarified.

6.2 Experimental

PZT and PZT-Pt films were prepared by PLD on conducting 1 wt.% Nb-STO substrates under the following conditions: T_s = 600 °C, E = 4 J/cm^2, f = 10 Hz, pO_2 = 0.1 mbar, d = 45 mm. The film thickness ranged from 60 to 1500 nm. The synthesis and characterisation of the films are described in detail in Chapters 4 and 5. For electrical measurements, the top Au electrodes of 100 nm thickness and 100×100 μm^2 surface area were sputter deposited at room temperature using a shadow mask. D.c conduction measurements were carried out with a 4140 pA meter (Hewlett-Packard) using a d.c voltage source. The film was poled prior to the measurement to exclude the contribution of a switching current. During the measurement, the voltage was varied in steps of 100 mV, with a delay time of 2 s before readings. The polarity of the applied voltage was considered with respect of the top electrode. For measurements at elevated temperatures, a heating chuck was used which provided a temperature stability of ±2 °C. The temperature was varied from room temperature up to 250 °C. A sketch of the measurement system is shown in Fig. 6.1.

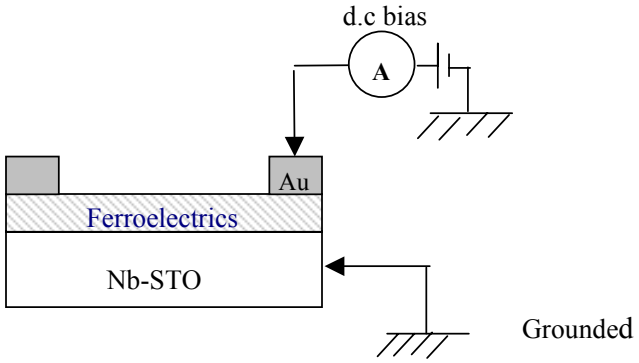

Fig. 6.1. Schematic presentation of the measurement circuit and the geometry of the PZT and PZT-Pt thin film capacitors. The top electrode is connected to a d.c-voltage source. The bottom electrode is grounded.

6.3 Results

6.3.1 I-V characteristics of PZT films

A representative *I-V* curve of a 500 nm thick PZT film, measured at room temperature, is shown in Fig. 6.2 (current in a logarithmic scale). The current values are lower at negative than at positive bias, indicating that the leakage current is dependent on the voltage polarity. In both positive and negative branches, the *I-V* curves can be divided in three regimes.

At low electrical fields, denoted as regime I, the current increases super-linearly with increasing field. At intermediate fields the current saturates (regime II) and is nearly field-independent. At higher fields, the current increases again, indicated as regime III.

In Fig. 6.3 the *I-V* curves are presented for PZT films with a thickness of 60, 250, 500 and 1500 nm. The *I-V* characteristics depend on the film thickness, but the three regimes are clearly visible for all films. In regimes I-II (low and intermediate fields), the current densities of all films almost coincide. The onset of regime III (high field), however, shifts towards lower field strength with decreasing film thickness. The semi-logarithmic *I-V* plots in this regime show almost identical slopes.

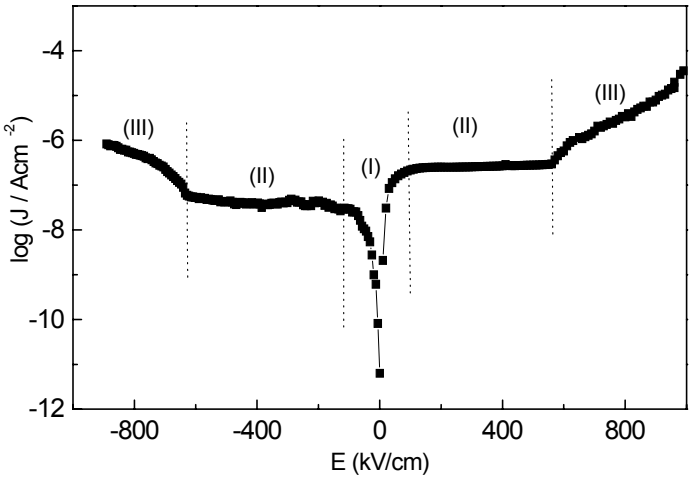

Fig. 6.2. Typical *I-V* curve of the PZT film with thickness of 500 nm. The three regimes I-III are also indicated.

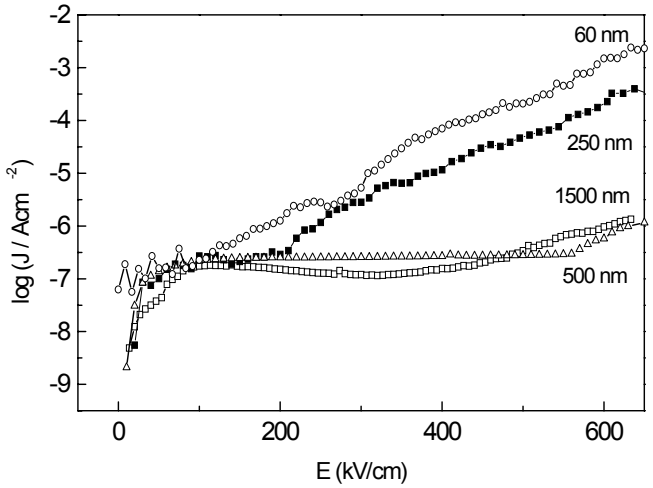

Fig. 6.3. *I-V* curves at positive bias of PZT films with different thickness.

6.3.2 I-V characteristics of PZT-Pt films

In Fig. 6.4 the *I-V* curve obtained for Au/PZT-Pt10/Nb-STO capacitor at negative bias is shown. The shape of the curve does not differ from that obtained for pure PZT (see Fig. 6.2). The three above-mentioned regimes are also clearly distinguished. The magnitude of the leakage current in a PZT-Pt10 film, however, is about a factor 3 higher than for a PZT film with the same thickness. The onset field for regime III for the PZT-Pt10 film decreases significantly with respect to observations for the PZT film.

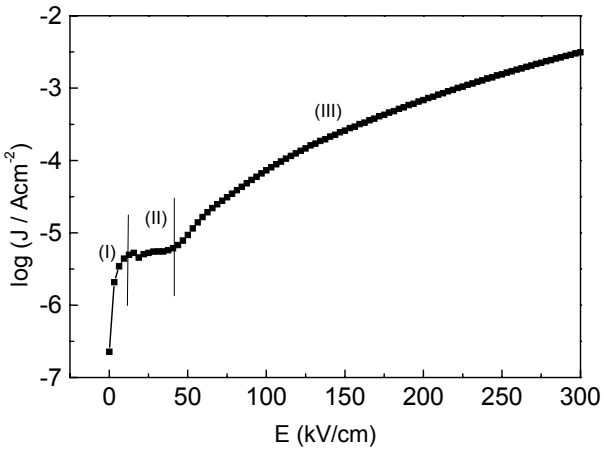

Fig. 6.4. *I-V* characteristic of PZT-Pt10 film at negative bias.

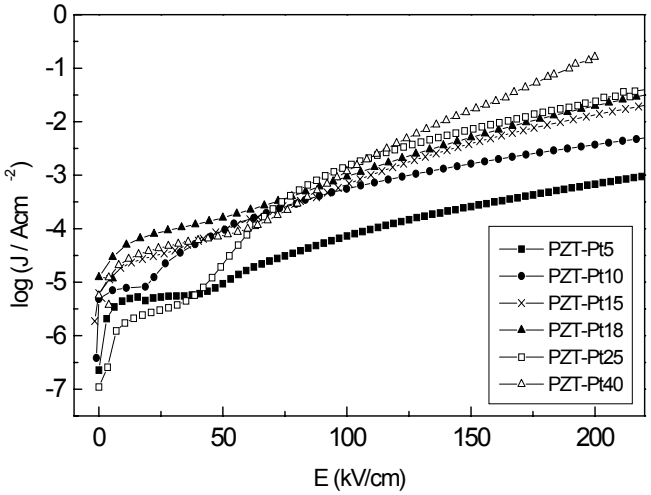

Fig. 6.5. *I-V* curves at positive bias of PZT-Pt films with different Pt contents.

The *I-V* curves of other PZT-Pt films are presented in Fig. 6.5. It can be seen that increasing the Pt content results in an increase of the leakage current: at first in an increase of the saturation current in regime II, secondly in a decrease of the onset field for regime III. The saturation regime disappears at 15 vol.% of Pt. The suppression of the leakage current

at intermediate electric fields for samples with Pt contents higher than 15 vol.% is considered to be due to trapping of injected carriers by deep traps, which can be emptied at higher temperatures [8].

6.4 Discussion

6.4.1 Theoretical outline

Since PZT has a band gap of 3.4 eV, we can treat it as a semiconductor and apply the energy band structure theory for a metal/semiconductor/metal system in which the two metals play the role of electrodes. Even though Nb-STO is an *n*-type doped semiconductor we will consider it as a metal because of its very high conductivity at high Nb-doping level.

6.4.1.1 Energy band structure in metal-semiconductor interface

a. Barrier height

In Fig. 6.6 the energy band structure of a metal/semiconductor interface in contact is sketched. E_F, E_v and E_c denote the Fermi level, the valence band and the conduction band, respectively. The energy difference or barrier for carrier injection from the metal to the semiconductor is termed a Schottky barrier (Φ_B). This barrier height is the difference between the work function of the metal [i] (Φ_M) and the electron affinity [ii] (χ) of the semiconductor:

$$\Phi_B = \Phi_M - \chi \qquad (6.1)$$

If the materials with different Fermi levels are brought together, charge will flow to equalise the Fermi levels through the whole structure, causing band bending near the interface. The layer of space charge with a width of w_d at the interface supports a potential drop $V_{bi} = \Phi_M - \Phi_s$, called the built-in or diffusion voltage (where Φ_s is the work function of the semiconductor).

[i] Work function: the energy difference between the vacuum level and the Fermi level edge.

[ii] Electron affinity: the energy difference between the vacuum level and the conduction band.

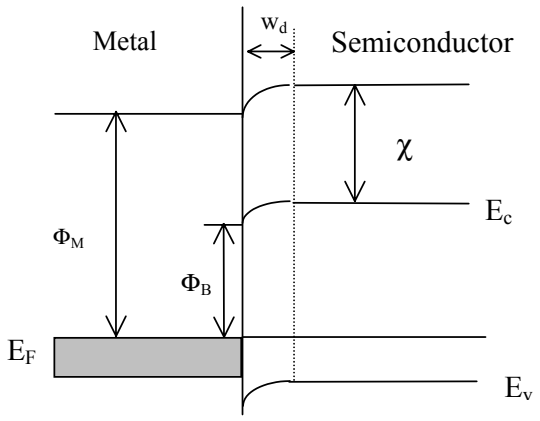

Fig. 6.6. Energy band diagram of a metal/semiconductor contact.

b. Depletion regions and flat-band voltage

The surface/interface states, which act as trapping centres for electrons and holes, can induce a space charge depletion region near the metal electrodes [9, 10]. In metal/semiconductor/metal systems, the depleted regions are present at both electrode interfaces. When a voltage is applied, the width of the depletion region near the reversed biased electrode increases. At a sufficiently large voltage, the depletion layer will expand over the whole thickness of the film, i.e. the film is fully depleted. The corresponding voltage is defined as the flat-band voltage V_{fb}, since under this condition there is no space charge at the interface, and the energy band is flat. V_{fb} can be described as follows [9]:

$$V_{fb} = \frac{qN_D d^2}{2\varepsilon_0 \varepsilon_s} \tag{6.2}$$

where ε_0, ε_s are the dielectric constants of vacuum and the semiconductor, respectively, q is the electron charge and N_D is the donor carrier concentration.

Only when the film is fully depleted, the electric field at the metal-insulator interface can be considered as the voltage over the film thickness: $E = V/d$.

6.4.1.2 Possible conduction mechanisms in thin films

In general, the leakage current through a metal/semiconductor/metal system is determined by the bulk properties of the film and by the electrode interface. Usually one of these factors is highly dominating. A distinction between a bulk-controlled and a interface-controlled conduction mechanism can be made by checking the symmetry of the leakage current with respect to the voltage polarity, while using different top and bottom elec-

trodes. The bulk-controlled mechanism will exhibit a symmetric *I-V* curve, while the interface-controlled mechanism will demonstrate an asymmetric curve.

a. Bulk-controlled conduction mechanisms

Bulk controlled conduction includes ohmic conduction, space charge limited current (SCLC) and Poole-Frenkel conduction. *Ohmic* conduction is often observed at low applied voltage and represents a linear dependence of current density on applied voltage. In the case of an ohmic contact, a space charge layer forms at the film/electrode interface above a critical onset voltage. This onset voltage strongly depends on the trap density in the film. The current is limited by the space charge layer, hence is called a *space charge limited current*. *Poole-Frenkel* conduction is due to the thermal excitation of electrons or holes from the trapping levels to the conduction band of the semiconductor [11].

b. Interface-controlled conduction mechanisms

These conduction mechanisms are due to the injection of carriers from the metal electrode into the film. The injection can be due to the following processes:

Fowler-Nordheim tunnelling: Electrons can tunnel through a barrier that is sufficiently thin (usually below 10 nm) and energetically high (see Fig. 6.7a). For thick films the tunnelling of electrons is possible when the interface barrier becomes thin under a very high field. Usually, the Fowler-Nordheim tunnelling exhibits a weak temperature dependence [12].

Thermionic emission: Electrons will cross the barrier from the metal electrode to the film if they have energy larger than the top of the barrier (see Fig. 6.7a). The actual shape of the barrier is hereby ignored. The current density is strongly dependent on temperature. A thermionic emission can be enhanced by the field-dependent barrier lowering, the so-called Schottky effect (Fig. 6.7b) [11, 12].

The asymmetric *I-V* curves obtained for Au/PZT/Nb-STO capacitors provided in Fig. 6.2 suggest that the conduction mechanisms would be interface-controlled. Since the tunnelling conduction usually occurs in the case of a very thin barrier (5-10 nm) and at an extremely high field, it is not favoured in thick films of 60 nm to 1.5 μm. Thermionic emission, enhanced by the Schottky effect hence is the most likely mechanism.

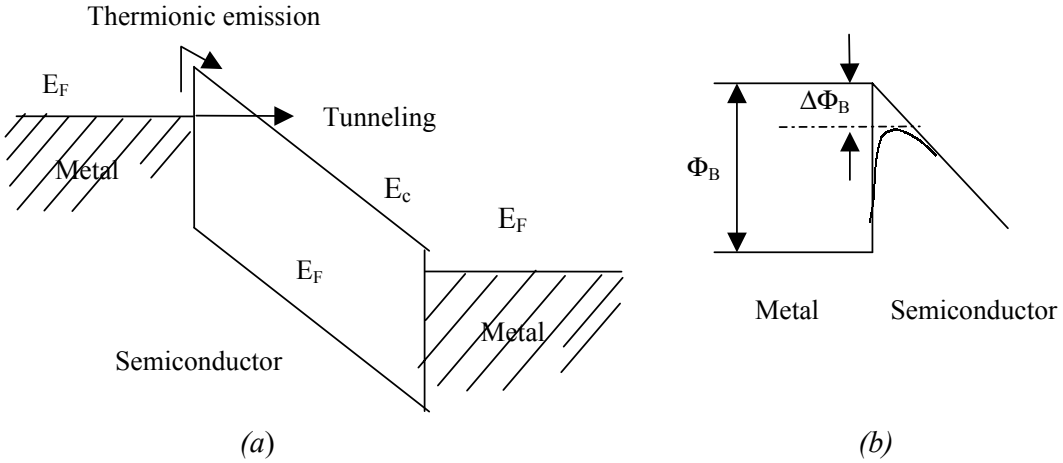

Fig. 6.7. (a) Injection of carriers from a metal into a semiconductor film [11], (b) The barrier lowering $\Delta\Phi_B$ for electrons due to the Schottky effect [12].

6.4.1.3 Thermionic emission model for metal/semiconductor/metal capacitors.

a. Thermionic emission

Thermionic emission of electrons over the Schottky barrier at film/electrode interface always occurs. However, at zero-voltage, the total flowing current via a metal/semiconductor/metal system is zero, since the backward and forward currents are equal, apart from the sign. Under an external electric field the barrier height at each metal/semiconductor interface changes and hence results in a non-zero current. We will present below how the current changes under an applied voltage and how it depends on the polarity of the applied voltage. For illustration an Au/PZT/Nb-STO structure is taken here as an example.

- *At V = 0*:

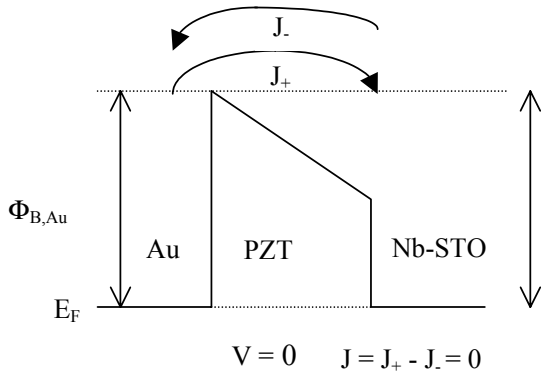

Fig. 6.8. Energy band diagram of Au/PZT/Nb-STO systems and resulting thermionic currents without bias voltage.

The energy band scheme of an Au/PZT/Nb-STO structure at zero voltage is sketched in Fig. 6.8 together with the resulting thermionic currents. Since the barrier height at the metal/semiconductor interface, but not the barrier shape determines the emission current, the forward and backward currents can be described as:

$$J_+ = J_- = A^{**}T^2 exp(-\frac{q\Phi_{B,Au}}{k_B T}) \tag{6.3}$$

where A^{**} denotes the effective Richardson constant, T the temperature, k_B Boltzmann's constant, $\Phi_{B,Au}$ the barrier height at PZT/Au interface. Because the backward and forward currents have the same magnitude, in this case no net current flows through the whole system.

- *At V < 0*:

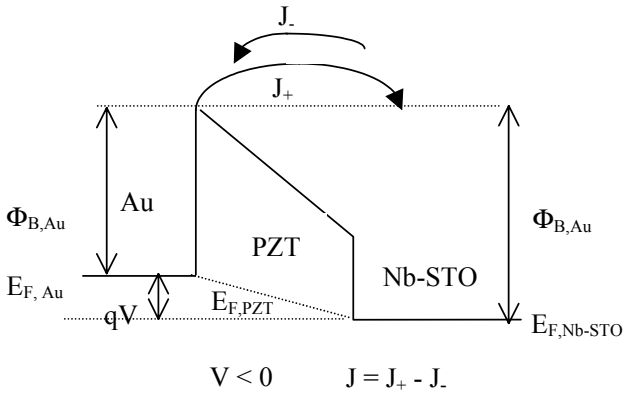

Fig. 6.9. Energy band diagram of Au/PZT/Nb-STO system at a negative bias voltage.

When a negative voltage is applied, the Fermi energy level of the metal is raised with respect to the Fermi energy in the semiconductor (see Fig. 6.9). As a consequence, the barrier height at the Au/PZT interface remains unchanged, while the barrier height at the Nb-STO/PZT interface is raised by an amount equal to qV. This results in an unchanged forward current:

$$J_+ = A^{**}T^2 exp(-\frac{q\Phi_{B,Au}}{k_B T}) \tag{6.4}$$

and a decreasing backward current:

$$J_- = A^{**}T^2 exp(-\frac{q\Phi_{B,Au} + qV}{k_B T}) \tag{6.5}$$

The total current density is given by the difference between J_+ and J_-:

$$J = J_+ - J_- = A^{**}T^2 exp(-\frac{q\Phi_{B,Au}}{k_B T})\left[1 - exp(-\frac{qV}{k_B T})\right] \quad (6.6)$$

Eq. (6.6) shows an increase of the net current with increasing voltage. However, at a sufficiently large voltage, where qV becomes larger than k_BT, the term exp(-qV/k_BT) vanishes and the current becomes voltage independent:

$$J = J_S = A^{**}T^2 exp(-\frac{q\Phi_{B,Au}}{k_B T}) \quad (6.7)$$

As a result, the *I-V* curve will represent a plateau, usually called the saturated regime. In this voltage regime, the current is limited only by the barrier height at the PZT/Au interface and the temperature.

- At V > 0:

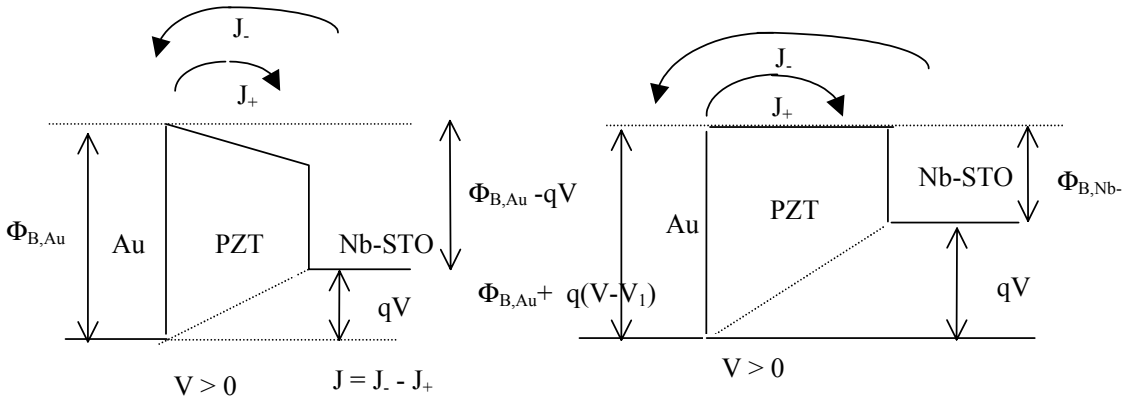

Fig. 6.10. Energy band diagram of Au/PZT/Nb-STO system at positive voltage $V < V_1$ (a), $V > V_1$ (b).

When a positive voltage is applied, the Fermi energy of the metal is lowered with respect to the Fermi energy in the semiconductor. The barrier height at the Au/PZT interface remains the same, while the barrier height at the Nb-STO/PZT interface decreases (Fig. 6.10a).

The total current flowing through the system is mainly caused by the backward current from the Nb-STO into the film. At voltages larger than V_1, where V_1 is defined by: $qV_1 = \Phi_{B,Au} - \Phi_{B,Nb\text{-}STO}$, the barrier height at the Nb-STO/PZT interface remains unchanged, while the barrier height at the Au/PZT interface starts to increase (see Fig. 6.10b). Now the backward current J_- remains the same and the forward current J_+ becomes smaller. The total current can than be described by the following equation:

$$J = A^{**}T^2 exp(-\frac{q\Phi_{B,Nb-STO}}{k_B T})\left[1 - exp(-\frac{qV}{k_B T})\right] \tag{6.8}$$

Eq. (6.8) has the same form as Eq. (6.6), it differs only in the barrier height value. This leads us to the conclusion that at negative bias the current is governed by the Au/PZT interface while at positive bias it is determined by the Nb-STO/PZT interface. In another words, it is the reverse biased interface that determines the net current through the system.

b. Schottky effect (Schottky emission)

From the previous section, it can be seen that above a certain voltage the current does not depend on the applied voltage but on the barrier height at the electrode/film interface. The current is kept constant if the barrier height value is voltage independent. However, due to the Schottky effect the barrier height is lowered under high electric field, resulting in an increase of the current density. The barrier height decrease, $\Delta\Phi_B$ (see Fig. 6.7b), equals to:

$$\Delta\Phi_B = (\frac{qE}{4\pi\varepsilon_0\varepsilon_r})^{1/2} \tag{6.9}$$

Here E is the electric field at the interface, ε_r is the optical dielectric constant (equal to the square of the refractive index), which is different from the d.c dielectric constant ε_s [i] appearing in Eq. (6.2). The lowering of the Schottky barrier leads to the following current expression:

$$J_s = A^{**}T^2 exp(-\frac{q\Phi_B}{k_B T})\exp\left[\frac{q}{k_B T}(\frac{qE}{4\pi\varepsilon_0\varepsilon_r})^{1/2}\right] \tag{6.10}$$

Rearranging Eq. (6.10) in different ways and taking the logarithm results in two different expressions:

$$\ln J_s = \frac{q}{k_B T}\left(\frac{q}{4\pi\varepsilon_0\varepsilon_r}\right)^{1/2} E^{1/2} + C_1 \tag{6.10a}$$

and: $$\ln\left(J_s / T^2\right) = \frac{q}{k_B}\left[\left(\frac{qE}{4\pi\varepsilon_0\varepsilon_r}\right)^{1/2} - \Phi_B\right]\frac{1}{T} + C_2 \tag{6.10b}$$

[i] The time spent by the electrons while moving through the barrier is short in comparison to the period of a long wavelength longitudinal optical photon. Hence Frohlich interaction between injected electrons and phonons is very limited. Thus here the optical dielectric constant, ε_∞, must be used.

where C_i are constants. Thus the plot of $\ln J_s$ vs. $E^{1/2}$ presents a straight line, where the value of ε_r can be obtained from its slope. Subsequently the value of Φ_B can be determined from the slope of the $\ln(J/T^2)$ vs. $1/T$ plot, once ε_r is known.

The Poole-Frenkel emission mentioned above has a virtually identical expression to that of the Schottky emission [11]. However, since the Poole-Frenkle emission is a bulk-controlled conduction, it can be easily distinguished from Schottky emission by evaluating the asymmetry of the leakage current using different bottom and top electrodes.

An important feature of the Schottky effect is that the lowering of the barrier is only experienced by a carrier while approaching the interface. It is therefore governed by the electric field at the interface between the film and the metallic electrode. Many publications assume the value of the electric field in Eq. (6.10) to be the average value of the applied voltage over the film thickness: $E = V/d$. This assumption is valid only for the flat-band condition: i.e. no space charge layer is formed at the interface, or the film is fully depleted. In Refs. [2, 8], the onset of the Schottky emission is considered to coincide with the flat-band voltage, which corresponds to the potential required to deplete the interfacial space charge at the film/electrode interface.

c. Thermionic emission accompanied with Schottky effect model

Based on the theoretical outline presented above, and on the experimental data obtained in Section 6.3, we propose the following conduction mechanism for PZT and PZT-Pt films. The conduction model actually combines thermionic emission and Schottky effects, taken into account the above-mentioned hypothesis on the Schottky onset.

- At low and intermediate electric fields, the conduction in the film follows the thermionic emission. The current density is dependent on the polarity of voltage and is governed by the reverse biased interface as described in Eqs. (6.6) and (6.8). A constant current versus applied voltage is expected until the applied voltage reaches the flat-band voltage value. Compared with the experimental data, the low-field and the constant current parts correspond to regimes I and II in Figs. 6.2 and 6.4, respectively.

- The Schottky effect is initialised at the flat-band voltage, giving rise to an increase in the current density, which represents regime III in Fig. 6.2. The current density now can be described by Eq. (6.10), where the barrier height, Φ_B, corresponds to the reverse biased interface.

6.4.2 Experimental verification of the model

6.4.2.1 I-V characteristics of PZT films

In this section, the proposed model will be used to analyse the *I-V* experimental data of PZT films in Figs. 6.2-6.3. The current in regime I is due to the difference between the thermionic currents from Nb-STO to PZT and from Au to PZT. Many authors ascribed the leakage current at low voltages to ohmic conduction. We, however, did not observe the linear dependence of current on voltage. In our case the ohmic current caused by the intrinsic charge carriers may be much smaller than the thermionic current.

The saturation regime (regime II) exhibits a voltage independent current, as predicted by Eq. (6.7). In this regime, the current is governed only by the barrier height at the electrode/film interface. In Ref. [13] similar *I-V* curves were observed and were explained by the thermionic emission model in combination with Fowler-Nordheim tunnelling. The transition from thermionic emission to the tunnelling mechanism is assigned to the cross-over from the saturation regime to the ascending regime at high field. Our data in the high field regime (regime III), however, match the Schottky equation provided in Eq. (6.10). The linear fit for $\ln J$ versus $E^{1/2}$, given in Fig. 6.11, provides a slope of 6.3×10^{-4}. From this slope a value of $\varepsilon_r = 5.7$ was derived for the optical dielectric constant (see Eq. (6.10a)), which is close to the optical dielectric constant of PZT presented in literature ($\varepsilon_r = 5.36$).

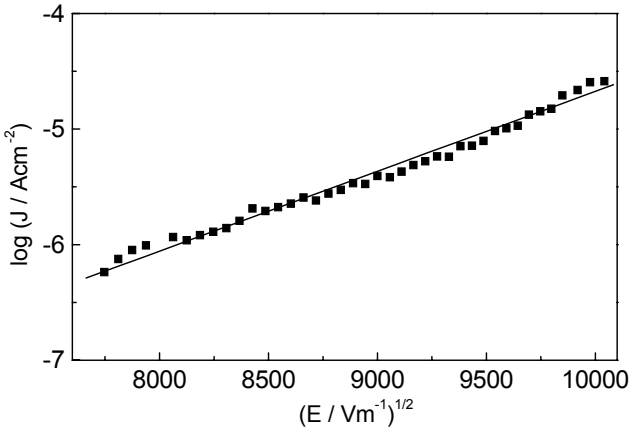

Fig. 6.11. The field dependence of the current in the high field regime (regime III) for data at positive bias, presented in Fig. 6.2. The solid line represents the linear fitting.

Since the Schottky emission is strongly temperature dependent, while the Fowler-Nordheim tunnelling is not, the temperature dependence of the *I-V* characteristics can be used to discriminate between these two conduction mechanisms. In Fig. 6.12 the leakage

currents at negative and positive bias are presented as function of the reciprocal temperature.

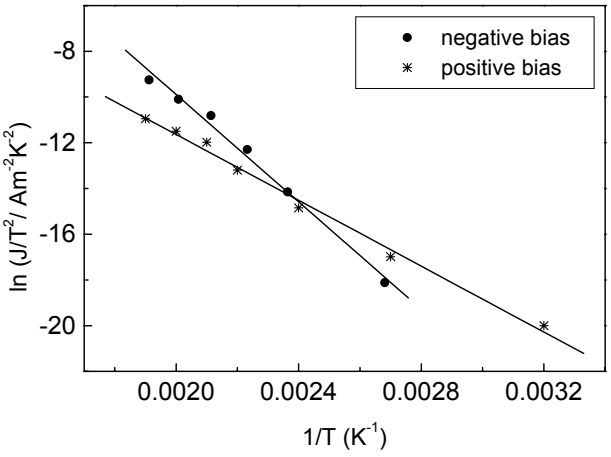

Fig. 6.12. Temperature dependence of the leakage current in a PZT film at positive (E = 500 kV/cm) and negative biases (E = -500 kV/cm). The dashed and solid lines represent linear fits for positive and negative biases, respectively.

The graphs of $\ln(J/T^2)$ vs. $1/T$ clearly fit to straight lines as expected from the Schottky equation (Eq. (6.11b)). The barrier height can be calculated from the slopes of these lines in combination with the fitting results from the graphs of $\ln J$ vs. $E^{1/2}$. The obtained values for negative bias is $\Phi_B = 1.22 \pm 0.07$ eV, while for positive bias $\Phi_B = 0.81 \pm 0.05$ eV is found.

The above-obtained values for barrier height are in agreement with theoretical calculations. Providing $\chi_{PZT} = 3.5$ eV [14] and $\Phi_{M,Au} = 4.6$ eV [14], $\Phi_{M,Nb\text{-}STO} = 4.2$ eV [15], one obtains the barrier height at the PZT/Au interface:

$$\Phi_B = \Phi_{M,\,Au} - \chi_{PZT} = 1.1 \text{ eV}$$

and the barrier height at the PZT/Nb-STO interface:

$$\Phi_B = \Phi_{M,\,Nb\text{-}STO} - \chi_{PZT} = 0.7 \text{ eV}$$

This supports the assumption that the conduction mechanism at positive bias is governed by the PZT/Nb-STO interface, and the conduction mechanism at negative bias is controlled by the PZT/Au interface. Since the barrier height at PZT/Nb-STO is lower than at PZT/Au, it explains why the current is larger at positive bias than at negative bias around room temperatures. At higher temperatures the situation reverses because under negative bias the current increases faster with increasing temperature than under positive bias.

As the current density depends on the Schottky barrier height, replacing the Au electrode with another metal having a higher work function, one can raise the barrier height and significantly reduce the leakage current density. In our observation, employing Pt as a top electrode instead of Au, leads to a much lower leakage current in the *I-V* curve at negative bias. The barrier height calculated for Pt/PZT interface is 1.35 eV, which is smaller than the theoretically expected: $\Phi_B = \Phi_{M,\,Pt} - \chi_{PZT} = 5.2 - 3.5 = 1.7$ eV, but it is quite close to the value of 1.5 eV experimentally observed in literature [14].

Below we will clarify the dependence of the leakage current on the film thickness. The studies on this subject presented so far in literature provide quite different results. In Ref. [16] the authors observe a significant increase of the leakage current with increasing film thickness, while other authors show that the leakage current does not depend on the film thickness [17].

From Fig. 6.3, it can be seen that for PZT films at low electric fields the current density does not depend on film thickness. All films exhibit the same saturation current, indicating a constant barrier height. Only at higher fields, the variation of current with film thickness becomes evident with the shifting of the Schottky emission onset towards smaller field values. The Schottky plots ln$J$ vs. $E^{1/2}$ for high-field data given in Fig. 6.13 provide almost identical values in the slopes, showing an insignificant change in the optical dielectric constant with changing film thickness.

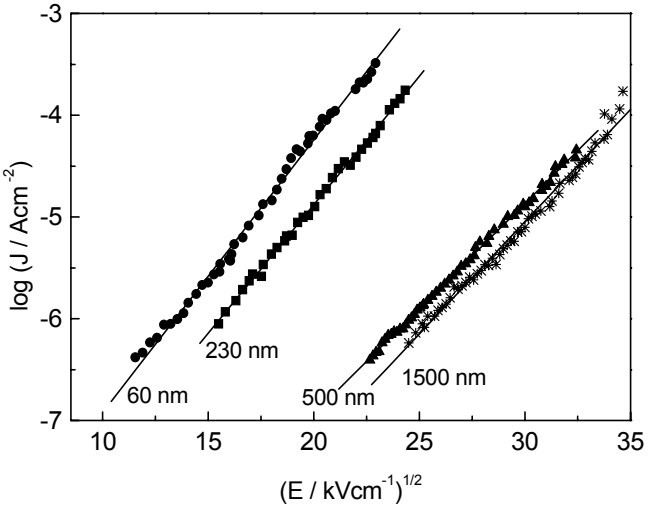

Fig. 6.13. Schottky plots for PZT films with different thicknesses. The solid lines represent linear fits.

If we assume that the onset voltage coincides with the flat-band voltage (see Eq. (6.2)) and the carrier concentration is in the same range for films with different thickness, thicker films would have Schottky emission starting earlier than thinner ones, as observed in Fig. 6.3. Using Eq. (6.2), the carrier concentrations were calculated from the flat-band voltage and listed in Table 6.1. The obtained values are in the same order of 10^{18} cm^{-3}, which is in agreement with our assumption made above. The slight increase of the carrier concentration with decreasing film thickness is possibly related to a higher defect density at the film surface.

Table 6.1. The carrier concentration calculated from flat-band voltage for PZT films with different thickness.

Film thickness d (nm)	1500	500	250	60
Carrier concentration N_D (cm^{-3})	0.9×10^{18}	3.3×10^{18}	2.7×10^{18}	11×10^{18}

In order to evaluate the consistency of the experimental data with the thermionic-Schottky model, we compared the experimental data given in Fig. 6.2 with the calculated values of the leakage current using Eqs. (6.8) and (6.10) with the following parameters: $\Phi_B = 0.81$ eV, $A^{**} = 125\times10^4$ $Am^{-2}K^{-2}$, $\varepsilon_r = 5.68$, $\varepsilon_s = 600$, $d = 500$ nm, $N_D = 3.3\times10^{18}$ cm^{-3}, $T = 300$ K. The calculated result, presented as the solid line in Fig. 6.14, fits very well with the experimental data in regimes II-III, but deviates in regime I (see Fig. 6.14). Other bulk-related factors, such as the trapping of charge carriers, drifting and diffusion of carriers in the bulk of the film, may contribute to the inconsistency of the model at low voltages.

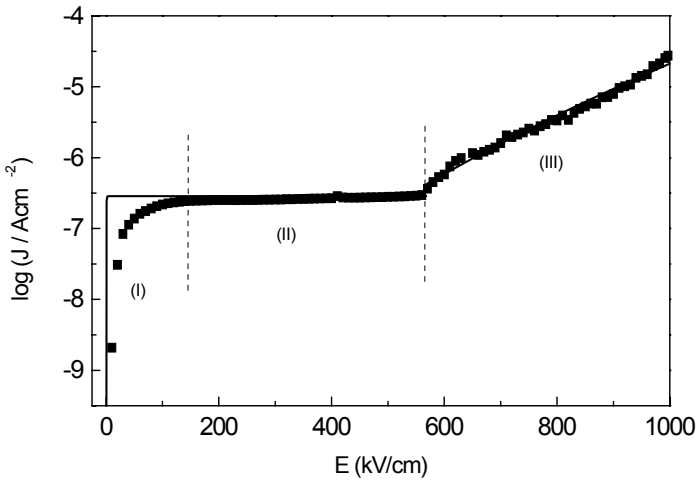

Fig. 6.14. *I-V* curve of the Au/PZT/Nb-STO system at positive bias, the solid line represents the fit of the curve using the thermionic-Schottky emission model.

6.4.2.2 I-V characteristics of PZT-Pt films

As described in Section 6.3.2, PZT-Pt films exhibit a higher leakage current than pure PZT films. The leakage current also increases with increasing Pt content. This increase of leakage is attributed to two factors: (a) the increase of the saturation current and (b) the shifting of the Schottky onset towards lower fields.

Based on Eq. (6.2), which describes the onset field of Schottky emission, the shrinking of the saturation regime with increasing Pt content may be related to the decrease in effective thickness of the PZT phase and to the increase of the effective dielectric constant with the dispersion of Pt. The voltage-dependence of the leakage current in the Schottky regime at positive bias is given in Fig. 6.15 for films with different Pt contents. All curves exhibit almost the same slopes for linear fits, indicating that the optical dielectric constant does not significantly vary with Pt content. For the PZT-Pt40 film, however, the experimental data deviates from the Schottky fit at high field. The sharper increase of the current at high fields implies the transition to another conduction mechanism. Taking into account that the high Pt content in the film results in very thin layers of PZT between the Pt particles, the conduction mechanism possibly relates to the tunnelling of electrons through a thin barrier under high electric field.

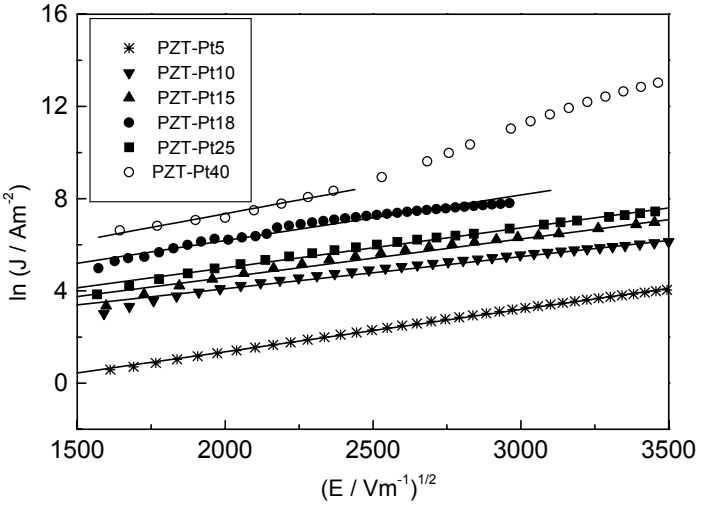

Fig. 6.15. *I-V* characteristics at positive bias, presented as ln*J* vs. $E^{1/2}$ plots, for films with different Pt contents. The solid lines represent linear fits.

The plots of $\ln(J/T^2)$ vs. $1/T$ for PZT and PZT-Pt films are presented in Fig. 6.16. From this figure it can be seen that the slope of the linear fit changes significantly going from pure PZT to a PZT-Pt5 film. With further increase in the Pt content the slopes continue to de-

crease, but only to a small extent. Using the Schottky equation (6.10b), the barrier heights at the film/electrode interface were calculated for films with different Pt contents. The obtained results are given in Table 6.2 and are illustrated in Fig. 6.17.

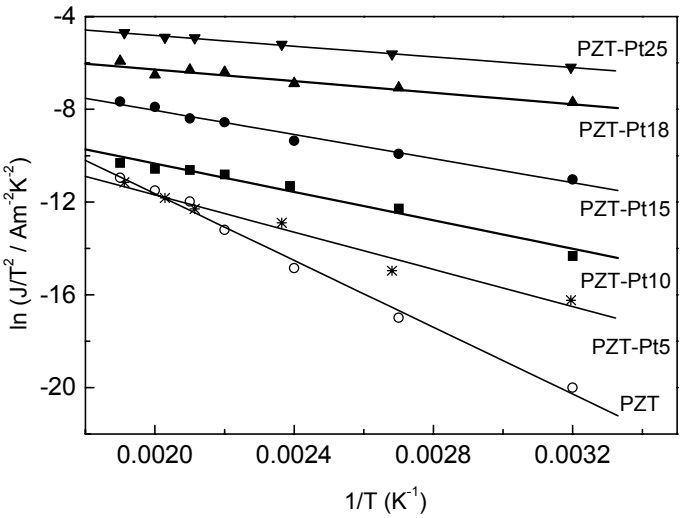

Fig. 6.16. Temperature dependence of the leakage current in PZT (E = 300 kV/cm) and PZT-Pt films with different Pt contents (E = 75 kV/cm). The solid lines indicate linear fits based on Eq. (6.10b).

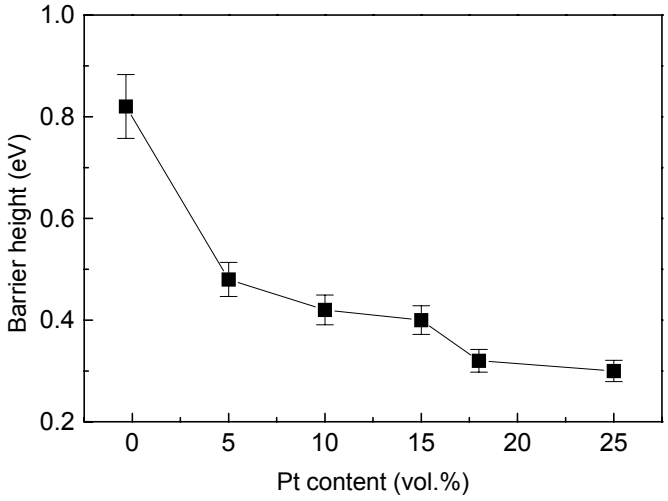

Fig. 6.17. Dependence of the barrier height in PZT-Pt films on Pt content.

Table 6.2. Barrier heights calculated at positive bias for PZT-Pt films with different Pt contents.

Pt content (vol. %)	0	5	10	15	18	25
Φ_B (eV)	0.81 ± 0.05	0.48 ± 0.04	0.41 ± 0.02	0.39 ± 0.03	0.32 ± 0.04	0.29 ± 0.03

As can be seen from these results, the barrier height strongly decreases at 5 vol.% Pt addition. At higher Pt contents the decrease tends to saturate. Since the current is exponential inversely proportional to the barrier height, a decrease of a few hundred meV in the barrier height results in an increase in the current of several orders of magnitude. It is well known from percolation theory or the effective media theories that the conductivity of an insulator-conductor mixture does not increase more than one order in the regime far from the percolation threshold. The drastic increase of the conductivity in thin films therefore underlines the role of the interface, or more specifically, the modification of the barrier height at the interface.

The lowering of the barrier height is usually related to barrier height inhomogeneties and the modification of interface states. In Ref. [18], the authors observed a considerably lower barrier height by the incorporation of 20 nm sized Au particles in Ti-Schottky contacts on silicon carbide (4H-SiC). The barrier height reduction is in the range of 0.19 to 0.25 eV as compared to particle-free Ti-Schottky contacts. It has been proposed that the lowering is caused by an enhanced electric field in the depletion region close to the surface of the semiconductor due to the small size of the Au nano-particles and the large difference between the barrier heights of Ti and Au [19]. By using Tung's dipole-layer approach [19], the potential distribution for a circular patch geometry at the interface was calculated. The electric field at the interface is only enhanced significantly when the size of embedded particles is smaller than 50 nm. With the dispersion of Pt in PZT-Pt films, contact of nano-Pt particles with the top and bottom electrodes is inevitable. Those small Pt inclusions can therefore enhance the electric field at the interface in the same way, leading to the lowering of the barrier height. Since this potential modification depends on the particles size and the barrier height only, we can expect a weak dependence of the barrier height lowering on the Pt content.

The barrier height of a metal-semiconductor contact is determined not only by the metal work function but also by the surface states [20, 21]. The formula given in Eq. (6.1) for

calculating the barrier height is actually for the ideal Schottky contact. The full expression derived by Cowley and Sze can be found in Ref. [8]:

$$\Phi_B = \left[S(\Phi_m - \chi) + (1-S)(E_g - \Phi_0) - \Delta\Phi_B \right] + \left\{ \frac{S^2 C}{2} - S^{3/2} \left[C(\Phi_m - \chi) + (1-S)(E_g - \Phi_0)\frac{C}{S} - \frac{C}{S}(E_g - E_F + k_B T) + \frac{C^2 S}{4} \right]^{1/2} \right\} \quad (6.11)$$

where S is the derivative of the barrier height with respect to electron affinity, E_g the band gap, Φ_0 the charge neutrality level [i], E_F the Fermi level. The quantity C is proportional to the donor concentration N_D and the dielectric constant ε_s. For semiconductors with a small dielectric constant ($\varepsilon_s \sim 10$) and a low carrier concentration ($N_D < 10^{18}$ cm^{-3}), C is in the order of 0.01 eV, the donor-concentration dependent term (the second term in Eq. (6.11)) can be discarded. However, for ferroelectric materials that have a high dielectric constant, a high carrier concentration can make that term significant, leading to the decrease of barrier height [21]. According to Ref. [21] if $\varepsilon_s \sim 400$, a value of $N_D = 10^{18}$ cm^{-3} and $N_D = 10^{20}$ cm^{-3} can increase C approximately up to 3.6 eV and 300 eV respectively, resulting in a reduction of the barrier height of about 0.1 eV when N_D increases by a factor 100, from 10^{18} cm^{-3} to 10^{20} cm^{-3}. Experimentally the barrier height of Au/n-GaAs Schottky diodes, determined from *C-V* measurements, has been found to decrease from 1.02 eV to 0.84 eV as the carrier concentration increases from 2.5×10^{15} to 1×10^{18} cm^{-3} [20]. This variation is ascribed to the change of the interface states near the semiconductor/metal interface. In PZT-Pt films, the increase in the carrier concentration can be caused by Pt addition, following the effective medium theories or percolation theory. The structural and morphological inhomogeneities at the interface in the presence of Pt also can increase the surface state densities. For example, the imperfect nature of the interface at the SiC-dielectric interface due to the presence of carbon clusters and/or dangling Si and C bonds is believed to cause a high density of trap or surface state energy [22].

In conclusion, a dispersion of Pt in PZT films leads to the increase of the leakage current. The decrease in the effective thickness of the PZT phase and the increase in the dielectric constant result in the earlier onset of the Schottky effect. Additionally, the decrease of the Schottky barrier height with a few hundred meV leads to an increase of the current with

[i] Charge neutrality level: the level below which all surface states must be filled for charge neutrality at the surface.

several orders of magnitude. The decrease of the Schottky barrier is tentatively attributed to either the incorporation of nano-Pt particles in the electrodes and/or the change in surface state density through the increase of charge carrier and the change in structural and morphological of film surface.

6.5 Conclusions

In this chapter we studied the conduction mechanism in metal/PZT-Pt/metal capacitors. The main conduction mechanism is thermionic emission of electrons over the Schottky barrier from the metal electrode to the ferroelectric film. The field-induced Schottky effect of barrier lowering due to the attractive "image" force between the electrons in the metal and those in the films is also considered. The onset for Schottky emission is assumed to coincide with the flat-band voltage. The calculated values using the above model exhibit inconsistency with the experimental data in the low-field regime, but demonstrate excellent matching for the intermediate and high-field regimes. Other *I-V* characteristics, e.g. the field dependence, the temperature dependence, the field polarity dependence and the film thickness dependence were clarified by the model. The influence of Pt addition on the increase of the leakage current was intuitively explained, considering the decrease of the PZT phase effective thickness, the increase of the dielectric constant and the decrease of the barrier height at the film/electrode interface. The latter is attributed to either the embedding of nano Pt-particles in the electrodes or the increase of surface state density.

References

1. J.F. Scott, C.A. Araujo, B.M. Melnick, L.D. McMillan and R. Zuleeg, *Quantitative measurement of space charge effects in lead zirconate titanate memories*, J. Appl. Phys. **70** (1991) 382.
2. C.H. Lin, P.A. Friddle, C.H. Ma, A. Daga and H. Chen, *Effect of thickness on the electrical properties of metalorganic chemical vapor deposited Pb(Zr,Ti)O_3 (25-100nm) thin films on $LaNiO_3$ buffered Si*, J. Appl. Phys. **90** (2001) 1509.
3. I. Boerasu, L. Pintilie, M. Pereira, M.I. Vasilevskiy and M.J.M. Gomes, *Competition between ferroelectric and semiconductor properties in $Pb(Zr_{0.65}Ti_{0.45})O_3$ thin films deposited by sol-gel*, J. Appl. Phys. **93** (2003) 4776.
4. Y.S. Sang, S.J. Lee, S.H. Kim, B.G. Cahe and M.S. Jang, *Schottky barrier effects in the electronic conduction of sol-gel derived lead zirconate titanate thin film capacitors*, J. Appl. Phys. **84** (1998), 5005.
5. K.H. Ahn, S.S. Kim and S. Baik, *Thickness dependence of leakage current behavior in epitaxial (Ba,Sr)TiO_3 film capacitors*, J. Appl. Phys. **93** (2003) 1725.
6. G. Dietz and R. Waser, *Charge injection in $SrTiO_3$ thin films*, Thin Solid Films **299** (1997) 53.
7. T. Mihara and H. Wanatabe, *Electronic conduction characteristics of sol-gel ferroelectric $Pb(Zr_{0.4}Ti_{0.6})O_3$ thin film capacitors: Part I*, Jpn. J. Appl. Phys. **34** (1995) 5664.
8. I. Stolichnov and A. Tagantsev, *Space-charge influenced-injection model for conduction in $Pb(Zr_xTi_{1-x})O_3$ thin films*, J. Appl. Phys. **84** (1998) 3216.
9. S.M. Sze, *Physics of semiconductor devices*, John Wiley & Sons, Inc., 1981, 2nd edition.
10. D.J. Roulston, *An introduction to the Physics of semiconductor devices, Oxford University Press, 1999*, New York, Oxford.
11. D.R. Lamb, *Electrical conduction mechanism in thin insulating films*, Methuen, London, 1967.
12. G.W. Dietz and W. Antpohler, *Electrode influence on the charge transport through $SrTiO_3$ thin films*, J. Appl. Phys. **78** (1995) 6113.
13. L. Zheng, C. Lin and T. Ma, *Current-voltage characteristic of asymmetric ferroelectric capacitors*, J. Phys. D: Appl. Phys. **29** (1996) 457.
14. J.F. Scott, *Ferroelectric memories*, Springer, Verlag Berlin Heidelberg 2000, pg. 99.
15. B. Nagaraj, T. Wu, S.B. Ogale, T. Venkatesan and R. Ramesh, *Interface characterisation of all-perovskite oxide field effect heterostructures*, J. Electroceram. **8** (2002) 233.
16. J. Shin, J. Park, C. Hwang and H.J. Kim, *Dielectric and electrical properties of sputter grown (Ba,Sr)TiO_3 film capacitors*, J. Appl. Phys. **86** (1999) 506.

17. G.W. Dietz, M. Schumacher and R. Waser, *Leakage current in $Ba_{0.7}Sr_{0.3}TiO_3$ thin films for ultrahigh-density dynamic random access memories*, J. Appl. Phys. **82** (1997) 2359

18. S.K. Lee, C.M. Zetterling, M. Ostling, I. Aberg, M.H. Magnusson, K. Deppert, L.E. Wernersson, L. Samuelson and A. Litwin, *Reduction of the Shottky barier height on silicon carbide using Au nano-particles*, Solid State Electronics **46** (2020) 1433.

19. R.T. Tung, *Electron transport at metal-semiconductor interfaces: general theory*, Phys. Rev. B **45** (1992) 13509.

20. M.K. Hudait and S.B. Krupanidhi, *Doping dependence of the barrier height and ideality factor of Au/n-GaAs Schottky diodes at low temperatures*, Physica B **307** (2001) 125.

21. M. Dawber, J.F. Scott and A.J. Hartmann, *Effect of donor and acceptor dopants on Schottky barrier heights and vacancy concentrations in barium strontium titanate*, J. Eur. Ceram. Soc. **21** (2001) 1633.

22. V.V. Afanasev, M. Bassler, G. Pensl and M. Schutlz, *Intrinsic SiC/SiO_2 interface states*, Physica Status Solidi **162** (1997) 321.

7

Recommendations

Below some recommendations for future research are given.

7.1 Suppressing the leakage current in PZT-Pt films

The high dielectric constant of PZT-Pt composites offers perspectives for super-capacitor and DRAM applications. The issue that remains to be solved is the high leakage current observed for thin films. The increase of the leakage current at high fields is due to Schottky emission of electrons/holes from the metallic electrode to the bulk of the film. Emission occurs through a barrier at the electrode/film interface. If it is possible to increase the barrier height, the leakage current will be minimized. S. Eglash *et al*. [1] proposed using a thin, highly doped layer at the metal-semiconductor interface to modify the effective barrier height. Thin *n*-layers at the interface were used to decrease the effective barrier height and thin *p*-layers were used to increase the barrier height. By this approach, the effective barrier height on *n*-type GaAs can be tuned in the wide range from near zero to 1.33 eV. In our case, a highly *p*-doped layer at the film/electrode interface hence can be useful to suppress the leakage current of PZT-Pt thin films.

7.2 Nano-polar domains and off-set charge

Even though PZT-Pt films with Pt contents above 10 vol.% are not of interest for practical applications due to the high loss, high leakage and low polarization, their relaxor-like and graded-like behaviours might be of interest for theoretical aspects.

The slimming of the *P-E* loops and the shift towards lower values of the temperature at which the dielectric constant is maximum (T_M) resemble the behaviour of a relaxor. We suggest that the formation of nano-polar PZT domains, resulted from the breaking of long-range order of polarization in the presence of Pt phase, is responsible for this observation. However, the temperature dependence of the dielectric constant as a function of frequency should be investigated more carefully in order to elucidate the relaxor-nature of

PZT-Pt films. TEM observation of domains in the films is highly recommended to see if nano-polar domains do form in the presence of Pt.

The shifting of *P-E* loops upon a.c field is similar to what is observed for graded-ferroelectrics. According to Mantese *et al*. [2] the graded- ferroelectrics posses very high pseudo pyroelectric effect, which is defined as $p_{\text{pseudo}} = \partial(\Delta Q / A) / \partial T |_E$, where A is the electrode surface area and ΔQ the charge offset upon field excitation. The following relationship is expected: $p_{\text{pseudo}} \sim E^{2\gamma}$, which can be quite large with γ = 3-5. It should be noted that the observed offsets in our films are very large, greater than 160 μC/cm^2 at 160 kV/cm (see Fig. 5.8) as compared with the value of 60 μC/cm^2 when driven at 700 kV/cm for graded BST [2] or 400 μC/cm^2 at 500 kV/cm for graded PZT [3]. New devices can be developed based on this new hysteresis quantity: the offset charge. Further studies on the pyroelectric properties as well as on the origin of the charge offset would be of interest for PZT-Pt composite thin films.

7.3 Design a hetero-structure with functional properties

The study of chemically and structurally non-uniform ferroelectric materials has recently received great attention for the understanding of the related electrical properties. The formation of polarization variable heterostructures, however, has been primarily an artifact of their growth process rather than through design. Based on the knowledge of the influence of the volume fraction and spatial distribution of the Pt phase on the dielectric and ferroelectric properties of PZT-Pt, a hetero-structure can be designed from layers of PZT; Pt and PZT-Pt composites for a specific requirement. Those properties can be tuned through changing the thickness as well as the composition of each layer. Graded-ferroelectrics can be fabricated by varying the Pt content in each PZT-Pt layers.

7.4 Hydrogen sensor application

Hydrogen sensors are developed based on catalytic metal (Pd, Pt, Ag) gate-insulator-semiconductor (metal) structures, where the quantity measured is the change in threshold voltage upon changing H_2 concentration [4-8]. H_2 molecules dissociate at the top surface of the catalytic metal layer and then accumulate at the interface between the metal and the insulator film. Dipoles are thus formed so that a polarization potential is built up at the interface, causing the change in threshold voltage [4]. The state-of-the-art is listed in Table. 7.1

Table 7.1 Hydrogen sensitivity of different hydrogen sensor devices.

Device	Voltage shift (eV)	H_2 concentration (ppm)	Dielectric constant of insulator
Pd/SiO_2/Si [4]	0.62	1000	3.9
Pt/SiO_2/SiC/Si [6]	0.61	6000	3.9
Pd/amorphous PZT/Pt [7]	2.3	1000	22
Pd/ amorphous BST/Pt [8]	4.5	1000	20

The hydrogen sensitivity of the device is attributed to the adsorption of hydrogen dipoles at the metal/insulator interface [4] and to the dielectric constant of the insulator, which enhances the dipole polarization [8]. As can be seen from Table 7.1, the highest sensitivity obtained so far is for devices using ferroelectric layers. This can be explained by the much higher dielectric constant of ferroelectrics compared to that of SiO_2. If, instead of PZT or BST, Pt/PZT or Pt/BST composite layers are used, we can increase the dielectric constant of the insulator and the effective surface area of the catalytic metal gate and hence, might be able to enhance the sensitivity of the device. However, it is noted here that for this application, amorphous films are recommended for a better blocking effect of protons.

References

1. S.J. Eglash, N. Newman, S. Pan, D. Mo, K. Shenai, W.E. Spicer, F.A. Ponce and D.M. Collins, *Engineered Schottky barrier diodes for the modification and control of Schottky barrier heights*, J. Appl. Phys. **61** (1987) 5159.

2. J.V. Mantese, N.W. Schubring, A.L. Micheli, A.B. Catalan, M.S. Mohammed, R. Naik and G.W. Auner, *Slater model applied to polarisation graded ferroelectrics*, Appl. Phys. Lett. **71** (1997) 2047.

3. M. Bazier, M. McElfresh and S. Mansour, *Unconventional hysteresis behavior in compositionally graded Pb(Zr,Ti)O_3 thin films*, Appl. Phys. Lett. **72** (1998) 1121.

4. Y. Gurbuz, W.P. Kang, J.L. Davidson, D.L. Kinser, D.V. Kerns, *Diamond microelectronic gas sensors*, Sensors and Actuators B **33** (1996) 100.

5. Y. Morita, K. Nakamura, C. Kim, *Langmuir analysis on hydrogen gas response of palladium-gate FET*, Sensors and Actuators B **33** (1996) 96.

6. A. Arbab, A. Spetz and I. Lundstrom, *Gas sensors for high temperature operation based on metal oxide silicon carbide (MOSiC) devices*, Sensors and Actuators B **15** (1993), 19.

7. J. Deng, W. Zhu, O.K. Tan, X. Yao, *Amorphous Pb(Zr,Ti)O_3 thin film hydrogen gas sensor*, Sensors and Actuators B **77** (2001) 416.

8. W. Zhu, O.K. Tan and X. Yao, *Amorphous ferroelectric ($Ba_{0.67}Sr_{0.33}$)$Ti_{1.02}O_3$ thin films with enhanced H_2 induced interfacial polarisation potential*, J. Appl. Phys. **84** (1998) 5134.

Summary

Ferroelectric materials are important for many industrial applications, ranging from high-dielectric constant capacitors to later developments in piezoelectric transducers, sensors, actuators and memories. To meet stringent requirements for a specific application their physical properties can be tailored, e.g., by varying the synthesis conditions, doping with a foreign element or adding a second phase. In this thesis the preparation and characterisation of dual-phase PZT-Pt composites, in the form of bulk and thin films, have been presented. The basic idea is to enhance the dielectric and ferroelectric properties of PZT by dispersion of Pt in the PZT matrix. The dispersion reduces the effective thickness phase of PZT, hence results in an increase of the effective dielectric constant and a decrease of coercivity. The formation of space charges at PZT/Pt interfaces also contributes to the enhancement of the dielectric constant and the total polarisation of material. The high dielectric constant of such composites is promising for application in super-capacitors or for DRAM devices, while the low coercivity suits low-voltage operation for applications like non-volatile memories.

Dual-phase PZT-Pt composites were prepared successfully by the sol-precipitation route, in which PZT powder is wet mixed with a sol containing Pt nano-particles. The use of a suitable stabilization agent prevents agglomeration of the Pt particles in the sol while the wet mixing ensures a homogenous phase distribution. The dielectric constant at room temperature of the PZT-Pt composites reaches a 6-times enhancement at 28 vol.% of Pt relative to that observed for bulk ceramic PZT. The increase of the dielectric constant with increase of the Pt content in the composites can be fitted with the Bruggeman symmetric equations and the normalized percolation equation. The composites exhibit higher polarisations than pure PZT, which is attributed to the space charge polarisation formed at PZT/Pt interfaces.

Thin films of PZT-Pt were fabricated by Pulsed Laser Deposition. The film microstructure can be controlled through changing the deposition conditions. Among various deposition parameters, the laser energy density plays the most important role since it determines the stability of plasma formed during deposition and hence strongly influences the properties of the film. The highest enhancement factor of the dielectric constant obtained for thin films equals to 8 at 10 vol.% Pt. Films with Pt contents below 10 vol.% exhibit good prop-

erties: high dielectric constant, low dielectric loss, high polarisation and low coercive field. For films with Pt contents higher than 10 vol.% both the dielectric and ferroelectric properties degraded. The change from micro to nano-size in domain structure of PZT in the presence of Pt particles is considered to be responsible for the degradation of ferrolectric properties. The dielectric and ferroelectric properties are dependent on the film morphology, such as the spatial distribution of Pt phase and also the film roughness.

Because charged defects may also induce enhanced degradation for fatigue, imprint and retention, it is imperative to determine the concentrations and mobilities of these species. Studies on the electronic and ionic conductivities of PZT using complex impedance spectroscopy suggest that lead and oxygen vacancies are the majority lattice defects. The *p*-type conductivity is found dominant at high temperature above the Curie transition, while below it a significant contribution of ionic conductivity is observed. The slow equilibration of the oxygen exchange reaction between the gas phase and the oxide at low temperature contributes to a higher value of the activation energy of both ionic and electronic conductivities than that observed at high-temperature. Defect association between lead vacancies and oxygen vacancies in the tetragonal phase reduces the ionic conductivity.

From bulk to thin film of PZT-Pt the conduction mechanism changes from bulk-controlled to interface-controlled. The *I-V* characteristics of PZT and PZT-Pt films can be well explained by the thermionic-Schottky emission model. The current at low and intermediate fields is due to the thermionic emission of electrons/holes over the Schottky barrier height from the reverse biased electrode into the film. At high fields, the lowering of the barrier heights due to the Schottky effect results in a stronger increase of current. The increase of leakage current in PZT-Pt films with increasing Pt content is attributed to the earlier onset of the Schottky effect and to the decrease of the barrier height at the film/electrode interface in the presence of Pt phase. The former is due to the decrease of the effective thickness of PZT phase and the increase of the effective dielectric constant. The latter is attributed to either the embedding of nano Pt-particles in the electrodes or the increase of surface state density.

Samenvatting

Ferro-elektrische materialen zijn van groot belang voor veel industriële toepassingen: van condensatoren met een hoge diëlektrische constante tot recente ontwikkelingen zoals piëzo-elektrische transducers, sensoren, actuatoren en geheugens. Om tegemoet te komen aan de stringente eisen voor specifieke toepassingen, kunnen de fysische eigenschappen aangepast worden, bijvoorbeeld via controle van de synthese condities, het dopen met vreemde elementen of door het toevoegen van een tweede fase. In dit proefschrift wordt de preparatie en karakterisering van duo-fase PZT-Pt composieten, in bulk vorm en als dunne film, gepresenteerd. Het uitgangspunt is de diëlektrische en ferro-elektrische eigenschappen van PZT te versterken door dispersie van Pt in de PZT matrix. De dispersie verkleint de effectieve dikte van de PZT fase waardoor de effectieve diëlektrische constante toeneemt en de coërciviteit afneemt. Het ontstaan van ruimteladingen aan de PZT/Pt grenslagen draagt eveneens bij aan de toename van de diëlektrische constante en de totale polarisatie van het materiaal. De hoge diëlektrische constante van deze composieten is veelbelovend voor toepassing in supercondensatoren en DRAM schakelingen, terwijl de lage coërciviteit bijvoorbeeld het toepassen van permanente geheugens bij lage bedrijfsspanningen mogelijk maakt.

Met succes zijn twee-fasen composieten van PZT-Pt gemaakt via de sol-precipitatie route, waarbij het PZT nat gemengd is met een sol van Pt-deeltjes in de nanometer range. Door gebruik te maken van een geëigende stabilisator wordt voorkomen dat de Pt-deeltjes in de sol aglomereren, terwijl het nat mengen een homogene faseverdeling bewerkstelligd. De diëlektrische constante van de PZT-Pt composieten bereikt voor 28 vol.% Pt bij kamertemperatuur een zesvoudige relatieve toename ten opzichte van PZT keramiek. De toename van de diëlektrische constante met het Pt gehalte in de composieten kan gemodelleerd worden met de symmetrische vergelijkingen van Bruggeman en de genormaliseerde percolatie vergelijking. De composieten vertonen een grotere polarisatie dan gemeten voor zuiver PZT, wat wordt toegeschreven aan de ruimteladingspolarisatie die gevormd wordt aan de PZT/Pt grensvlakken.

Dunne PZT-Pt films zijn vervaardigd door middel van gepulste laser depositie (Pulsed Laser Deposition, PLD). De microstructuur van de film kan gestuurd worden door het aanpassen van depositiecondities. Onder de verschillende procesparameters is de energie-

dichtheid van de laserbundel de meest belangrijke omdat deze tijdens de depositie de stabiliteit bepaalt van het gevormde plasma. Daardoor heeft deze energiedichtheid ook een sterke invloed op de eigenschappen van de PZT-film. De grootste toename in de diëlektrische constante wordt gevonden voor dunne films met 8 tot 10 vol.% Pt. Films met een Pt-fractie onder de 10 vol.% vertonen goede eigenschappen: een hoge diëlektrische constante, lage diëlektrische veliezen, grote polarisatie en een laag coërcief veld. Bij films met meer dan 10 vol.% Pt waren zowel de diëlektrische als de ferro-elektrische eigenschappen onderhevig aan degradatie. De overgang van micro- naar nano-grootte in de domeinstructuur van PZT in de aanwezigheid van Pt, wordt verondersteld verantwoordelijk te zijn voor de degradatie van de ferro-elektrische eigenschappen. De diëlektrische en ferro-elektrische eigenschappen zijn afhankelijk van de morfologie van de film, bijvoorbeeld de ruimtelijke verdeling van de Pt-fase, maar ook van de ruwheid van de film.

Omdat geladen defecten eveneens verhoogde degradatie, ten gevolge van vermoeiing, "imprint" en "retention", kunnen veroorzaken is het van groot belang om de concentratie en mobiliteit van deze defecten te bepalen. Bestudering van de elektronische en ionogene geleidbaarheid van PZT, met gebruikmaking van complexe impedantie spectroscopie, leidt tot de suggestie dat lood- en zuurstofvacatures de overheersende roosterfouten zijn.

p-Type geleiding is overheersend bij temperaturen boven de Curie overgang, terwijl beneden de Curie-temperatuur een significante bijdrage van de ionengeleiding wordt waargenomen. De trage instelling van het evenwicht in de zuurstof-uitwisselingsreactie tussen de gasfase en het oxide bij deze lage temperaturen leidt tot een hogere activeringsenergie voor zowel de ionogene als de elektronische geleiding dan wat voor de hoge temperatuur fase wordt gevonden. Defect-associatie in de tetragonale fase tussen loodvacatures en zuurstofvacatures verlaagt de ionengeleiding.

Gaande van bulk naar dunne film verandert het geleidingsmechanisme van PZT-Pt van bulk gecontroleerd naar grensvlak gecontroleerd. De *I-V* karakteristieken van PZT en PZT-Pt films kunnen goed worden verklaard met het thermionische Schottky emissie model. De stroom bij lage en gemiddelde velden wordt veroorzaakt door de thermionische emissie van elektronen/elektronen-gaten over de Schottky barrière van de negatief gepolariseerde elektrode de film in. Bij hoge veldsterkten wordt de barrière verlaagd ten gevolge van het Schottky effect, wat resulteert in een sterke toename van de stroom. De toename in de lekstroom bij toename van het Pt-gehalte in PZT-Pt films wordt toegeschreven aan een vervroegd optreden van de "Schottky onset", en aan de afname in the barrièrehoogte aan het

film/elektrode grensvlak door de aanwezigheid van de Pt-fase. Het eerste effect is het gevolge van de afname van de effectieve dikte van de PZT fase en de toename in de diëlektrische constante. Het tweede effect wordt toegeschreven aan ofwel de inbedding van Pt nano-deeltjes in de elektroden, ofwel aan een toename in de toestandsdichtheid aan het oppervlak.

Appendix. Influence of film thickness on P-E loops of PZT films

The *P-E* loops measured at 100 Hz for PZT films with different thickness (*d*) are provided below. It is evident that with decreasing thickness, the remanent polarization (P_r) decreases and the coercive field (E_c) increases. The 60 nm thick film does not exhibit the switching behaviour.

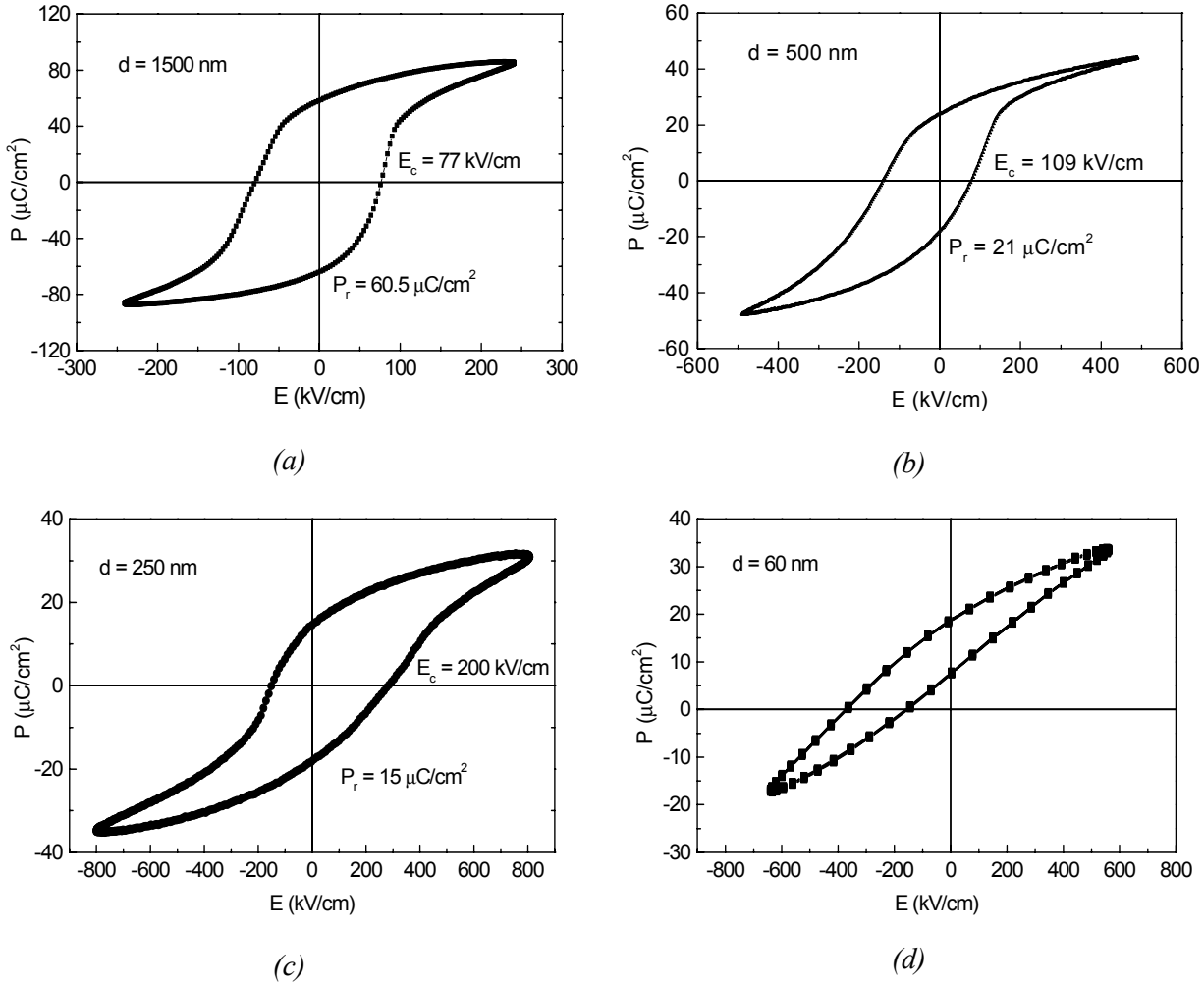

Figure 1. *P-E* loops of PZT films with different thickness: 1500 nm (a), 500 nm (b), 250 nm (c) and 60 nm (d).

Acknowledgements

I would like to save these pages to express my thanks to all people, who, by any means, provide help and support during my last four years of Ph.D.

First of all, I would like to express my gratitude to Prof. Dave Blank, my promotor, for his general guidance, encouragement and continuous support. Dave, thanks also for all the discussions we had at the PLD meetings and a warm atmosphere at the Ph.D. dinners.

I am thankful to my supervisors, at the very beginning, Dr. Henny Bouwmeester, and later, Dr. Guus Rijnders for their close guidance, stimulating discussions and especially the detailed reading and correction of my thesis.

I would like to thank all the committee members for the careful reading and the instructive comments to my thesis. Special thanks are to Dr. Bernard Boukamp for his contribution to the realisation of Chapter 2 and the Dutch translation of the summary.

I am indebted to many people whose their collaboration leads to success of my work: Dr. Pim Groen from Yageo B.V. for *P-E* measurement of bulk samples, Dr. Alwin Marsman from Philips Research Laboratory Eindhoven for *P-E* measurement of thin films, Marcel Weusthof and Henk Vries for *C-V* and *I-V* measurements, Mark Smitthers for SEM measurement, Rico Keim for TEM measurements, Albert van de Berg for XPS analysis, Herman Koster for XRD and SEM measurements, Louise Vrielink for XRF measurement and Joop Snoeyenbos for polishing the samples. My working time in MESA$^+$ would have been very difficult without the help from Frank Roesthuis, my "problem solver" and Dick Veldhuis, my "ex-neighbour". Help from other guys, Frank, Matthijn, Mark, Koray, Arjen M., Arjen J., Joska, Paul, Ard is also thankful.

It was a pleasure to be at a very nice group as AMK. I would like to thank all the members of the group for a pleasant working atmosphere and especially for nice conversations at the coffee breaks. Very special thanks are to my office mates: *three girls* Jelena, Monse, Krisztina and *a boy* Frédéric for sharing with me the good and the bad times. My dear friends, Ashima, José and André, Riaan, Samuel, Sankho, Richard, Vittorio, Tijana, Wika, Mieke, Cindy, Peter (DSM), without your friendship my stay in Enschede would not be that enjoyable. Louis and Henk, thanks for your wise advice concerning experimental work. Attila, thanks for your help whenever I need in the lab and sorry for not being able

to “fluiten”. I will not forget Cis’s kindness when I first came to the group and the amazingly quick help in any little things from Marion in the last two years.

Being a foreigner studying in the Netherlands, I very much appreciate the warm relationship and caring among our Vietnamese community. Thanks to my Vietnamese friends in Enschede: Hien and Nhu and Quynh Anh, Kim and Van Anh, Hieu and Lam, Hanh and Hoang Anh, Tu and An, Phuong and Ha and Viet Hung, Duy and Chi, Long, Kien, Giang, Chi, Nhung, Hoa, Cuong and in Amsterdam: Mai, Thanh, Hue; and to my close friends in Vietnam for their remote but precious support: Nga, V. Phuong, Ngan, Thao, Tung, Trinh, Son, Q. Phuong, Diep, Huong, “Bac”, Giang.

I am grateful to all Vietnamese former teachers, staff members at the Chemical Analysis group (Department of Chemistry, Vietnam National University) and at the International Training Institute for Materials Science (ITIMS) in Hanoi that I could not mention their names one-by-one. Sincere thanks are due to Prof. Tran Chuong Huyen and Prof. Pham Luan from the Chemical Analysis group for their kind support when I was in Hanoi as well as in Enschede.

And of course how can I forget to mention my beloved family: my parents, Hoan and Lien, my parents in law, Gioi and Muu, my brothers and sister Thanh, Loi, Huyen and my little niece Bao Han with their unlimited love and trust in me.

My last but deepest thanks are for my dearest husbie Thang, for everything he does for me and *our little family*.

Enschede, December 2004